Montanuniversitaet Leoben

Doctoral Thesis

Plasticity and fatigue of miniaturized Cu structures

Alexander Wimmer

Leoben, June 2014

June 26th, 2014

Erich Schmid Institute of Materials Science

Austrian Academy of Sciences

Department Materials Physics

Montanuniversitaet Leoben

Jahnstraße 12

A-8700 Leoben

Affidavit

I declare in lieu of oath, that I wrote this thesis and performed the associated research myself, using only literature cited in this volume.

Leoben, June 2014

//

Acknowledgements

First of all I want to thank my doctoral advisor Prof. Gerhard Dehm, who was a tremendous mentor for me. Without his supervision and constant help this dissertation would not have been possible. Furthermore I am grateful for the second opinion of Prof. Helmut Clemens.

I would also like to thank Prof. Xavier Sauvage and Prof. Frederic Danoix, supporting me with atom probe tomography at CNRS Rouen. Furthermore my gratitude is expressed to Dr. Pyuck-Pa Choi, Dr. Franz Roters, Dr. Michael Herbig, Dr. Pratheek Shanthraj, Wei Guo, M.Sc., Monika Nellessen and Uwe Tezins, helping me during the measurements at the Max-Planck-Institut Düsseldorf. I want to thank all my colleagues at the Erich Schmid Institute for fruitful discussions and their help. Special thank is expressed to Dr. Christoph Kirchlechner, Dr. Megan Cordill, assoc. Prof. Daniel Kiener and Prof. Reinhard Pippan answering my questions on micro-plasticity and fatigue. Furthermore I thank Dr. Martin Smolka and Alexander Leitner for supporting me with the experimental part of this work. In addition I thank DI Mario Stefenelli and Dr. Jürgen Maierhofer for beneficial discussions.

I am grateful for the support of Mag. Elisabeth Regittnig, DI Josef Fugger, Dr. Walther Heinz, DI Michael Fugger, Dr. Werner Robl and Dr. Thomas Detzel from KAI and Infineon for the support during the past years. I also want to thank the Montanuniversitaet Leoben, the Government of Lower Austria and Dr. Cornelius Grupp for their financial support granted through scholarships.

I would like to express the deepest appreciation to my family and friends, without their help I wouldn't be the person I am today and I wouldn't be where I am now.

Abstract

Moore’s law, indicating that the complexity of integrated circuits is doubled every 12 months, is only possible due to miniaturization and optimization of microelectronic devices, consisting of semiconductors, isolators and metallic thin films. These thin films play an important role in devices such as microelectromechanical systems (MEMS). Metallic Cu films, for example, transport the electric current between the semiconductor structures and if they are thick enough can also act as heat sinks for the thermal energy generated by Joule heating. During the lifetime of miniaturized Cu structures these are exposed to several billion thermal cycles, which can cause cracks and subsequently premature failure if the strength of the metal structure is not sufficient. Consequently in this thesis the mechanical properties of Cu thin film structures with different grain sizes are studied to gain insight into the deformation mechanisms, allowing lifetime predictions and optimization of the material behavior. Testing of the Cu films was done by shaping tensile samples and bending beams by a lithographic process and applying miniaturized mechanical experiments mainly conducted inside a scanning electron microscope (SEM).

For analysis of the static mechanical properties, such as yield strength, ultimate tensile strength and elongation to fracture, tensile tests between 143 and 873 K were performed. These experiments gave insight into the activation energies as well as the activation volumes, and subsequently to the underlying deformation mechanisms. The experiments above room temperature revealed an embrittlement in the material with 2.7 µm grain size. Chemical analysis and calculations concerning segregation, work of separation and diffusion indicate a segregation of non-metallic impurities to the grain boundaries.

As the cyclic properties are of great interest for practical applications, cyclic creep experiments (ratcheting) between 293 and 673 K were performed, pointing out the same deformation mechanisms as found in the static experiments. The lifetime, which strongly depends on the creep strain per cycle, was described by a modified Basquin equation. However, as the ratio between the maximum and minimum stress is negative in real life Cu microstructures, also bending experiments were conducted to mimic the alternating stress conditions. In contrast to the ratcheting experiments,

these show the extensive formation of intrusions and extrusions on the surface and cell structures inside the freestanding Cu beams.

In situ like electron backscatter diffraction (EBSD) studies during the static and cyclic experiments provided insight into the evolution of the geometrically necessary dislocation (GND) density and the microstructure evolution of the surface grains, which dominate the strength of small scale samples. The deformation behavior recorded at the surface of the samples in the *in situ* SEM experiments, measurements of the GND density, deduced activation volumes and energies point all towards dislocation plasticity as the dominating deformation mechanism. However, with decreasing grain size grain diffusion comes increasingly into play at temperatures exceeding room temperature.

The results of this thesis are enclosed as four publications. Publication A reports on the grain boundary embrittlement observed in static experiments between 293 and 673 K. Publication B demonstrates the deformation behavior in static and cyclic tension-tension experiments at room temperature, while Publication C extends this study into before unreached temperature regimes for micron-sized samples with experiments being performed between 143 and 873 K. Finally, Publication D presents cyclic bending experiments with *in situ* like EBSD at room temperature.

The present thesis demonstrates that the microstructural design must be performed carefully as the effects of the microstructure are changing with the temperature. Static and cyclic experiments accompanied by *in situ* SEM/EBSD with different stress-ratios gave insight into deformation mechanisms and pointed out a change from bulk-like to small scale behavior in the analyzed grain size regime.

Kurzfassung

Das Mooresche Gesetz, welches eine Verdopplung der Komplexität von elektrischen Schaltkreisen alle 12 Monate vorhersagt, ist nur möglich durch die kontinuierliche Verkleinerung und Optimierung von mikroelektronischen Bauelementen, welche aus Halbleitern, Isolatoren und metallischen Dünnschichten bestehen. Diese Dünnschichten spielen eine wichtige Rolle in Bauelementen wie mikroelektromechanischen Systemen (MEMS). Metallische Filme, beispielsweise Cu, transportieren den elektrischen Strom zwischen den Halbleiterstrukturen und dienen bei entsprechender Dicke als Wärmesenke für die thermische Energie, generiert durch Joulesche Erwärmung. Während der Lebensdauer von miniaturisierten Cu-Strukturen müssen diese mehrere Milliarden thermischen Zyklen standhalten, welche Risse und einen frühzeitigen Ausfall verursachen können, wenn die Festigkeit des Metalls nicht ausreichend ist. In der vorliegenden Arbeit werden die mechanischen Eigenschaften von Cu-Dünnschichten mit unterschiedlicher Korngröße untersucht, um Einblick in die Verformungsmechanismen zu bekommen, um dadurch eine Lebensdauervorhersage und eine Optimierung der Materialeigenschaften zu ermöglichen. Miniaturisierte Zug- und Biegeproben wurden mittels eines fotolithographischen Prozesses hergestellt und in einer mikromechanischen Apparatur getestet, wobei die Experimente überwiegend im Rasterelektronenmikroskop (SEM) durchgeführt wurden.

Für die Untersuchung der statischen mechanischen Eigenschaften, wie Streckgrenze, Zugfestigkeit und Bruchdehnung, wurden Zugversuche zwischen 143 und 873 K durchgeführt. In diesen Experimenten wurden Aktivierungsenergien und -volumina ermittelt, wodurch in Folge die zugrundeliegenden Verformungs-mechanismen bestimmt werden konnten. Die Experimente bei erhöhten Temperaturen zeigten eine Versprödung im Material mit 2.7 µm Korngröße. Chemische Analysen und Berechnungen zu Segregation, Korngrenzenfestigkeit und Diffusion zeigten als Ursache für die Versprödung die Segregation von nichtmetallischen Elementen an die Korngrenze.

Da für praktische Anwendungen vor allem die dynamischen Eigenschaften von Interesse sind, wurden zyklische Kriechexperimente (Ratcheting) zwischen 293 und 673 K durchgeführt, wobei die gleichen Verformungsmechanismen wie im

Zugversuch gefunden wurden. Die Lebensdauer, welche stark von der Kriechdehnung pro Zyklus abhängt, konnte durch ein modifiziertes Basquin-Gesetz beschrieben werden. Da in Cu-Mikrostrukturen, welche in Bauelementen Verwendung finden, das Verhältnis von Maximal- zu Minimalspannung meist negativ ist, wurden ebenfalls Biegeversuche durchgeführt, um einen alternierenden Spannungszustand zu erreichen. Im Gegensatz zu den Ratcheting-Experimenten zeigte sich in den Biegeversuchen eine deutliche Ausbildung von Extrusionen und Intrusionen auf der Probenoberfläche sowie eine Zellstruktur im Probeninneren.

Durch Anwendung von Elektronenrückstreubeugung (EBSD) während der statischen und dynamischen Versuche konnte die Entwicklung der Dichte an geometrisch notwendigen Versetzungen (GND) und die Mikrostrukturentwicklung der Oberflächenkörner, welche das Verformungsverhalten in mikromechanischen Experimenten bestimmen, untersucht werden. Das Verformungsverhalten der Probenoberfläche, aufgenommen mittels in situ SEM, die gemessene GND Dichte sowie die abgeleiteten Aktivierungsenergien und –volumina verdeutlichten eine Verformung basierend auf Versetzungsplastizität. Nichtsdestotrotz, mit abnehmender Korngröße steigt der Einfluss von Korngrenzendiffusion bei erhöhten Temperaturen.

Die Ergebnisse dieser Arbeit sind in Form von vier Publikationen angefügt. Publikation A berichtet über Korngrenzenversprödung, welche im statischen Zugversuch zwischen 293 und 673 K gefunden wurde. Publikation B erläutert das Verformungsverhalten in statischen und dynamischen Zug-Zug-Versuchen bei Raumtemperatur, Publikation C erweitert diese Messungen durch Versuche im bisher unerreichten Temperaturbereich von 143 bis 873 K. Schließlich werden in Publikation D Biegeversuche bei Raumtemperatur, unter Zuhilfenahme von EBSD während des Experiments, behandelt. Die Ergebnisse verdeutlichen, dass das Mikrostrukturdesign eine ambivalente Wirkung hat, da sich der Einfluss der Mikrostruktur mit der Temperatur ändert. Statische und dynamische Experimente mit unterschiedlichen Dehnraten, unter Verwendung von SEM/EBSD, gaben Einblick auf Verformungs-mechanismen und zeigten einen Wechsel von makroskopischen zu mikroskopischen Materialeigenschaften im untersuchten Korngrößenbereich.

Felix qui potuit rerum cognoscere causas

Publius Vergilius Maro

Contents

1 Introduction

Cu thin films are of great interest for applications such as integrated circuits (ICs) and microelectromechanical systems (MEMS). There Cu is used in the conductive paths because of the high electrical and thermal conductivity of the metallic element. ENIAC, the first electronic general-purpose computer, allowed $5 \cdot 10^4$ point operations per second and occupied an area of 170 m² in 1946 [1]. The fastest computer in early 2014, Tianhe-2, allows $3.4 \cdot 10^{16}$ floating point operations per second onto an area of 720 m² [2, 3]. This demonstrates the tremendous speed of miniaturization of thin films in micro-electronic devices.

It has been shown, that small scale samples show a different behavior compared to bulk Cu samples and these mechanisms are well understood. However, thin film samples as used in semiconductor industries are in the transition regime between bulk-like and small scale behavior and deformation mechanisms in static and cyclic experiments have to be clarified. Since the millennium “More than Moore” is even more challenging the miniaturization of materials. Subsequently the size of real life Cu micro-structures constantly decreases, resulting in a change in deformation mechanisms as shown in static experiments, where surface grains dominate the deformation behavior if the sample dimension to grain size ratio decreases below a critical limit of five [4 - 6]. Also in fatigue experiments a change in deformation mechanisms was found, if the film thickness or grain size decreases below a critical limit of roughly 1 µm [7, 8], which is a typical thickness in real life thin films. Nevertheless, these experiments were only performed at room temperature without EBSD during the experiments, which would shed light on the deformation behavior of surface grains, dominating the strength of small scale samples [4].

In practical applications Cu microstructures are subject to cyclic loading at elevated temperatures with a positive mean stress due to thermal mismatch between the metallic thin film and the silicon substrate. Therefore, the mechanical properties of these films have to be investigated and optimized: excellent static mechanical properties are required to withstand peak loads and the cyclic mechanical behavior influences the lifetime during cyclic loading. In the past decades predominantly thermo-mechanical experiments were used to characterize thin film structures.

However, in these experiments the effects of temperature and mechanical stress are coupled and cannot be separated.

A further reduction in size of microelectronic devices results in a dramatic increase in power dissipation and, therefore, it is necessary to characterize and optimize the mechanical properties of metal thin films. The target of this work is to analyze the plasticity and fatigue behavior of freestanding Cu micro-samples over a wide range of temperature, grain sizes, strain rates and stress states. A comparison between the obtained mechanical data, deformation evolution, chemical analysis and simulations should give insights to deformation mechanisms.

References

1 HH Goldstine, A Goldstine, The Electronic Numerical Integrator and Computer (ENIAC), The Origins of Digital Computers, Springer, (1982).

2 J Dongarra, Visit to the National University for Defense Technology Changsha, China, (2013).

3 SH Chan, J Cheung, E Wu, H Wang, CM Liu, X Zhu, S Peng, R Luo, TW Lam, arXiv:1402.4876.

4 B Yang, C Motz, M Rester, G Dehm, Phil. Mag. 92, 25-27, (2012), 3243-3256.

5 XW Gu, CN Loynachan, Z Wu, YW Zhang, DJ Srolovitz, JR Greer, Nano Lett. 12, (2012), 6385-6392.

6 DC Jang, JR Greer, Scr. Mater. 64, (2011), 77.

7 GP Zhang, CA Volkert, R Schwaiger, E Arzt, O Kraft, J. Mater. Res. 20, 1, (2005), 201-207.

8 GP Zhang, CA Volkert, R Schwaiger, P Wellner, E Arzt, O Kraft, Acta Mater. 54, (2006), 3127-3139.

2 Basic concepts of plasticity and fatigue

In the following the basic principles of size dependent mechanical properties and hardening mechanisms will be described. Furthermore, the background of elastic and plastic deformation is presented introducing the differences between static and cyclic deformation. Finally the analysis tools employed in this study will be shortly shown. For continuative studies the reader is referred to the given references.

2.1 Size dependent mechanical properties

For macro-sized samples it is well known, that intrinsic parameters such as grain size or particle size influence the strength of materials significantly. For micro-sized samples, where the sample size is in the range of the grain size, also the sample dimension has strong impact on the mechanical properties [1].

2.1.1 Strengthening by reducing the grain size

The Hall-Petch effect, which describes the increase of flow stress σ with decreasing grain size d, is well known since more than 60 years [2, 3]:

$$\sigma = \sigma_0 + \frac{k_{HP}}{\sqrt{d}}, \tag{1}$$

where σ_0 [MPa] is a material constant (e.g. the lattice friction stress/Peierls stress) and k_{HP} [MPa $m^{0.5}$]is the Hall-Patch constant. However, in the past decades it has been shown that this relation is not valid for grain sizes in the nanometer range, where the Inverse-Hall-Petch effect was observed [4]. Furthermore it has been shown recently, that the increase in strength should scale better with ln(*d*) / *d* + *const*. instead of the well-known $d^{-0.5}$ + *const.* [5].

2.1.2 Influence of the sample dimension on deformation behavior

For macroscopic samples, especially brittle materials such as ceramics, the strength is increasing with decreasing sample dimension because with the smaller sample size the probability for containing defects becomes smaller [6, 7]. This behavior is also well known for microscopic metallic samples, as the density of dislocation sources is getting smaller [8, 9].

However, for micron-sized polycrystalline samples it has been observed, that at a constant grain size larger samples are stronger, caused by the sample size to grain size ratio $D : d$. This is caused by grains with a free surface to the environment as these can deform easily as there is no resistance against deformation from neighboring grains. Furthermore dislocations can escape to the free surface and do not contribute to dislocation hardening. If the $D : d$ ratio is large, i.e. the sample is significantly larger than the grain size, most grains are not in contact with the free surface and consequently show a high strength. If the $D : d$ ratio is small, many grains are on the free surface, dislocations can escape easily and there is less hardening during deformation [10 - 12]. In the case of $D : d < 1$ the cross-section is single-crystalline. If the grain size d is in the order of the sample dimension D, some cross-sections are polycrystalline, but there could be some areas with single-crystalline cross-section, which act as a “weakest link” [10].

2.1.3 Influence of the experimental mode on strength

In a tensile test, the cross-sectional area with the smallest number of grains has the highest probability to fail. However, if a static or cyclic bending experiment is performed, the highest stress appears close to the sample fixation [9]. Consequently, if a single-crystalline cross-section is close to the area with the highest stress in the outer fiber, the sample will fracture earlier as in the case where a polycrystalline cross-section is close to the sample foot, as dislocations can escape more easily in the single-crystalline cross-section [10].

2.2 Hardening mechanisms

Beyond the fact, that a small grain size increases the hardness and ductility of a material, it is well known, that the strength of metals can be increased by adding elements or precipitates to the matrix. Adding atoms, which are soluble in the metal matrix, can lead to solid solution hardening because of spherical or non-spherical distortions of the lattice [13 - 15]. In this case the hardening effect is dominated by the concentration, *c*, of the added element:

$$\tau_c \sim \sqrt{c} \text{ or } \tau_c \sim c^{\frac{2}{3}} \text{ [15]}, \tag{2}$$

where τ_c [MPa] is the critical shear stress. If elements are added, which are not soluble in the metal matrix, this can led to formation of coherent or non-coherent precipitations, where volume fraction and size of the precipitates dominate the hardening effect [16]. Furthermore it has been found, that the hardening effect of rods and plates is twice as strong as that of spherical particles [17]. If compounds are added as dispersions to a metal matrix this usually results in hardening caused by non-coherent particles (e.g. Y_2O_3 in oxide dispersion strengthened (ODS) alloys [18]).

Finally it is possible that grain boundaries are pinned by impurities. This is an important mechanism especially at elevated temperatures because precipitates prevent grain boundary sliding and grain growth [19 - 24]. These impurities (e.g. S or P) influence the strength of grain boundaries and can cause weakening or embrittlement [25, 26]. However, some impurities such as B [27] or Re [28] are well known to increase the strength of grain boundaries.

2.3 Static deformation of materials

2.3.1 Elastic deformation

If a sample is subject to a uniaxial mechanical loading the elastic behavior can be described by the Hooke's law [29]:

$$\sigma = E \bullet \varepsilon \,, \tag{3}$$

where σ [MPa] is the stress, E [GPa] the Young's modulus and ε the strain.

As long as the sample is loaded below the onset of plastic deformation, the yield strength σ_{ys}, there is a linear relationship between stress and strain, all deformation is reversible and after unloading the sample reaches the initial state [29]. Besides the strength the Young's modulus is also dependent on the length scale, e.g. in nanocrystalline (nc) materials this is caused by different atomic spacing in the grain boundary region [30 - 33].

2.3.2 Plastic deformation

If the elastic limit is exceeded, plastic (non-reversible) deformation starts in the material. Through hardening of the material, mainly caused by dislocation multiplication [34], the external stress constantly increases with increasing strain (strain hardening) [8, 35]. As for metals the volume is constant, with increasing strain the cross-sectional area decreases (geometrical weakening). As long as hardening of the material is stronger than geometrical weakening, the engineering stress, which refers to the initial cross-sectional area, increases. At a certain point, the geometrical weakening is as strong as hardening, the maximum stress, the ultimate tensile stress (UTS) is reached. From that point geometrical weakening is predominant and the engineering stress is decreasing. However, the true stress in the material refers to the current cross-sectional area and is increasing in the necking (lateral contraction) zone until fracture occurs.

Depending on the microstructure, hardening could be more or less distinctive. If the cross-section is single-crystalline (e.g. in a single-crystalline sample or polycrystalline sample with bamboo-structure), hardening is less pronounced as dislocations can escape easily through the free surface. In the case of a polycrystalline cross-section, the grains show stronger hardening as grains are supporting each other. To fulfill material coherence geometrically necessary dislocations (GNDs) are necessary and contribute to hardening. [8, 35, 36]

2.3.3 Dislocation plasticity

As mentioned above, to ensure integrity during plastic deformation of polycrystalline materials, GNDs are necessary (Fig. 1). These GNDs allow the grains to deform with respect to neighbor grains. Additionally there are statistically stored dislocations (SSDs), which are randomly generated during plastic deformation of materials [37 - 39] and are directly contributing to plastic straining in contrast to GNDs [40]. During inelastic deformation SSDs arrange in mosaic patterns where regions of high SSD densities (dislocation boundaries) are separating regions of low SSD densities [39].

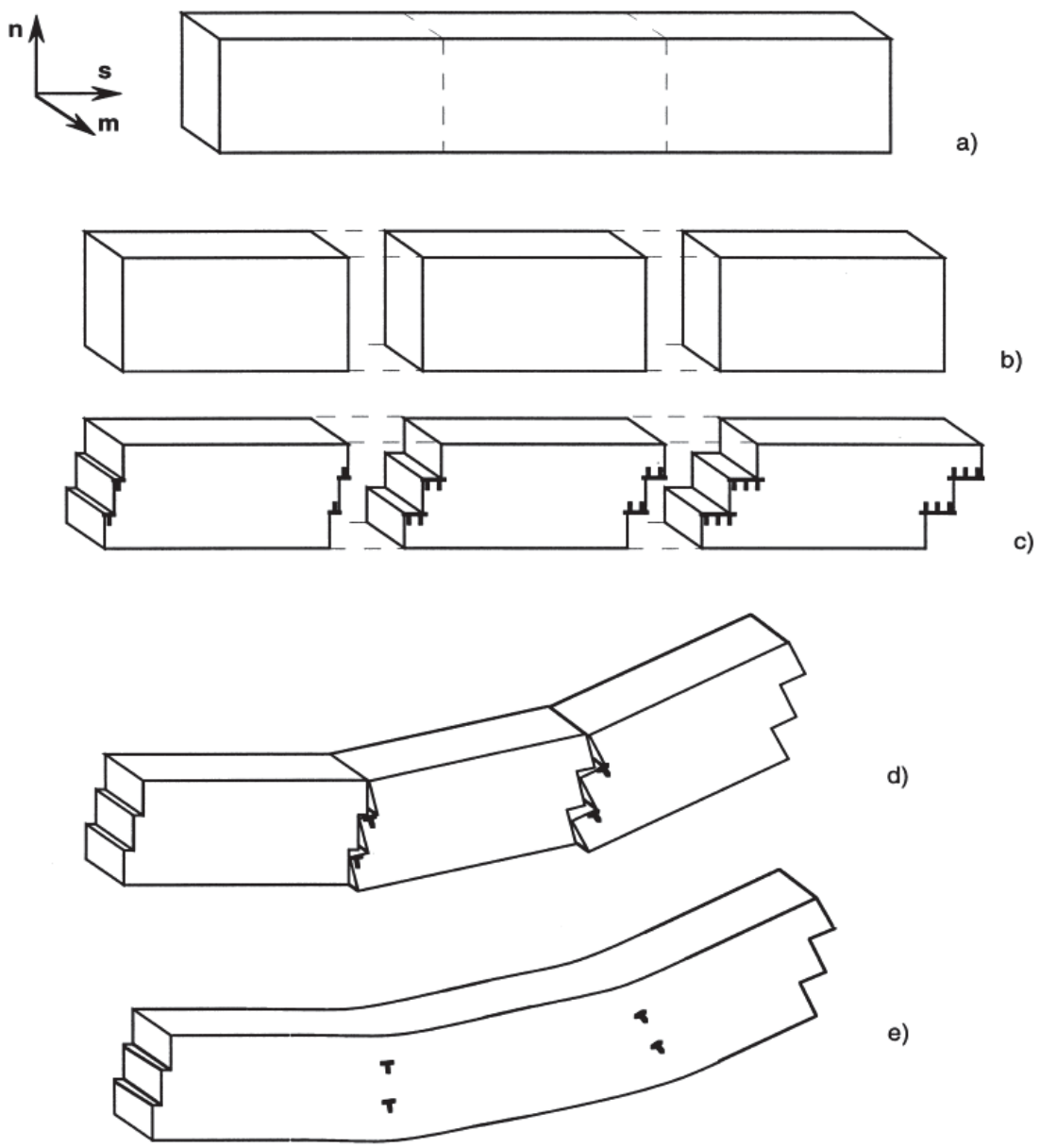

Fig. 1. Schematic process (a-e) of GND accumulation [38].

A single dislocation can split up into two partial dislocations and a stacking fault. For Cu the stacking fault energy is 78 mJ/m², which results in a small separation and consequently cross-slip is easily possible [41]. If a dislocation moves from one primary slip-plane to another, parallel slip plane using an intersecting slip-plane without changing the direction of the Burgers vector, this is called cross-slip (Fig. 2). If the dislocation is moving back from the intersecting slip-plane to the primarily slip plane this is called double cross-slip. Cross-slip plays an important role during dislocation multiplication and strain hardening [42].

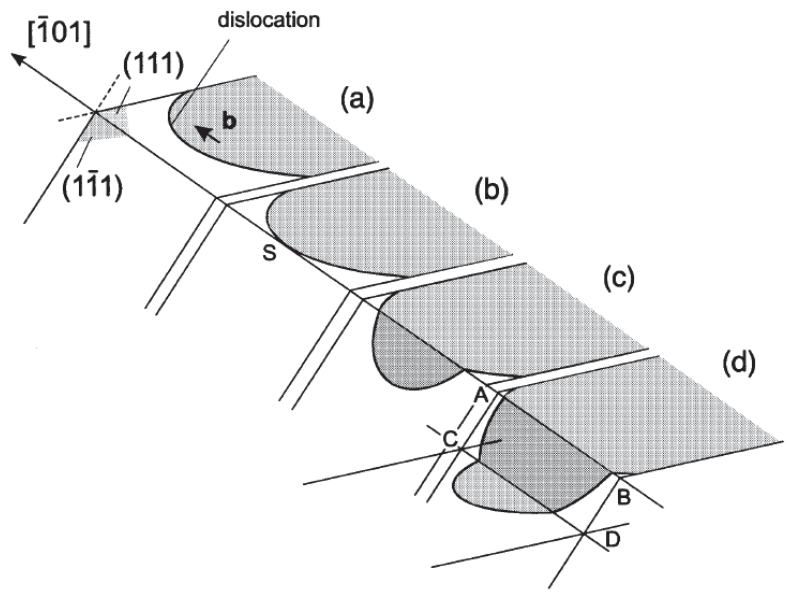

Fig. 2 Illustration of a cross-slip process (a-d) [8].

Another form of dislocation interaction is the formation jogs through dislocation cutting. The direction of a jog is parallel to the Burgers vector of the cutting dislocation; consequently the direction of the jog can vary. If the generated jogs have an edge character they move outside the slip-plane, called non-conservative motion (climb), generating vacancies or interstitial atoms dependent on the direction of movement. Kinks, which are a sub-form of jogs, have the same slip direction as the dislocation line and consequently they are moving in a slip plane, called conservative motion (glide). [43]

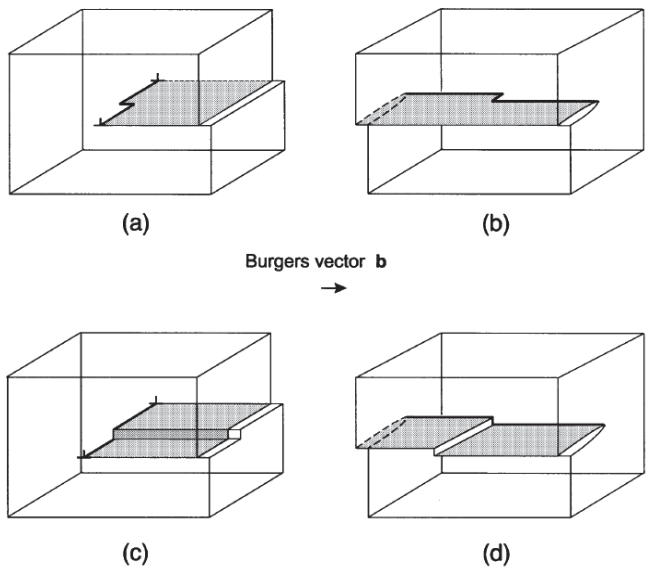

Fig. 3. Possible dislocation structures after dislocation-dislocation interaction. The Fig. illustrates a (a) kink in an edge dislocation, (b) kink in a screw dislocation, (c) jog in an edge dislocation and (d) jog in a screw dislocation [8].

2.3.4 Activation energy

It is well known, that chemical reactions have activation energies, which can be seen as barriers to start a chemical reaction, which can be overcome by catalysts or thermal activation. Plastic deformation mechanisms also have an activation energy. The activation energy can be determined by analyzing the temperature dependence of the yield strength [44]. If the yield strength shows no temperature dependence, this indicates that the processes during deformation are not thermally activated. If the temperature shows a strong effect on the yield strength this can lead back to thermally activated processes as grain boundary or lattice diffusion. Typical values for activation energies are given in Tab. 1.

Tab. 1. Activation energies *Q* for different processes in metals.

Process	*Q* [kJ/mol]	Ref.
Cross-slip	30 - 64	[42]
Grain boundary diffusion	72.47 - 104	[45, 46]
Lattice self-diffusion Non-conservative motion	100 - 200	[47]
Lattice self-diffusion	200	[48]

2.3.5 Activation volume

If a dislocation is moving through a crystal it can interact with obstacles such as particles, interstitials or dislocations. These obstacles (Fig. 4) hinder movement of the dislocation. However, the dislocation segment between the obstacles is expanding and the dislocation shifts the obstacle for a small distance *Δy**, the activation length, as a result of the external stress. If this activation length is multiplied with the dislocation segment length λ, the activation area *Δa** is obtained, which finally gives the activation volume *V** [36, 49, 50] when multiplied with the Burgers vector *b*:

$$V^* = \Delta y^* \bullet \lambda \bullet b \tag{4}$$

If the stress on the dislocation is further increased it can overcome the obstacle and return to its relaxed shape. The activation volume ranges typically from 1 to 1,000 b³ as given in Tab. 2. Note, that ultrafine-grained (ufg) and nanocrystalline (nc) materials show significantly lower activation volumes [51] as given in Tab. 2.

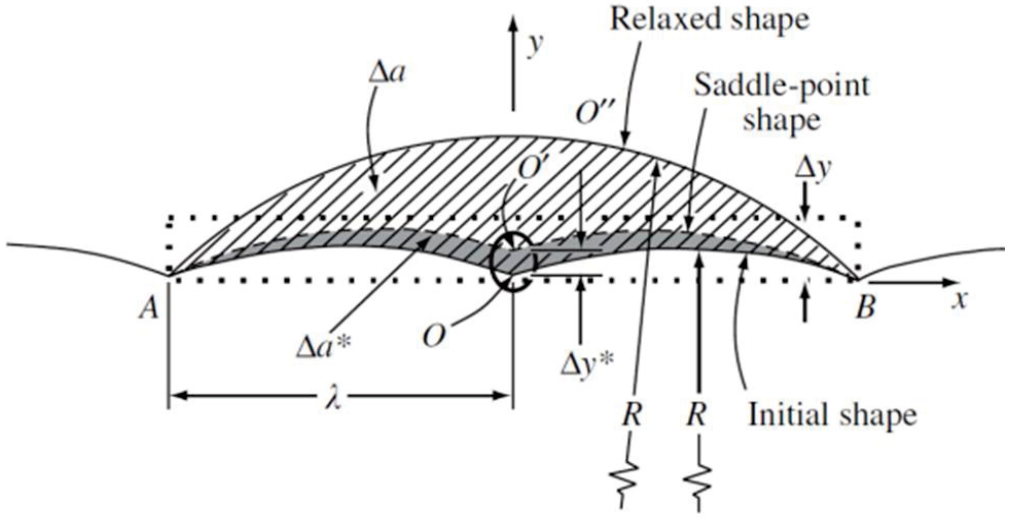

Fig. 4. Schematic drawing of the activation volume [36]. *A, O* and *B* are the obstacles in the initial positions, *O'* is the position of the shifted obstacle and *O''* the position of the obstacle after relaxation. *R* displays the force on the moving dislocation. *Δy** is the activation length, *Δa** is the activation area.

Tab. 2. Activation volumes V^* for different deformation mechanisms.

Mechanism	V^* [b^3]	Ref.
Coble creep	≈ 1	[52]
Grain boundary diffusion	1 - 10	[53]
Kink-pair movement Peierls–Nabarro barriers Dislocation-boundary interactions Grain-boundary shear	≈ 10	[53]
Cross slip	10 - 100	[52]
Dislocation glide, grain boundary sliding	≈ 44 (ufg Cu)	[51]
Punching of mobile dislocations through a dense bundle of grain boundaries Emission of dislocation from grain boundaries De-pinning of a propagating dislocation pinned by grain boundaries	29 ($\dot{\varepsilon}$ = 11,000 s^{-1}) - 53 ($\dot{\varepsilon}$ = 0.001 s^{-1})	[54]
Forest dislocation cutting	100 – 1,000	[53]

2.4 Cyclic deformation of materials

Cyclic deformation is described by the stress ratio R and mean stress σ_{mean}:

$$R = \frac{\sigma_{\min}}{\sigma_{\max}}, \tag{5}$$

$$\sigma_{\text{mean}} = \frac{\sigma_{\max} + \sigma_{\min}}{2}, \tag{6}$$

where σ_{min} [MPa] is the minimum stress and σ_{max} [MPa] the maximum stress (Fig. 5). Consequently - ∞ ≤ R ≤ ∞ (Fig. 5a) and three major cases are possible (Fig. 6): In the case of R = 0 (Fig. 6b), which means σ_{min} = 0, the material undergoes a combined cyclic and static stress with a positive σ_{mean}. For R = - 1 (Fig. 6c), σ_{min} = - σ_{max} indicating a typical fatigue experiment with σ_{mean} = 0. For R = - ∞ (Fig. 6d), which indicates σ_{max} = 0, the material undergoes a combined cyclic and static stress with a negative σ_{mean} (Fig. 5b). The fourth, trivial case is R = 1 which is a static (creep) test with constant load (σ_{min} = σ_{mean} = σ_{max}). If 0 ≤ R ≤ 1, there is a steady tensile stress and the experiment can be described as a cyclic creep experiment, also known as ratcheting [55]. If R < 0, in each cycle tension and compression stress is applied to

the material, resulting in typical fatigue behavior with intrusions and extrusions on the free surface and fatigue structures (dislocation wall/cell structures, persistent slip bands (PSBs)) inside the material [56 - 58].

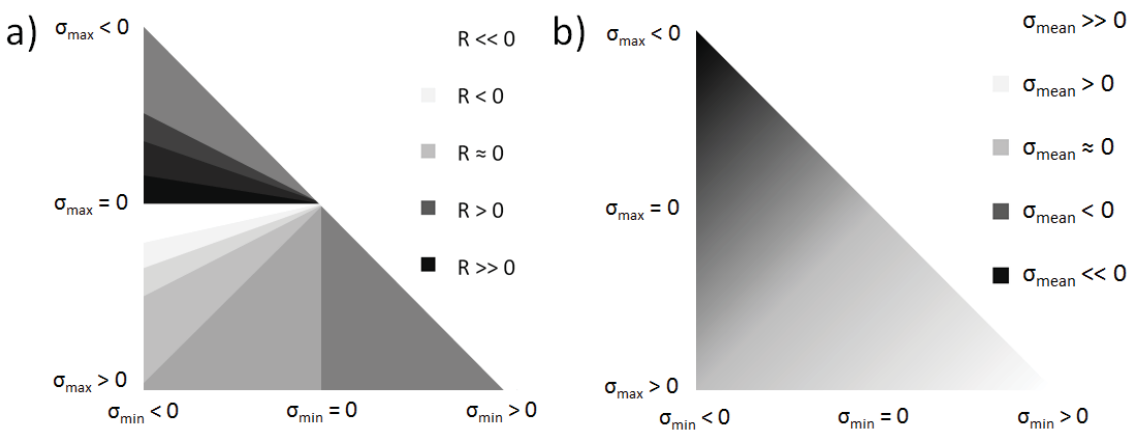

Fig. 5. (a) Stress ratio R and (b) mean stress σ_{mean} as a function of the minimum stress σ_{min} and maximum stress σ_{max}.

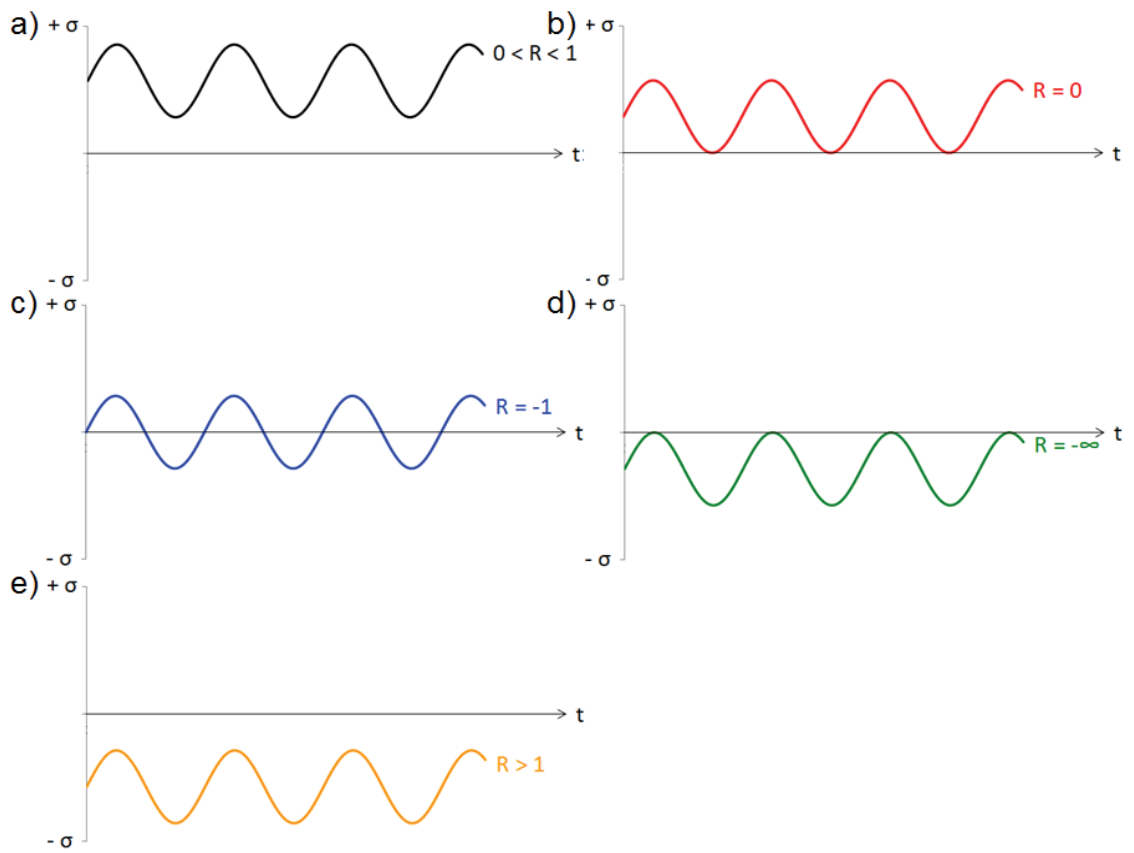

Fig. 6. Experimental modes for cyclic experiments. (a), (b), (c) and (e) show ratcheting experiments, (d) demonstrates a typical fatigue experiment. In the displayed case the stress follows a sinusoidal curve, however also other curve forms are possible (e.g. a square-curve stress).

2.4.1 Ratcheting

If the mean stress $\sigma_{mean} \neq 0$ the experiment can be described as a combined creep and fatigue experiment, a ratcheting experiment, also called cyclic creep experiment [59]. Two cases can be distinguished: Firstly experiments, where $\sigma_{max} > \sigma_{min} \geq 0$ (or $0 \geq \sigma_{max} > \sigma_{min}$), showing only pulsating tension (or compressive) stress during the whole experiment. In that case any plastic deformation is irreversible and the plastic deformation accumulates during the experiment. Secondly, if $\sigma_{max} > -\sigma_{min} \geq 0$, during the first half cycle the stress is positive and during the second half cycle the stress is negative (or vice versa). This means, that deformation of the first half cycle will be reversed to some extend during the second half cycle, resulting in fatigue deformation of the material. However, as $\sigma_{mean} \neq 0$ there will be also a superposed creep deformation.

2.4.2 Fatigue

If the mean stress is equal to zero ($\sigma_{mean} = 0$) then the experiment can be described as a typical fatigue experiment. During the first half cycle the material is plastically deformed and reversibly deformed during the second half cycle, resulting in a hysteresis. The area inside the hysteresis curve is a measure for the energy (work) absorbed by the material. Typically fatigue experiments are performed as bending experiments, as dog-bone shaped sample could buckle if the aspect ratio is too large. [60] Furthermore thermo-mechanical experiments on a substrate (e.g. Al on Si) show typical fatigue damage [61]. During cyclic loading dislocations accumulate on obstacles (e.g. grain boundaries). If now the stress is relieved, a reversal flow is observable above a stress level of 0, the so-called Bauschinger effect [62]. During the first 10-100 cycles of a fatigue experiment strain hardening is observed and the maximum stress increases in a strain controlled bending experiment. After several 100-1,000 cycles dislocation wall/cell structures and finally persistent slip bands (PSBs) are formed [56]. These PSBs cause extrusions/intrusions on the surface and allow easy slip of dislocations, fostering localized deformation, and decreasing the maximum stress due to fatigue damage. Finally, cracks are initiated on extrusions/intrusions and the sample fractures. If the grain boundary or sample size is below 1-3 µm [63 - 64], there is not enough space for the formation of dislocation wall/cell structures and PSBs. Subsequently these structures do not exist, the deformation mechanisms are changing and cracks originate at grain boundaries. [63]

2.4.3 Comparison between fatigue and ratcheting

If $-\infty < R < 0$ the material shows a combination of fatigue and creep deformation. If $R = -\infty$ or $R > 0$ the material only shows creep deformation and all plastic deformation is non-reversible [65, 66].

However, for both cases it is possible to make lifetime predictions. For typical fatigue deformation the well-known Coffin-Manson equation [67, 68] is used in the low cycle fatigue (LCF) regime with $< 10^5$ cycles to failure. In the high cycle fatigue (HCF) regime with $> 10^4$ cycles to failure the Basquin equation [69] is used. For experiments with combined fatigue/creep deformation the lifetime can be described by the modified Goodmann equation [70, 71], the Smith–Watson–Topper (SWT) parameter [72], the Walker parameter [73] and Park et al.'s ratcheting-modified SWT parameter [74, 75].

2.5 *In situ* micromechanical experiments and analysis tools

2.5.1 *In situ* scanning electron microscopy

In situ scanning electron microscopy (SEM) experiments have several advantages compared to *in situ* light optical microscopy (LOM) experiments. First, the SEM allows a much higher lateral resolution compared to LOM and the high vacuum (10^{-5} - 10^{-7} mbar) inside the SEM decouples the device from thermal fluctuations. The absence of oxygen allows experiments at elevated temperatures without significant oxidation, which also has significant influence on the fatigue behavior [76, 77]. However, *in situ* SEM experiments give only information of the samples surface, while *in situ* transmission electron microscopy (TEM) or *in situ* EBSD can deliver information about crystal orientation and dislocations. Furthermore TEM can deliver information about the chemical composition with atomic resolution.

2.5.2 *In situ* electron backscatter diffraction

For *in situ* EBSD measurements the sample has to be tilted (e.g. 70°) to obtain high quality Kikuchi patterns. For *in situ* SEM experiments images can be taken during deformation, as imaging time is in the order of some seconds. In the case of *in situ*

EBSD experiments the deformation can be also continued during imaging, as long as the imaging time is short. This is only the case if the EBSD pattern of a spot or a line ("line scan") is analyzed. In the case of extended areas ("area scan") a compromise between recording time and pattern quality must be found. In the case of area scans with several thousand points and an imaging time in the order of several minutes, the experiment has to be stopped, implicating relaxation during imaging. However, as long as experiments are performed at room temperature the influence of relaxation should be negligible. However experiments should be called *in situ* like EBSD as experiments are intermitted for recording of the EBSD images.

Up to now, *in situ* EBSD measurements were performed for self-annealing of copper at ambient temperatures [78], during *in situ* heat treatment for various materials [79], rock salt up to 723 K [80], tantalum up to 1,453 K [81] and Cu up to 773 K [82, 83]. Furthermore, the phase transformation of α-Ti to β-Ti at 1,155 K has been observed by *in situ* EBSD, showing nucleation and growth of β-Ti at the α-Ti grain boundaries [84].

EBSD measurements during *in situ* mechanical testing of macro-sized samples have been performed for Al single crystals [85], Ti6Al4V [86], solder joints [87] and polycrystalline Cu [88]. EBSD measurements during *in situ* compression of micron-sized single-crystalline GaAs pillars were performed with sub-100 nm resolution, showing reversible bending of the micro-pillars up to 3° [89].

2.5.3 Atom probe tomography

Atom probe tomography (APT) was invented about 30 years ago based on field ion microscopy. For analysis a sharp tip with a tip radius < 50 nm is prepared, either by electro-polishing [90] or lift-out technique [91, 92, 93, 94, 95]. This tip is now introduced in an ultra-high vacuum (UHV) chamber and between the tip and a counter electrode an electrical field is applied (Fig. 7). Through the small tip radius the atoms on the surface are field evaporated either by voltage or laser pulses and detected by a time-of-flight mass spectrometer. This allows identification of atoms and their bonding relations with atomic resolution. However, in the APT it is impossible to differ between ions with the same mass to charge ratio as ions are identified in a time-of-flight mass spectrometer. Consequently it is hard to distinguish

between S and O atoms, which can have a detrimental influence on the strength of Cu [96, 97]. O ions are mainly single charged ($^{16}O^{+}$), as O is easy to field evaporate, S ions are mainly double charged (95 % $^{32}S^{+2}$ and 5 % $^{34}S^{+2}$), as S is hard to field evaporate [98]. As a consequence, for a small number of atoms it is not possible to distinguish between $^{16}O^{+}$ and $^{32}S^{+2}$ (mass to charge ratio ≈ 16). The only possibility to distinguish between O and S is to detect a large number of atoms with a good mass resolution to be able to find a $^{32}S^{+2}$ peak at 16 and a $^{34}S^{+2}$ peak at 17. The ratio between ^{32}S and ^{34}S is 20 : 1, consequently for the identification of S it is necessary to find a peak at a mass to charge ratio of 16 and a ≈ 20 times smaller peak at 17, which can be only found at a low noise level. Furthermore under poor vacuum conditions residual H_2O is present in the APT chamber and gets ionized and may cause an OH^{+} peak which could cover a $^{34}S^{+2}$ peak.

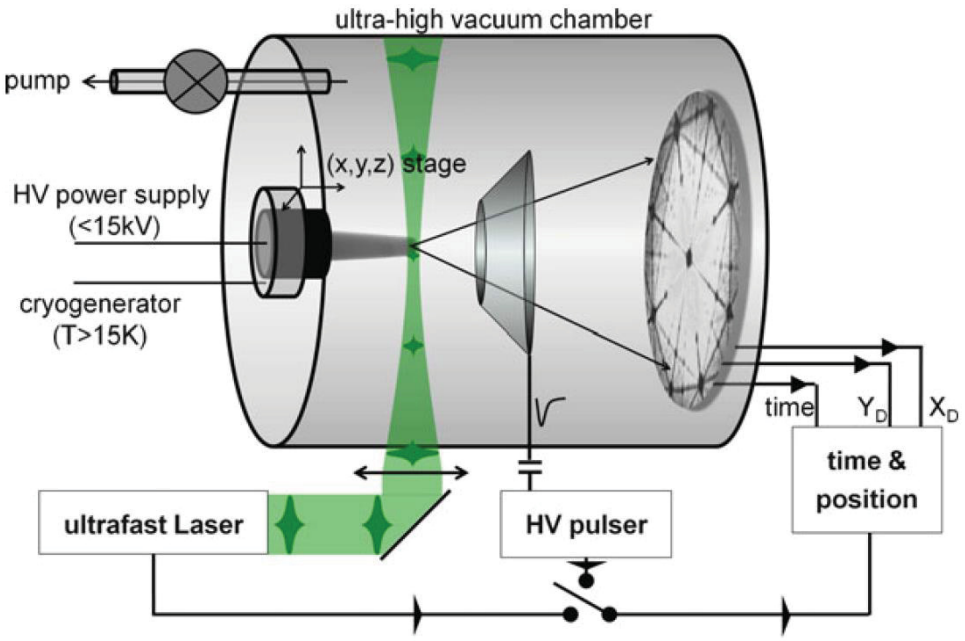

Fig. 7. Basic principle of APT [99]

References

1 MD Uchic, DM Dimiduk, JN Florando, WD Nix, Science 305, 5686, (2004), 986-989.

2 EO Hall, Proc. Roy. Soc. B 64, (1951), 747-753.

3 NJ Petch, J. Iron Steel 174, (1953), 25-28.

4 CE Carlton, PJ Ferreira, Acta Mater. 55, (2007), 3749-3756.

5 DJ Dunstan, AJ Bushby, Int. J. of Plast. 53, (2014), 56-65.

6 W Weibull, Ingeniors Vetenskamp Akademien, Handlingar, 151, (1939), 5.

7 W Weibull, J. Appl. Mech., (1951), 293-297.

8 D Hull, DJ Bacon, Introduction to dislocations, Butterworth Heinemann, Oxford, (2001).

9 D Kiener, W Grosinger, G Dehm, R Pippan, Acta Mater. 56, (2008), 580-592.

10 B Yang, C Motz, M Rester, G Dehm, Phil. Mag. 92, 25-27, (2012), 3243-3256.

11 XW Gu, CN Loynachan, Z Wu, YW Zhang, DJ Srolovitz, JR Greer, Nano Lett. 12, (2012), 6385-6392.

12 DC Jang, JR Greer, Scr. Mater. 64, (2011), 77.

13 RL Fleischer, Solid Solution Hardening, Reinhold Publishing Corp., New York, 1964.

14 R Labusch, phys. stat. sol. 41, (1970), 659-669.

15 R Labusch, Acta Metall. 20, 7, (1972), 917-927.

16 A Kelly, RB Nicholson, Prog. Mater. Sci. 10, 3, (1963), 151-191.

17 PM Kelly, Scr. Metall. 6, (1972), 647-656.

18 L Zhang, S Ukai, T Hoshino, S Hayashi, X Qu, Acta Mater. 57, (2009), 3671-3682.

19 JS Smart Jr., Butts A (Ed.), Rheinhold Publishing Corp., NY, Ch 19, (1954), 4102.

20 WH Bowyer, RL Crocker, SKI report 96:27.

21 M Stangl, PhD thesis, TU Dresden, (2007), 8-12.

22 HD Merchant, WC Liu, LA Giannuzzi, JG Morris, Materials Char., 53, (2004), 335-360.

23 J Neuner, I Zienert, A Peeva, A Preuße, P Kücher, JW Bartha, Microel. Eng., 87, (2010), 254-257.

24 VA Vas'ko, I Tabakovic, SC Riemer, MT Kief, Microel. Eng., 75, (2004), 71-77.

25 PJ Henderson, SKB technical report 92-04.

26 PJ Henderson, R Sandström, Mat. Sci. Eng. A 246, (1998), 143-150.

27 CT Liu, CL White, JA Horton, Acta metall. 33, 2, (1982), 213-229.

28 JH Liao, HY Bor, CG Chao, TF Liu, Mat. Trans. 52, 10, (2011), 1989-1997.

29 AC Ugural, SK Fenster, Advanced Strength and Applied Elasticity, 4th Edition, (2003).

30 JB Adams, WG Wolfer, SM Foiles, Phys. Rev. B 40, (1989), 9479-9484.

31 I Alber, JL Bassani, M Khantha, V Viter, GJ Wang, Philos. Trans. Roy. Soc. London A 339, (1992), 555-586.

32 JL Bassani, V Vitek, I Alber, Acta Metall. Mater. 40, (1992), S307 - S320.

33 MD Kluge, D Wolf, JF Lutsko, SR Phillpot, J. Appl. Phys. 67, (1990), 2370-2379.

34 L Johnson, MF Ashby, Acta Metall. 16, (1968), 219-225.

35 GE Dieter, Mechanical Metallurgy, McGraw Hill, (1988).

36 AS Argon, Strengthening Mechanisms in Crystal Plasticity, Oxford University Press, (2008), 51.

37 NA Fleck, GM Muller, MF Ashby, JW Hutchinson, Acta Metall. Mater. 42, 2, (1994), 475-487.

38 A Arsenlis, DM Parks, Acta mater. 47, 5, (1999), 1597 – 1611.

39 O Rezvanian, MA Zikry, AM Rajendran, Proc. R. Soc. A 463, (2007), 2833-2853.

40 LP Evers, WAM Brekelmans, MGD Geers, J. of the Mech. and Phys. of Sol. 52, (2004), 2379-2401.

41 EA El-Danafa, A Al-Mutlaqa, MS Solimana, Mat. Sci. Eng. A 528, (2011), 7579-7588.

42 SI Rao, DM Dimiduk, TA Parthasarathy, J El-Awady, C Woodward, MD Uchic, Acta Mater. 59, (2011), 7135-7144.

43 WF Hosford, Mechanical Behavior of Materials, Cambridge University Press, (2005), 163-165.

44 A Smolej, B Skaza, M Fazarinc, RMZ – Materials and Geoenvironment 56, 4, (2009), 389-399.

45 HJ Frost, MF Ashby, Deformation-mechanism maps, Pergamon Press, Oxford, (1982).

46 T Surholt, C Herzig, Acta Mater. 45, 9, (1997), 3817-3823.

47 M Pahutova, J Cadek, P. Rys, Phil. Mag. 23, 183, (1971), 509-517.

48 DB Butrymowicz, JR Manning, ME Read, J. Phys. Chem. Ref. Data 2, 3, (1973), 643-648.

49 H Conrad, Acta Metall. 6, (1958), 339-350.

50 H Conrad, H Wiedersich, Acta Metall. 8, (1960), 128-130.

51 KV Ivanov, EV Naydenkin, Mat. Sci. Eng. A 608, (2014), 123-129.

52 YM Wang, AV Hamza, Appl. Phys. Lett. 86, (2005), 241917.

53 MA Meyers, A Mishra, DJ Benson, Prog. Mat. Sci. 51, (2006), 427-556.

54 S Tao, D Qiong, Mechanics of Materials 43, (2011), 111-118.

55 CB Lim, KS Kim, JB Seong, Int. J. Fat. 31, (2009), 501-507.

56 H Mughrabi, Mat. Sci. Eng. 33, (1978), 207-223.

57 HW Höppel, M Kautz, C Xu, M Murashkin, TG Langdon, RZ Valiev, H Mughrabi, Int. J. of Fat. 28, (2006), 1001-1010.

58 H Mughrabi, HW Höppel, Int. J. of Fat. 32, (2010), 1413-1427.

59 G Kang, Int. J. of Fat. 30, (2008), 1448-1472.

60 S Suresh, Fatigue of Materials, Cambridge Solid State Science Series, Second Edition, (1998).

61 W Heinz, R Pippan, G Dehm, Mat. Sci. Eng. A 527, (2010), 7757-7763.

62 J Bauschinger, Mittheilungen aus dem mechanisch-technischen Laboratorium der k. technischen Hochschule in Munchen, 13, Ch. 5, (1881), 31.

63 GP Zhang, CA Volkert, R Schwaiger, E Arzt, O Kraft, J. Mater. Res. 20, 1, (2005), 201-207.

64 GP Zhang, CA Volkert, R Schwaiger, P Wellner, E Arzt, O Kraft, Acta Mater. 54, (2006), 3127-3139.

65 S Date, H Ishikawa, T Otani, Y Takahashi, Nucl. Eng. and Design 238, (2008), 336-346.

66 H Kemper, B Weiss, R Stickler, Eng. Fract. Mech. 32, 4, (1989), 591-600.

67 LF Coffin, Jr. Trans. ASME 76, (1954), 931-950.

68 SS Manson, NACA TN-2933, National Advisory Committee for Aeronautics, (1954).

69 OH Basquin, Proc. Am. Soc. Test. Mater. 10, (1910), 625-630.

70 J Goodman, Mechanics applied to engineering. London: Longmans, Green and Co., (1919).

71 JO Smith, Bulletin No. 334, University of Illinois, Engineering Experiment Station, Urbana, IL, (1942).

72 RN Smith, P Watson, TH Topper, J. Mater JMLSA 5, 4, (1970) 767-778.

73 K Walker, ASTM STP 462, American Society for Testing Materials, Philadelphia; (1970), 1-14.

74 SJ Park, KS Kim, HS Kim, Fatigue Fract. Eng. Mater. Struct. 30, 11, (2007), 1076-1083.

75 CB Lim, KS Kim, JB Seong, Int. J. of Fat. 31, (2009), 501-507.

76 FJ Bradshaw, C Wheeler, Int. J. of Fract. Mech. 5, 4, (1969), 255-268.

77 JD Frandsen, NE Paton, HL Marcus, Metall. Trans. 5, (1974), 1655-1661.
78 N Alshwawreh, M Militzer, D Bizzotto, JC. Kuo, Microel. Eng. 95, (2012), 26-33.
79 J Wheeler, A Cross, M Drury, RM Hough, E Mariani, S Piazolo, DJ Priora, Scripta Mater. 65, (2011), 600-603.
80 M Bestmann, S Piazolo, CJ Spiers, DJ Prior, Journal of Structural Geology 27, (2005), 447-457.
81 N Bozzolo, S Jacomet, RE Logé, Materials characterization 70, (2012), 28-32.
82 K Mirpuri, H Wendrock, S Menzel, K Wetzig, J Szpunar, Microel. Eng. 76, (2004), 160-166.
83 K Mirpuri, H Wendrock, K Wetzig, J Szpunar, Microel. Eng. 83, (2006), 221-235.
84 GGE Seward, S Celotto, DJ Prior, J Wheeler, RC Pond, Acta Mater. 52, (2004), 821-832.
85 JH Han, DI Kim, KK Jee, KH Oh, Mat. Sci. Eng. A 387–389, (2004), 60-63.
86 MB Mathisen, Master thesis, NTNU Trondheim, (2012).
87 QK Zhang, ZF Zhang, Scripta Mater. 67, (2012), 289-292.
88 S Ifergane, Z Barkay, O Beeri, N Eliaz, J. Mater. Sci. 45, (2010), 6345-6352.
89 C Niederberger, WM Mook, X Maeder, J Michler, Mat. Sci. Eng. A 527, (2010), 4306-4311.
90 Y Aruga, DW Saxey, EA Marquis, A Cerezo, GDW Smith, Ultramicroscopy 111, (2011), 725-729.
91 MK Miller, KF Russell, GB Thompson, Ultramicroscopy 102, (2005), 287-298.
92 DW Saxey, JM Cairney, D McGrouther, T Honma, SP Ringer, Ultramicroscopy 107, (2007), 756-760.
93 MK Miller, KF Russell, Ultramicroscopy 107, (2007), 761-766.
94 JM Cairney, DW Saxey, D McGrouther, SP Ringer, Physica B 394, (2007), 267-269.
95 F Pérez-Willard, D Wolde-Giorgis, T Al-Kassab, GA López, EJ Mittemeijer, R Kirchheim, D Gerthsen, Micron 39, (2008), 45-52.
96 TG Nieh, WD Nix, Met. Trans A 12A, (1981), 893-901.
97 PJ Henderson, R Sandström, Mat. Sci. Eng. A, 246, (1998), 143-150.
98 K Hayek, O Frank, WA Schmidt, JH Block, Berichte der Bunsengesellschaft für physikalische Chemie 81, 3, (1977), 262–268.
99 B Gault, MP Moody, JM Cairney, SP Ringer, Atom Probe Microscopy, Springer, (2012).

3 Conclusion

It has been shown, that general statements such as “smaller is stronger” or “a small grain size is favorable” are only valid at a defined set of parameters. For submicron, single-crystalline samples “smaller is stronger” is valid. But, for polycrystalline samples in some cases the opposite trend can be observed if the sample size to grain size ratio D : d decreases below a critical limit. While at room temperature a small grain size is favorable, at elevated temperatures a small-grained material can show embrittlement caused by grain boundary segregation of non-metallic elements. Through a heat treatment impurities can be removed from grain boundaries by diffusion to the free surface and embrittlement disappears. However, annealing also increases the grain size and consequently decreases the strength. Through alloying prior to the heat treatment the decrease in strength could be extenuated through solid solution hardening. However, if impurities segregate from the grain boundaries to the surface of the material this can lead to interface embrittlement in multilayer systems.

For cyclic experiments the stress ratio R and mean stress σ_{mean} dominate the failure mode: While for cyclic experiments with $\sigma_{mean} = 0$ (cyclic bending experiments) fatigue damage is dominating, for cyclic experiments with σ_{mean}, σ_{max}, $\sigma_{min} > 0$ (cyclic creep, ratcheting) the deformation mechanisms are comparable to a tension test.

Through *in situ* like EBSD it was possible to get insights to deformation mechanisms during static and cyclic deformation and make a rough estimate of the internal strength based on the Taylor factor, grain size, dislocation density and the ratio between sample dimensions and grain size.

Based on this findings it is possible to optimize the microstructure of thin films in microelectronic devices and consequently assist a further continuation of Moore‘s law. Dependent on the strain rate, application temperature and thin film dimensions different parameters such as impurity level and subsequently grain size have to be optimized, as these are influencing the transition from bulk-like to small-scale behavior. Based on the microstructural observations estimations of the static and cyclic strength are possible, making a significant reduction of material testing costs possible. As metallic thin films in practical applications are only one component of a complex thin film system, interactions, especially on the grain boundaries and interfaces, have to be considered to optimize the system lifetime.

4 Appended papers

Paper A

Temperature dependent transition of intragranular plastic to intergranular brittle failure in electrodeposited Cu micro-tensile samples

A. Wimmer, M. Smolka, W. Heinz, T. Detzel, W. Robl, C. Motz, V. Eyert, E. Wimmer, F. Jahnel, R. Treichler, G. Dehm

submitted manuscript (2014)

Paper B

Damage evolution during cyclic tension–tension loading of micron-sized Cu lines

A. Wimmer, A. Leitner, T. Detzel, W. Robl, W. Heinz, R. Pippan, G. Dehm

Acta Materialia 67, (2014), 297–307

Paper C

Micro-tension and ratcheting study of miniaturized Cu lines at variable temperature

A. Wimmer, W. Heinz, A. Leitner, T. Detzel, W. Robl, C. Kirchlechner, G. Dehm

submitted manuscript (2014)

Paper D

Cyclic bending experiments on freestanding Cu micron lines observed by EBSD

A. Wimmer, W. Heinz, T. Detzel, W. Robl, M. Nellessen, C. Kirchlechner, G. Dehm

to be submitted

Paper A

Temperature dependent transition of intragranular plastic to intergranular brittle failure in electrodeposited Cu micro-tensile samples

A. Wimmer [a], M. Smolka [b], W. Heinz [a], T. Detzel [c], W. Robl [d], C. Motz [e], V. Eyert [f], E. Wimmer [f], F. Jahnel [g], R. Treichler [g], G. Dehm [h]

a Kompetenzzentrum Automobil- und Industrie-Elektronik GmbH, A-9524 Villach, Austria
b Institute of Sensor and Actuator Systems, Vienna University of Technology, A-1040 Vienna, Austria
c Infineon Technologies Austria AG, A-9500 Villach, Austria
d Infineon Technologies Germany AG, D-93049 Regensburg, Germany
e Chair Experimental Methods of Material Science, University of Saarland, D-66123 Saarbrücken, Germany
f Materials Design SARL, F-92120 Montrouge, France
g Siemens AG, Otto Hahn Ring 6, D-81739 München, Germany
h Max-Planck-Institut für Eisenforschung GmbH, D-40237 Düsseldorf, Germany

submitted manuscript (2014)

Abstract

Smaller grain sizes are known to improve the strength and ductility of metals by the Hall-Petch effect. Consequently, metallic thin films and structures which must sustain mechanical loads in service are deposited under processing conditions leading to a fine grain size. In this study, we reveal that at temperatures as low as 473 K the failure mode of 99.99 at% pure electro-deposited Cu can change from ductile intragranular to brittle intergranular fracture. The embrittlement is accompanied by a decrease in strength and elongation to fracture. Chemical analyses indicate that the embrittlement is caused by impurities detected at grain boundaries. *In situ* micromechanical experiments in the scanning electron microscope and atomistic simulations are performed to study the underlying mechanisms.

1 Introduction

Cu is widely used as a metallization material in microelectronic devices, light emitting diodes, and micro-electromechanical systems. While the excellent electrical and thermal conductivity are the main tasks for the Cu metallization, its functionality is also strongly bound to the mechanical performance. Thus, it is of paramount interest to measure the stress-strain response of thin film materials and small scale structures at different temperatures. The main method to study the mechanical response of thin films is the wafer curvature approach where the thermal mismatch between film and substrate is utilized to strain the film [1, 2]. This technique mimics the thermo-mechanical exposure occurring in devices due to Joule heating and/or external temperature fluctuations but complicates an interpretation of the underlying deformation mechanisms as temperature and stress are always coupled and the strain is limited to typically less than 1 % [3]. The other most frequently used approach for mechanical testing of thin films is nanoindentation, which provides hardness and (reduced) Young's modulus values, but is not capable of providing full stress-strain curves and strain to failure [4, 5]. In the last decade, several miniaturized mechanical testing methods have been developed, which permit to perform quantitative measurements on small scale compression [6], tension [7], and bending [8] samples. Recently, Smolka et al. put the approach of miniaturizing forward by implementing a resistance heating system into a miniaturized test rig

which can perform tension tests on micron-sized samples inside a scanning electron microscope (SEM) at temperatures up to 673 K with a load resolution of 10 µN [9]. Thus, the mechanical properties of freestanding thin films can be measured without any influence of the thermal mismatch and consequently stress between the metal thin film and the substrate at variable temperatures and analyzed with respect to their microstructure.

In this study we focus on electrodeposited Cu films, which have, dependent on the additive system and resulting impurity level, a purity of better than 99.99 at% and a grain size of several micrometers. We are especially interested in the temperature dependence of yield stress, ultimate tensile strength, strain to fracture and fracture morphology of the microcrystalline Cu samples and possible effects caused by impurities stemming from the electrodeposition process. The Cu films are structured into tension samples using a photolithographic route as described in [9] and mechanical testing is performed at temperatures ranging from 293 K to 673 K. The microstructure of the Cu samples is characterized by electron backscatter diffraction in a scanning electron microscope (EBSD/SEM). Chemical analysis is performed by X-ray fluorescence spectroscopy (XRF), time-of-flight secondary ion mass spectroscopy (TOF-SIMS) and Auger electron spectroscopy (AES). Atomistic simulations are performed to understand possible detrimental influence of additives on the mechanical properties.

2 Experimental details

2.1 Film deposition

The Cu samples were produced by a photolithographic process and electrolytic deposition from liquid solution, for details see [9, 10]. Deposition was performed at room temperature (293 K) with an average current density of 300 A/m^2 and a voltage of ≈ 2 V. The electrolytes are sulfuric acid based with diluted $CuSO_4$. Two different additive systems in the electrolyte were used for Cu deposition with the aim to modify the grain size (samples A, B; see Fig. 1). Samples A possess a median grain size of 2.7 ± 0.6 µm and samples B of 10.1 ± 2.6 µm. All grain sizes were measured using the line intercept method for at least 50 grains. Since for the samples B the grains

frequently extend over the complete sample width the grain sizes were only measured along the sample length.

2.2 Heat treatment

All Cu samples were annealed at 673 K for 30 minutes after electrolytic deposition. Some of the samples with a small grain size of 2.7 ± 0.6 µm (samples A) were additionally annealed at 1073 K under vacuum (pressure < 10^{-5} mbar) for 5 h to reach a grain size which is comparable to samples B. In that case a median grain size of 15 ± 5 µm was measured using the line intersection method in EBSD/SEM images (Fig. 1).

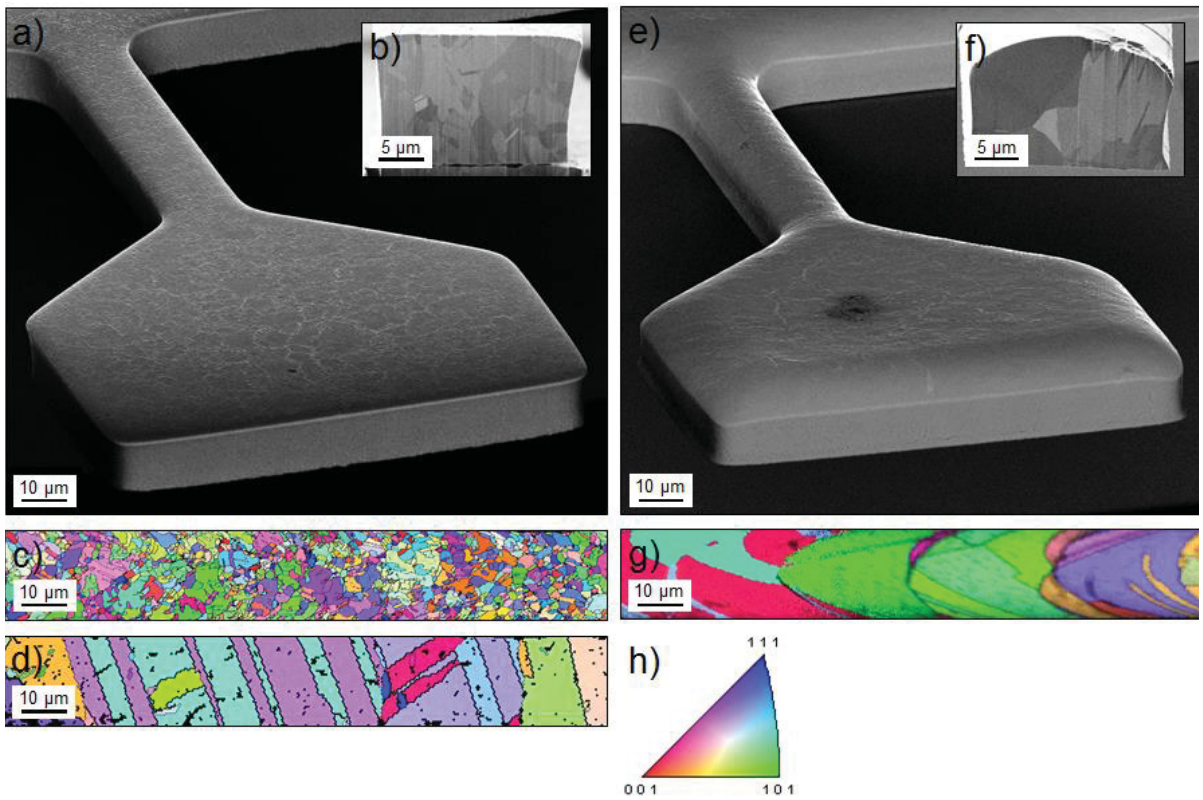

Fig. 1. EBSD/SEM images of the surface and cross-section of the tensile samples. (a, b, c) Sample type A, (d) sample type A annealed at 1073 K for 5 h, (e, f, g) sample type B and (h) color code of the inverse pole figure corresponding to the grain orientations. Note, that the distortion of Fig. 1g is caused by a curved surface.

2.3 Mechanical testing

For micromechanical testing a micro tensile module of Kammrath & Weiss [11], which was modified to operate at elevated temperatures up to 673 K [9], was used. All experiments were performed *in situ* using a SEM (LEO 440). Experiments were performed at 293 ± 2 K, 473 ± 4 K and 673 ± 4 K; at each temperature at least three samples were tested. The temperature was measured with a thermocouple in a distance of 3 mm to the tensile samples, leading in a finite element simulation to a 15 K lower temperature in the tensile samples than in the thermocouple at 673 K. The individual sample dimensions (ca. 20 • 20 • 130 μm^3) were determined using SEM (Zeiss Leo 1525) images for each sample before tensile testing for calculation of the stress-strain curve from the obtained force and elongation. Note, that the deviation from a rectangular shape was considered for cross-section calculation. Force measurement was performed with an accuracy of 10 µN by eigenfrequency measurements of a tungsten wire [12]. Elongation was recorded with an optical grid and verified by digital image correlation (DIC). The loading speed was 0.1 µm/s corresponding to a strain rate of approximately 10^{-3} s^{-1}.

2.4 Chemical characterization

The overall chemical composition of the 20 µm thick Cu films on silicon was measured with XRF (PANalytical Axios) and time-of-flight mass-spectroscopy (TOF-SIMS IV, IONTOF, analysis-source: 25 keV Bi^+, sputter-source O_2^+/Cs^+, lateral resolution < 300 nm, detection limit ≈ 10^{17} atoms/cm³ (≈ 1 at.ppm) for S and Cl). The chemical composition of the thin film surface was measured by AES (PHI 700 Scanning Auger Nanoprobe, hot field-emitter, cylindric mirror-analysator, Ar floodgun).

2.5 Atomistic simulations

Atomistic simulations were performed to assist the interpretation of the experimental results concerning detected impurities at surfaces and grain boundaries. The MedeA® computional environment of Materials Design Inc. [13] was used to conduct the simulations. The simulations were based on density functional theory (DFT) [14, 15]

within the generalized gradient approximation (GGA) as parameterized by Perdew, Burke, and Ernzerhof [16]. The density-functional or Kohn-Sham equations were solved with projector-augmented-wave (PAW) potentials and wave functions [17] as implemented in the Vienna ab initio Simulation Package (VASP) version 5.2 [18 - 21]. Information about the crystal structures and the atomic number/nuclear masses were used as input parameters. However, all structures were fully relaxed. Total energies were calculated for all relaxed structures in order to assess the thermo-dynamical stability and mechanical properties (e.g. work of separation). For the calculations of the ∑5 (001) and ∑7 (111) twisted grain boundaries unit cells with 240 and 336 atoms containing one or two impurity atoms were used.

3 Results and Interpretation

3.1 Mechanical properties

Tensile testing of the two sample types (A, B) reveals significant differences. The fine-grained samples of type A exhibit with 142 ± 5 MPa a higher yield stress at 0.2 % plastic strain than the large-grained samples B with 64 ± 10 MPa. The ultimate tensile strength (UTS) decreases from 254 ± 6 MPa (samples A) to 181 ± 31 MPa (samples B) as a consequence of the larger grain size, while the elongation to fracture remains unaltered at ca. 40 %. This finding has been explained earlier [22] based on the different median grain sizes (Hall–Petch effect [23, 24]). In contrast to that, a different behavior is observed when performing the micro-tensile tests at 473 K and 673 K and comparing the results for the two sample types (Fig. 2). The fine-grained material (samples A) reveals a pronounced decrease in elongation to fracture to values of approximately 20 % at 473 K and 10 % at 673 K, while samples B remain at a high elongation to fracture of typically about 30 %. Between 473 K and 673 K there is a further decrease in UTS from 153 to 104 MPa for samples A and from 129 to 77 MPa for samples B. The relatively large scattering in elongation to failure of the coarse microstructure is caused by the fact that only a few grains are contained in the micro-tensile sample and the weakest grain will determine with its orientation and size the mechanical response as seen by *in situ* and *post mortem* SEM observations. This behavior is independent of temperature (Fig. 3).

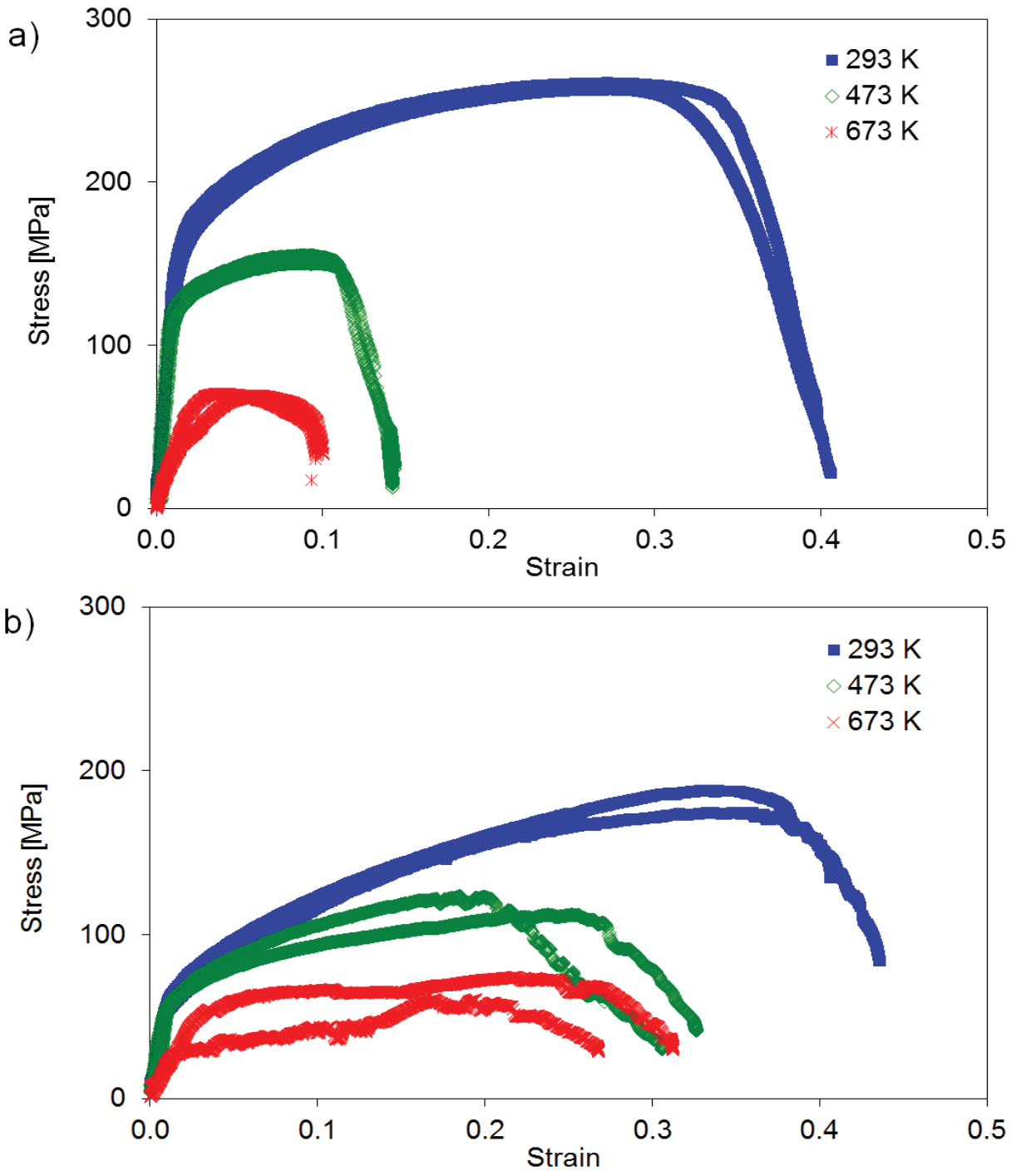

Fig. 2. Stress-strain curve of samples A and B at 293 K, 473 K and 673 K. Note that at 473 K the yield strength, UTS and elongation to fracture are drastically reduced for the (a) fine-grained samples A while for (b) samples B with their bamboo-like microstructure only the UTS shows a significant decrease with increasing temperature. Both samples A and B show at 673 K a significant smaller slope during loading (apparent Young's modulus) caused by plastic deformation (settlement) of the sample head.

3.2 Fracture appearance

The coarse-structured samples B show a ductile behavior with intragranular fracture accompanied by formation of glide steps on the surface at 293 K. The glide steps range across the whole sample cross-section (Fig. 3a) as a consequence of the relatively large grain size. The fracture morphology remains unaltered for the investigated temperature regime and occurs always by necking and fracture within a single grain due to dislocation plasticity (see Figs. 3b, c).

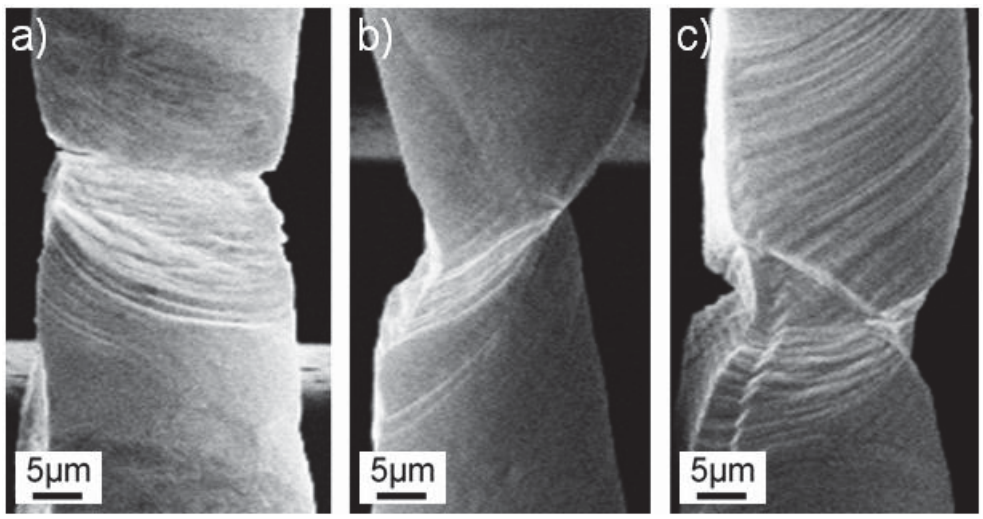

Fig. 3. Deformation behavior of bamboo-structured samples B at (a) 293 K, (b) 473 K, and (c) 673 K.

At 293 K samples A, which contain typically > 50 grains per cross-sectional area, show strong plastic deformation and necking (Fig. 4a) with numerous grains involved. At 473 K the fracture behavior changes; now preferential cracking along the grain boundaries occurs indicating that grain boundary embrittlement took place. While there is still some remaining plasticity visible on the fracture surface at 473 K (Fig. 4b), the overall fracture behavior appears to be brittle at 673 K (Fig. 4c, d).

EBSD/SEM studies were performed before and after micromechanical testing to identify the misorientation angle of grain boundaries along the fracture path at the sample surface. The grain boundaries which are prone to fracture at elevated temperatures are general large angle grain boundaries (Fig. 5). No $\sum 3$ and $\sum 9$ grain boundaries were observed to participate in intergranular fracture.

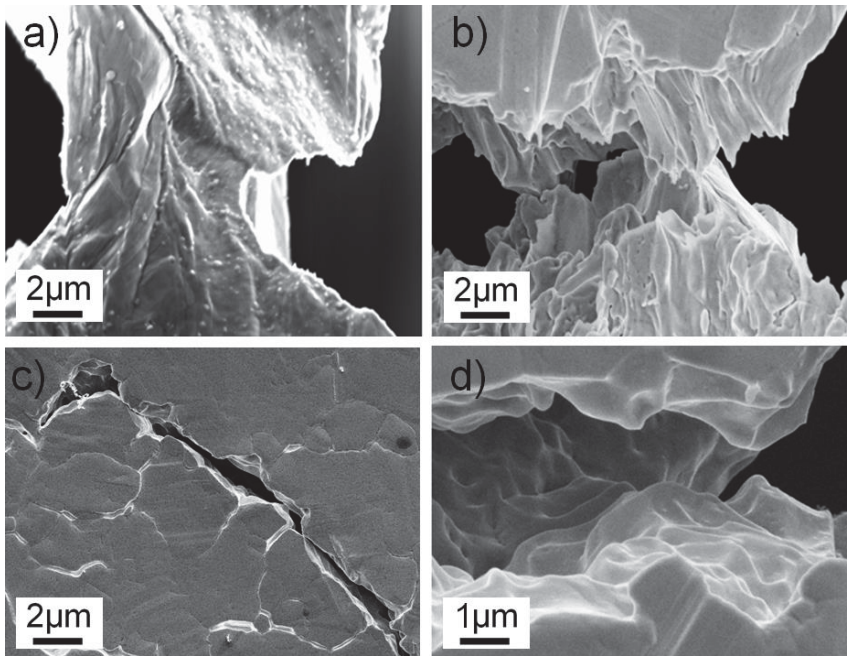

Fig. 4. Deformation behavior of samples A with a grain size of 2.7 µm at (a) 293 K, (b) 473 K, (c) and (d) 673 K.

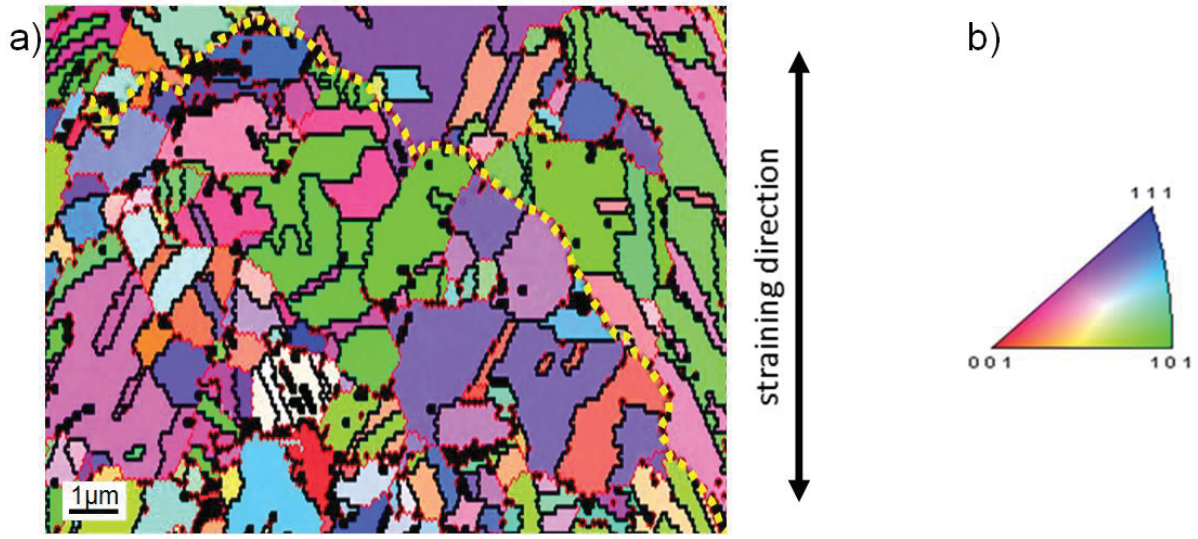

Fig. 5. (a) EBSD/SEM image of the tensile sample showing the grain orientation in tensile direction. Grain boundaries (red), Σ3 twin boundaries and Σ9 grain boundaries (black) and the crack path (yellow dotted line) are marked. (b) The color code of the inverse pole figure provides the orientation in tensile direction. For the corresponding SEM image see Fig. 4c.

3.3 Chemical analysis

Global chemical composition

The purity of all Cu samples was 99.99 at% or higher. Despite this high purity, up to 50 ppm of impurities (especially S and Cl) were detected. However this is the detection limit of XRF. This is in agreement with qualitative TOF-SIMS depth profile measurements over an area of 20 • 20 μm^2 revealing a higher S and Cl level for samples A compared to samples B (Fig. 6a and b). Both the XRF and TOF-SIMS measurements have detected an O signal in a similar range as for S or Cl. The higher signal near the surface originates from a slight surface oxidation. Under the assumption, that all impurities segregate to the grain boundaries this would result in a grain boundary allocation in the 2.7 µm grained material of 3.8 atoms each of S and Cl per nm^2.

Local chemical composition

AES measurements of the as-deposited samples A and B (i.e. prior to any heat treatment), both with a grain size of 2-3 µm, show no Cl on the surface. After a heat treatment at 673 K for 30 min both types of samples have a Cl surface content of 0.3 at%, indicating Cl segregation during annealing. There is no grain growth in samples A, however samples B show significant grain growth to ≈ 10.1 µm. TOF-SIMS maps of samples A over an area of 72 • 72 μm^2 reveal segregation of non-metallic elements such as O (Fig. 6c), Cl (Fig. 6d) and S (Fig. 6e) to grain boundaries.

Furthermore tips of the grain boundary region have been prepared for atom probe tomography (APT) to study the local chemical composition. However, all APT analysis of grain boundaries in sample type A failed due to the different evaporation fields of the matrix and the grain boundary. This led to errors in peak detection and three-dimensional atomic reconstructions preventing a meaningful interpretation.

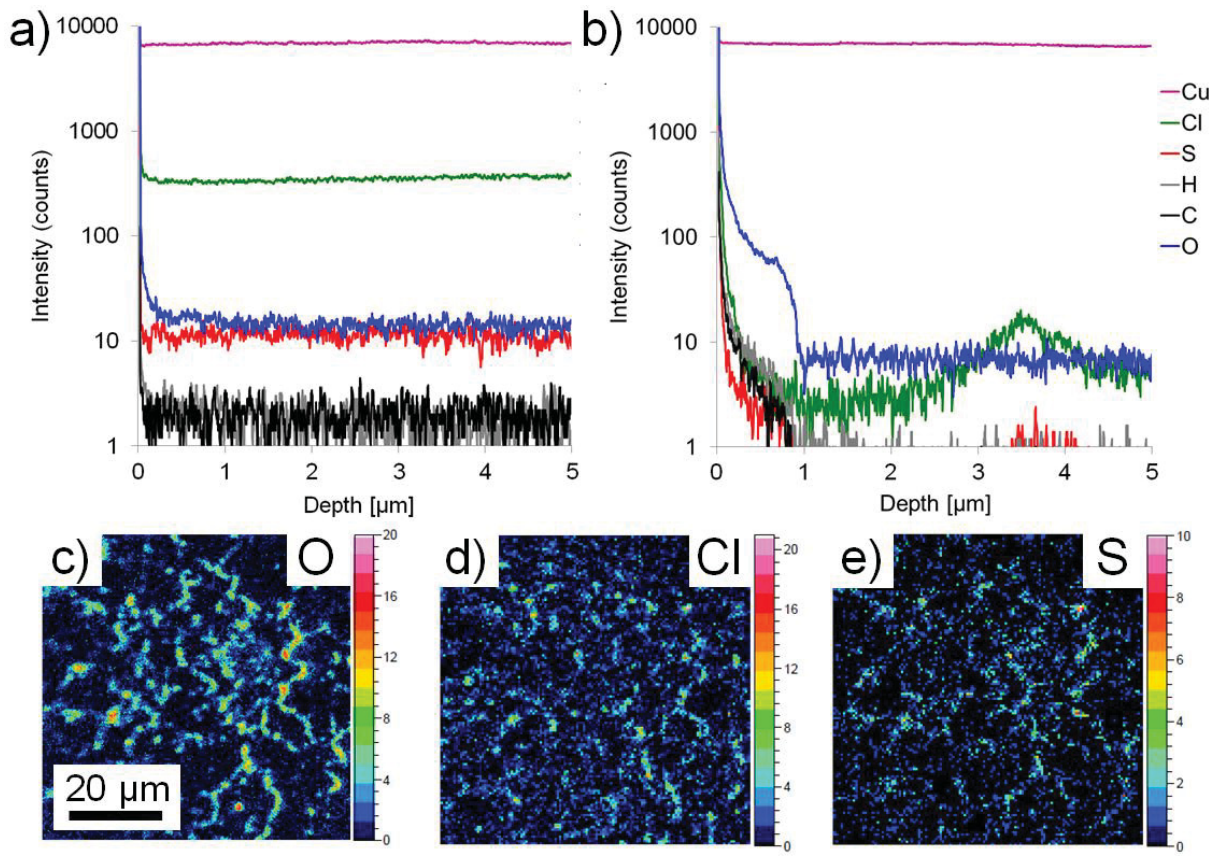

Fig. 6. TOF-SIMS analysis of the materials. Depth profiles of samples (a) A and (b) B show a significantly higher S and Cl content for sample type A. (c) O, (d) Cl and (e) S distribution maps of sample type A recorded at a depth of ≈ 50 nm. The maps (c-e) indicate a significant enrichment of O, S and Cl on grain boundaries. The O content is independent from the electrolyte system. Note, that in TOF-SIMS analysis a quantitative comparison between different elements is not possible due to element dependent signal yield.

3.4 Atomistic simulations

Our atomistic DFT simulations showed, that both Cl and S have a strong tendency to segregate from bulk Cu to grain boundaries and especially to the free surface, which is also well known from literature [10, 25]. A measure for the segregation tendency is the energy release ΔE_{seg} during segregation. Hence, in the case of a negative ΔE_{seg} there is a thermodynamic driving force for segregation. The calculations performed for ∑5 (001) and ∑7 (111) grain boundaries and the corresponding surfaces, i.e. (001) and (111) reveal a similar tendency towards segregation to the grain boundary for Cl and S. However, Cl has a much higher tendency to segregate to the free (001) and (111) surfaces than S (Tab. 1). In all cases ΔE_{seg} is lower for surface segregation than for grain boundary segregation.

Tab. 1. Calculated energy release during segregation ΔE_{seg} of Cl and S in Cu

	ΔE_{seg} [kJ/mol]	
	Cl	S
GB segregation, ∑5 (001)	-69.9	-54.3
surface segregation, (001)	-321.5	-145.3
GB segregation, ∑7 (111)	-53.5	-56.3
surface segregation, (111)	-272.0	-129.9

A measure for the weakening of the grain boundary is the work of separation E_{sep}. In the case of a low E_{sep} the grain boundary is weak. If impurities are inserted at the ∑5 and ∑7 twist grain boundaries, Cl reduces the work of separation more significantly than S (Tab. 2). The kinetics of S and Cl diffusion will be discussed later. Note that these results are based on an impurity concentration of 0.77 atoms/nm^2 for the ∑5 (001) and 0.62 atoms/nm^2 for the ∑7 (111) grain boundary.

Tab. 2. Calculated work of separation E_{sep} of ∑5 and ∑7 grain boundaries of pure Cu and Cu contaminated with Cl and S with planar impurity concentration c_{imp} in atoms per nm^2.

	c_{imp} [1/nm^2]	E_{sep} [J/m^2]		
		Pure Cu	Cl	S
∑5 (001)	0.77	1.08	0.82	1.01
∑7 (111)	0.62	1.13	0.89	1.04

4 Discussion

The discussion is divided into 4 sections. The first part focusses on the necessity to use additives for electrodeposition of Cu conductor lines/films. We also show that grain boundary sliding can be excluded as a course for the low ductility of the fine-grained samples at elevated temperatures. Furthermore, the detected non-metallic elements and their influence on grain boundary embrittlement is critically discussed. Finally, strategies to avoid grain boundary embrittlement for electrodeposited Cu are discussed.

Former studies on Cu micron samples [1, 26 - 28] show, that the mechanical properties at ambient temperature are improving with decreasing grain size. These

experimental observations are supported by simulations [29]. The fatigue lifetime at ambient temperature also increases with decreasing grain size [22, 30 - 33]. Consequently all applications which need Cu films or structures of high strength aim for small grain sizes.

To grow metal films with a small grain size by electrodeposition it is necessary to have additives in the electrolyte system. These additives are incorporated in the deposited Cu films especially at the beginning of the Cu deposition and cause a small impurity level (< 100 ppm) in the metal thin film [34, 35]. During annealing, which is usually done after deposition to stabilize the microstructure and to remove point defects, the additives decompose and their constituents segregate to interfaces like grain boundaries due to the low solubility of non-metallic elements such as S and Cl in Cu. E. g. for the system Cu-S the equilibrium solubility of S is 4 at.ppm (2 wt.ppm) at 900 K [36, 37]. For non-equilibrium conditions this solubility limit can be significantly exceeded leading to super-saturation. The resulting grain boundary segregation reduces grain growth by pinning the grain boundaries [22, 38 - 43] and by reducing the driving force for grain coarsening due to the reduction of the grain boundary energy [44, 45]. Even without an annealing process after deposition, molecular impurities decompose into atomic impurities accompanied by grain growth until metastable equilibrium conditions are approached. This effect is termed self-annealing and is caused by a high level of stored defect and interface energy, the latter being reduced by grain growth due to a reduction in grain boundary area [46, 47]. Furthermore, it has been shown that impurities at the grain boundaries can reduce electromigration, which in turn increases the lifetime of microelectronic devices [48]. The reason for the reduction of electromigration is a reduction of Cu self-diffusion along the grain boundary caused by Cu-S bonds [49].

However, the current micro-mechanical experiments performed at elevated temperatures reveal an embrittlement of Cu micron-samples deposited from an electrolyte system leading to a grain size of 2.7 µm (samples A) (Fig. 2).

While for nanocrystalline materials it is well known that grain boundary sliding can increase the ductility and elongation to fracture [50], for commercial-grained materials the opposite trend has been observed if grain boundary sliding starts before plastic deformation. Subsequently, to exclude grain boundary sliding as the

reason for the brittle behavior at elevated temperatures, the relaxation time, τ, for grain boundary sliding as a function of grain size and impurity level was calculated:

$$\tau = \frac{kTb^2d}{4\mu\Omega\delta D_{0,gb}} e^{\frac{Q_{gb}}{RT}} \text{ [51]}, \qquad (1)$$

whereby k = 1.38 • 10^{-23} J/K is the Boltzmann's constant, T [K] the temperature, μ = 42.1 GPa the shear modulus (at T = 300 K), Ω = 1.18 • 10^{-29} m³ the atomic volume, b = 2.56 • 10^{-10} m the Burgers vector, d [m] the grain size, $\delta D_{o,gb}$ the grain boundary diffusion pre-exponent ($\delta D_{o,gb}$ = 5 • 10^{-15} m³/s for the pure interface, 5 • 10^{-13} m³/s for the Cl decorated interface and 2 • 10^{-15} m³/s for the S decorated interface), Q_{gb} = 1.04 • 10^5 J/mol the grain boundary diffusion activation energy and R = 8.314 J K^{-1} mol^{-1} the universal gas constant [50, 52 - 55] (Fig. 7). The calculations show that both, samples A and B, could be prone to grain boundary sliding. The effect would be enhanced with Cl on the grain boundaries due to a reduction of relaxation time.

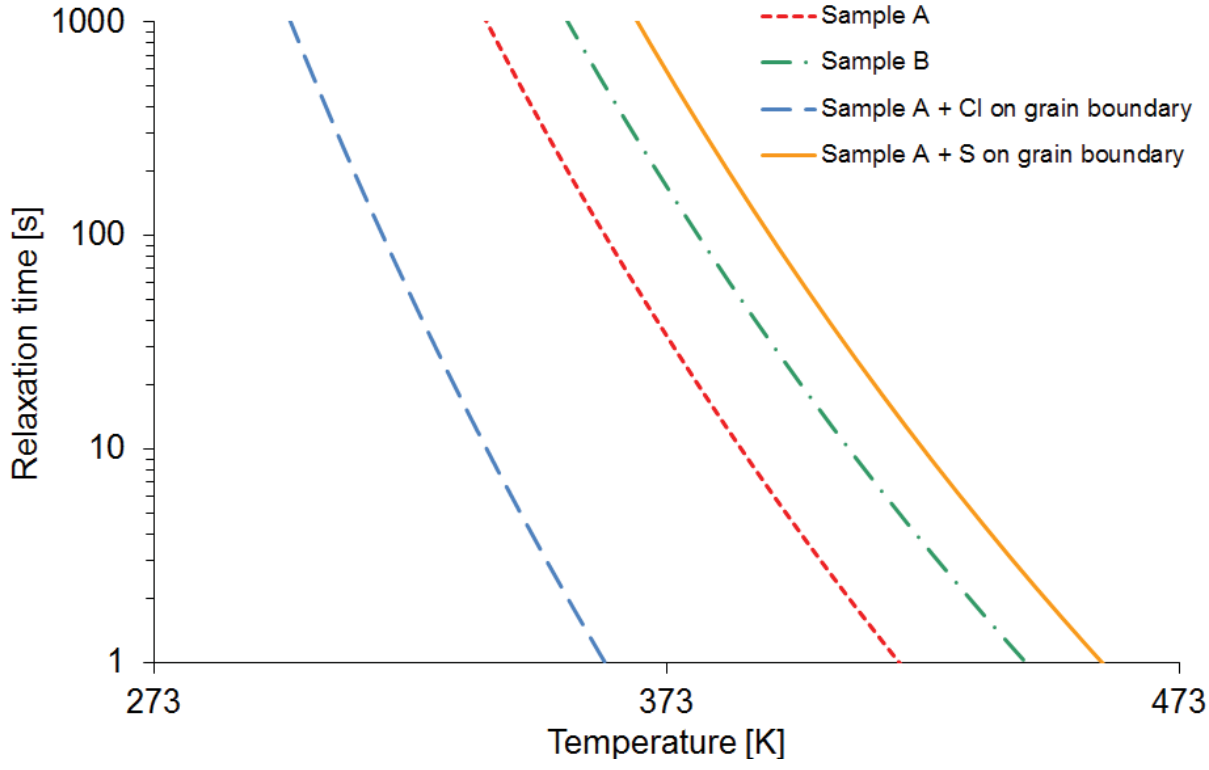

Fig. 7. Relaxation time τ for grain boundary sliding for Cu samples with different grain sizes and impurity levels [50, 52 - 55].

Thus, we believe that grain boundary sliding is not the reason for the brittle appearance of samples A at elevated temperatures, otherwise samples B should also show an intergranular fracture at 473 and 673 K. Since this has not been observed, other mechanisms must be the reason for the embrittlement.

In lateral TOF-SIMS maps on samples A the elements Cl, O and S have been identified and indicate grain boundary segregation (Fig. 6c, d and e). Indeed an embrittlement of Cu caused by O is well known [56]. We believe that O embrittlement can be excluded in our study as both types of samples A and B have a comparable O content (Fig. 6a and b). DFT calculations reveal that Cl on the grain boundary reduces the work of separation more significantly than S, which is in accordance with the low melting points of CuCl (703 K) and $CuCl_2$ (893 K) [57] compared to Cu_2S (1403 K) [58]. For the system Cu-Cl between 293 K and 673 K only at 648 K a phase transition occurs, which could cause grain boundary fracture. However, embrittlement was found at a much lower temperature and the formation of Cu-Cl phases on surfaces was not reported up to now [59].

For the system Cu-S there are several phase transitions [37, 60]. Below a S content of 100 ppm the formation of the Cu rich Cu_2S (chalcocite) is fostered and was reported in early studies on bulk Cu [61], but also found in more recent XPS studies of Cu thin films [35]. Crystallographic properties of Cu_2S can be found in Tab. 3.

Tab. 3. Crystallographic properties of Cu_2S [62, 63]

Phase	at% S	Structure	*a* [nm]	*b* [nm]	*c* [nm]
α-Cu_2S (α-chalcocite)	≈ 33.3	monoclinic	1.52	1.19 (β = 116.35°)	1.35
β-Cu_2S (β-chalcocite)	≈ 33.3	hexagonal	0.40		0.68

In bulk Cu_2S there is a reversible, polymorphic phase transformation of Cu_2S at 376 K from monoclinic α-Cu_2S (low temperature phase) to hexagonal β-Cu_2S (high temperature phase) [37, 64]. In Cu_2S nanorods this transformation has been found at 337 ± 4 K [65], indicating a size dependence of the transformation temperature.
One possible explanation for the embrittlement of the grain boundary through the phase transformation of Cu_2S at elevated temperatures is that the formation enthalpy $\Delta_f H$ of β-Cu_2S is smaller (more negative) than that of α-Cu_2S, resulting in a more ionic bond with higher brittleness for β-Cu_2S bonds. Another explanation is an

increase in specific volume ΔV during phase transformation causing cracks. For bulk Cu S induced embrittlement has been reported in literature [66]. The critical S level for embrittlement has been found to depend on the grain size [66]. Embrittlement of macro sized Cu samples with 10 ppm S at temperatures above 453 K was observed, caused by segregation of S to grain boundaries and up to 13 at% S were found by AES on the base of the cavities of the fracture surfaces [67]. It is well known that S causes embrittlement; the role of a possible Cl embrittlement is not yet fully understood and would demand in future for dedicated experiments with only Cl as an impurity element.

For practical applications it is required to solve the problem of embrittlement in small-grained electrodeposited Cu. To foster segregation from the bulk material via the grain boundary to the free surface an additional heat treatment at 1073 K (5 h) was performed. Through this additional heat treatment at 1073 K of samples A grain growth was achieved with a final average grain size of 15 ± 5 µm, which is comparable to the grain size of 10.1 ± 2.6 µm of samples B. Mechanical testing of the 1073 K annealed samples A show no embrittlement but nearly the same stress-strain curves as samples B independent of the temperature. This indicates that source segregation to the surface has reduced the allocation of non-metallic elements at the grain boundaries, which in turn led to grain growth. This is also supported by calculation of the diffusion kinetics of S at 1073 K [68] which indicate that for a diffusion distance of 10 µm only 130 s are required, which is in accordance with AES measurements, showing significant diffusion of S between 575 and 875 K to the free surface [25]. Estimates of Cl diffusion in Cu [69] reveal even shorter diffusion times below 1 ms for a diffusion distance of 10 µm at 1073 K.

For bulk Cu it has been shown that embrittlement at elevated temperatures can be reduced by an addition of small amounts of Ti, Zr and V before casting [70]. Furthermore small additions of B, Nb, Fe and Ag could reduce grain boundary embrittlement significantly [71, 72], subsequently this could also prevent the embrittlement of electrodeposited Cu, however influences on the electrical conductivity have to be considered for practical applications.

5 Summary and conclusions

Micro-tensile experiments at electrodeposited Cu at ambient and elevated temperatures have shown an embrittlement of Cu grain boundaries which leads to a significant reduction in strain to failure from 40 % at 293 K to 20 % at 473 K. Cracks are initiated at the grain boundaries before substantial plastic deformation in the grains starts. Segregation of the non-metallic elements S and Cl to the grain boundaries after a 30 min annealing (673 K) and finally to the free surfaces after 5 h annealing (1073 K) has been observed. Segregation of Cl to the free surface has been revealed by AES and atomistic simulations.

Through a heat treatment it was possible, to foster grain growth and remove Cl and S from the grain boundaries. Cl and S segregate to the free surfaces unpinning the grain boundaries, which leads to grain growth resulting in a bamboo-like microstructure. As a consequence, the Cu becomes devoid of grain boundary embrittlement even at 673 K.

While in other studies on Cu thin films it has been pointed out that impurities such as S have a positive effect on improving electromigration resistance [35, 49, 73], this study shows that impurities deteriorate the mechanical properties of Cu thin films at elevated temperatures.

Acknowledgement

Part of this work was jointly funded by the Austrian Research Promotion Agency (FFG, Project No. 831163) and the Carinthian Economic Promotion Fund (KWF, contract KWF-1521|22741|34186). The authors want gratefully acknowledge fruitful discussions with A. Mavromaras, M. Herbig and P.-P. Choi, furthermore the authors want to thank J. Fugger. Thanks for technical assistance is expressed to A. Leitner, M. Augustin, H. Felber, R. Grilz, H. Groß, F. Hubner, M. Krug, R. Leuschner, C. Lindner, K. Matoy, S. Modritsch, T. Ostermann, G. Reiter, H. Schönherr and K. Schrettlinger. A. Wimmer gratefully acknowledges the Erich Schmid Institute of Materials Science in Leoben, where the mechanical testing and SEM studies were performed.

References

1 WD Nix, Metall. Trans. A 20, 11, (1989), 2217-2245.

2 JC Bravman, WD Nix, DM Barnett, DA Smith, Mater. Res. Soc. Symp. Proc. 130, Pittsburgh, PA, (1996), 129.

3 G Dehm, Prog. Mat. Sci. 54, 6, (2009), 664-688.

4 WD Nix, Mat. Sci. Eng. A 234–236, (1997), 37-44.

5 R Saha, WD Nix, Acta Mater. 50, 1, (2002), 23-38.

6 MD Uchic, DM Dimiduk, Mat. Sci. Eng. A 400–401, (2005), 268-278.

7 D Kiener, W Grosinger, G Dehm, R Pippan, Acta Mater. 56, 3, (2008), 580-592.

8 C Motz, T Schöberl, R Pippan, Acta Mater. 53, 15, (2005), 4269–4279.

9 M Smolka, C Motz, T Detzel, W Robl, T Griesser, A Wimmer, G Dehm, Rev. Sci. Instrum. 83, (2012), 064702.

10 M Stangl, PhD thesis, TU Dresden, (2007), 27-31.

11 B Yang, C Motz, W Grosinger, W Kammrath, G Dehm, Int. J. Mater. Res. 99, (2008), 716-724.

12 B Yang, C Motz, W Grosinger, G Dehm, Mat. Sci. Eng. A 515, (2009) 71-78.

13 MedeA 2.6, Materials Design, Inc., Angel Fire, NM, USA (2011).

14 P Hohenberg, W Kohn, Phys. Rev. 136, 3B, (1964), B864-B871.

15 W Kohn, LJ Sham, Phys. Rev. 140, (1965), A1133-A1138.

16 JP Perdew, K Burke, M Ernzerhof, Phys. Rev. Lett. 77, (1996), 3865-3868.

17 PE Blöchl, Phys. Rev. B 50, (1994), 17953.

18 G Kresse, J Hafner, Phys. Rev. B 47, (1993), 558-561.

19 G Kresse, J Furthmüller, Phys. Rev. B 54, (1996), 11169-11186.

20 G Kresse, J Furthmüller, Comp. Mat. Sci. 6, (1996), 15-50.

21 G Kresse, D Joubert, Phys. Rev. B 59, (1999), 1758-1775.

22 A Wimmer, A Leitner, T Detzel, W Robl, W Heinz, R Pippan, G Dehm, Acta Mater. 67, (2014), 297-307.

23 EO Hall, Proc. Roy. Soc. B 64, (1951), 747-753.

24 NJ Petch, J. Iron Steel 174, (1953), 25-28.

25 IN Sergeev, VK Kumykov, VA Sozaev, MA Shebzukhova, Bulletin of the Russian Academy of Sciences: Physics 72, 10, (2008), 1388-1390.

26 GW Nieman, JR Weertman, RW Siegel, Scripta Met. 23, 12, (1989), 2013-2018.

27 XZ Liao, YH Zhao, YT Zhu, RZ Valiev, DV Gunderov, J. Appl. Phys. 96, 1, (2004), 636-640.

28 B Yang, C Motz, M Rester, G Dehm, Phil. Mag. 92, 25-27, (2012), 3243-3256.

29 C de Sansal, B Devincre, L Kubin, Key Eng. Mat. 423, (2009), 25-32.

30 DT Read, Int. J. Fat. 20, 3, (1998), 203-209.

31 S Hong, R Weil, Thin Solid Films, 283, 1-2, (1996), 175-181.

32 N Murata, K Tamakawa, K Suzuki, H Miura, Int. Conf. on Electr. Mat. and Packaging, (2008), EMAP 2008.

33 R Hofbeck, K Hausmann, B Ilschner, HU Kunzi, Scripta Metall. 20, 11, (1986), 1601-1605.

34 M Stangl, J Acker, S Oswald, M Uhlemann, T Gemming, S Baunack, K Wetzig, Microel. Eng. 84, (2007), 54-59.

35 S Strehle, R Reiche, V Hoffmann, J Acker, T Gemming, K Wetzig, Microchim. Acta 156, (2007), 167-172.

36 PA Korzhavyi, IA Abrikosov, B Johansson, Acta Mater. 47, 5, (1999), 1417-1424.

37 J Oudar, C. R. Acad. Sci. 249, (1959), 259.

38 JS Smart Jr., The effects of impurities in copper, Rheinhold Publishing Corp., NY, Ch 19, (1954), 4102.

39 WH Bowyer, RL Crocker, A study of Attenuation and scattering of ultrasound in polycrystalline copper, SKI report 96:27.

40 M Stangl, PhD thesis, TU Dresden, (2007), 8-12.

41 HD Merchant, WC Liu, LA Giannuzzi, JG Morris, Mat. Char. 53, (2004), 335-360.

42 J Neuner, I Zienert, A Peeva, A Preuße, P Kücher, JW Bartha, Microel. Eng. 87, (2010), 254-257.

43 VA Vas'ko, I Tabakovic, SC Riemer, MT Kief, Microel. Eng. 75, (2004), 71–77.

44 R Kirchheim, Acta Mater. 50, (2002), 413-419.

45 T Chookajorn, HA Murdoch, CA Schuh, Science 337, (2012), 951-954.

46 MS Yoon, YJ Park, YC Joo, Thin Solid Films 408, (2002), 230-235.

47 R Huang, W Robl, H Ceric, T Detzel, G Dehm, IEEE Transactions on Device and Materials Reliability 10, 1, (2010), 47-54.

48 E Glickman, M Molotskii, Materials Lett. 26, (1996), 65-68.

49 T Surholt, C Herzig, Acta mater. 45, 9, (1997), 3817-3823.

50 IA Ovid'ko, AG Sheinerman, Acta Mater. 57, (2009), 2217-2228.

51 MF Ashby, R Raj, RC Gifkins, Scr. Metall Mater. 4, (1970), 737-742.

52 GD Sim, JH Park, MD Uchic, PA Shade, SB Lee, JJ Vlassak, Acta Mater. 61, (2013), 7500-7510.

53 WK Walter, DE Manolopoulos, RG Jones, Surf. Sci. 348, (1996), 115-132.

54 HG Bohn, M Prieler, CM Su, H Trinkaus, W Schilling, J. Phys. Chem. Solids 55, (1994), 1157-1164.

55 R Raj, MF Ashby, Metall. Trans. 2, (1971), 1113-1127.

56 TG Nieh, WD Nix, Met. Trans A 12A, (1981), 893-901.

57 G Brauer, Handbuch der Präparativen Anorganischen Chemie, 2. Band, Ferdinand Enke Verlag, Stuttgart, (1978), 972-977.

58 NN Greenwood, A Earnshaw, Chemistry of the Elements, Oxford, Pergamon Press, (1984), 1373.

59 K Motai, T Hashizume, H Lu, D Jeon, T Sakurai, Appl. Surf. Sci. 67, (1993), 246-251.

60 Landolt-Börnstein, New Series IV/19B.

61 MJ Saarivirta, Trans ASM 57, (1964), 133-141.

62 HT Evans jr., Nat. Phys. Sci. 232, (1971), 69-70.

63 BJ Wuensch, MJ Buerger, Miner. Soc. Am. Spec. Paper 1, (1963) 164.

64 W Biltz, W Fischer, Z. Anorg. Allg. Chem. 166, (1927), 290-298.

65 H Zheng, JB Rivest, TA Miller, B Sadtler, A Lindenberg, MF Toney, LW Wang, C Kisielowski, AP Alivisatos, Science 333, (2011), 206-209.

66 PJ Henderson, Low temperature creep of copper intended for nuclear waste containers, SKB technical report 92-04.

67 PJ Henderson, R Sandström, Mat. Sci. Eng. A, 246, (1998), 143-150.

68 W Sesselmann, TJ Chuang, Surf. Sci. 176, (1986), 67-90.

69 F Moya, GE Moya-Gontier, F Cabane-Brouty, physica status solidi (b), 35, 2, (1969), 893-901.

70 H Suzuki, Trans Japan IoM 26, 1, (1985), 69-77.

71 NQ Vo, J Schäfer, RS Averback, K Albe, Y Ashkenazy, P Bellon, Scripta Mater. 65, (2011), 660-663.

72 S Özerinç, K Tai, NQ Vo, P Bellon, RS Averback, WP King, Scripta Mater. 67, (2012), 720-723.

73 A Zehe, Microel. Reliab. 42, (2002), 1849-1855.

Paper B

Damage evolution during cyclic tension-tension loading of micron-sized Cu lines

A. Wimmer [a,*], A. Leitner [b], T. Detzel [c], W. Robl [d], W. Heinz [a], R. Pippan [b], G. Dehm [e,f]

a Kompetenzzentrum Automobil- und Industrie-Elektronik GmbH, A-9524 Villach, Austria
b Erich Schmid Institute of Materials Science, Austrian Academy of Sciences, A-8700 Leoben, Austria
c Infineon Technologies Austria AG, A-9500 Villach, Austria
d Infineon Technologies Germany AG, D-93049 Regensburg, Germany
e Department Materials Physics, Montanuniversitaet Leoben, A-8700 Leoben, Austria
f Max-Planck-Institut für Eisenforschung GmbH, D-40237 Düsseldorf, Germany

Acta Materialia 67, (2014), 297–307

Abstract

In this study, the low cycle fatigue properties (1-15,000 cycles) of electrodeposited Cu, which is frequently used as metallization in the semiconductor industry, is analyzed with respect to its microstructure. Freestanding Cu tensile samples with a size of 20 • 20 • 130 μm^3 were fabricated by a lithographic process. The grain size of the samples was modified by using three different process conditions for electrochemical Cu deposition. All samples were subjected to cyclic tension-tension testing performed with a miniaturized stress-controlled stage *in situ* in a scanning electron microscope until failure occurred. The number of cycles sustained prior to failure depends on the accumulated creep strain and can be related to the failure strain in a tensile test. It will be shown, that the microstructure influences the number of cycles to failure and the failure mode.

1 Introduction

Cu in microelectronic devices, such as LED-submounts (light-emitting diode-submounts) and MEMS (micro-electro-mechanical systems), has to fulfill two important requirements. It must provide a low electrical resistance even at high current densities and simultaneously provide excellent thermal conductivity to transfer dissipated energy. Furthermore, the occurrence of thermal stresses due to the difference of the coefficient of thermal expansion (CTE) of Si and Cu require an optimization of the mechanical properties [1, 2]. This includes the mechanical fatigue behavior as in many cases more than 10^8 load cycles must be endured during the lifetime of semiconductor devices [3]. If the Cu line is damaged the electrical resistance increases leading to additional Joule heating, resulting in a local hot spot and subsequent failure of the device. Thus, compromises in the grain size must be made to fulfill opposing trends. To prevent electromigration and to provide excellent electrical conductivity a large grain size is favored [4, 5], while a fine grain size is best to achieve high mechanical strength and a low susceptibility to mechanical failure under cyclic loading [6]. Since as-grown electrodeposited Cu films undergo uncontrolled grain growth at room temperature [7] an annealing treatment is made after the film deposition with the intention to stabilize the microstructure at a specific grain size.

The strength of Cu films could also be increased by alloying. However, alloying reduces the electrical and thermal conductivity and as a consequence, the temperature of the metallization would increase leading to higher thermal stresses. The potential of alloying Cu to optimize the strength while maintaining sufficient electrical and thermal conductivity is limited. Alternatively, controlling the texture may open routes to tailor the mechanical performance of Cu due to its high elastic anisotropy while maintaining excellent electrical conductivity. Possible methods to influence the texture are ion bombardment as reported in [8] or abnormal grain growth where the competition of surface energy and strain energy permit the alteration of the texture from <111> to <100> with increasing film thickness [9]. Both methods of tailoring the texture are inconvenient for industrial device processing as abnormal grain growth is undesirable because of decreasing strength and ion bombardment is only applicable for films thinner than 5 µm. A simpler approach to improve the strength without negative effects on thermal and electrical conductivity is to control the grain size. It is well established that smaller grains lead to higher strength (Hall–Petch effect [10, 11]). Furthermore, recent publications have shown that the number of grains in a cross-section has a significant influence on the mechanical behavior [12-14]. For Cu samples with less than about 25 grains in a cross-sectional area the strength decreases significantly compared to the bulk material. The strength decreases because of the high percentage of surface intersecting grains, where dislocations can easily escape and thus do not contribute to hardening. Similar findings were made for Cu [12], Pt [13] and Ni [14]. This approach was taken in the present study where the median grain size, d, of the Cu lines (line width w) was varied between 2.7 µm (w : d = 7.5) and 13.5 µm (w : d = 1.5) by using different methods for electrochemical Cu deposition and analyzed with respect to their fatigue properties.

Up to now low cycle fatigue (LCF) experiments were performed for similar grain sizes on Cu films on a substrate [15], Cu-foils [16 - 18], micro-sized Cu wires [19, 20] and ultrafine-grained (ufg) bulk Cu [21]. Additionally, high cycle fatigue (HCF) experiments were performed for similar grain sizes on thin Cu films on a substrate [6, 22 - 24] and ufg bulk Cu [25 - 27]. In several of these publications the size effect of different sample dimensions with different grain sizes was analyzed. During fatigue testing transgranular extrusions and intergranular cracks are formed in large grains accompanied by surface roughening and damage formation [6, 22]. For thin films and

other small scale materials the fatigue lifetime significantly exceeds that of bulk material [23]. Increasing the loading frequency reduces the number of cycles to failure [24]. In the LCF regime the deformation behavior of ufg Cu in fatigue experiments is different to that of conventional bulk Cu. The static tensile strength of ufg Cu is 1.8 times higher than that of conventional bulk Cu, contrary to the high cycle fatigue properties that show no significant difference [25]. Up to 10^7 cycles ufg Cu shows a much higher strength compared to conventional bulk Cu, above 10^7 cycles grain coarsening starts resulting in a much lower strength in this area [26]. Contrary to this in other fatigue experiments of ufg material a change in microstructure was not found until > 10^9 cycles [27].

In this paper detailed investigations on the influence of grain size for free-standing micron-sized samples are reported. A further target of this work was to compare the cyclic tension-tension behavior ($R \approx 0$, $R = \sigma_{min} / \sigma_{max}$) with cyclic compression-tension experiments ($R = -1$) from bulk material. The main outcome is that with changing R values different deformation mechanism are expected. Furthermore, macroscopic samples with a microcrystalline grain structure usually possess more than 10^{10} grains in the sample volume, while for microscopic samples with microcrystalline grain structure the number of grains per volume typically ranges between a few and 10^3 grains.

Performing micromechanical experiments on small samples adds an additional complication to fatigue testing. It is challenging to accurately measure the strain between subsequent loading cycles for micromechanical experiments. In this study it will be shown that strain measurements can be performed accurately by performing *in situ* scanning electron microscope (SEM) fatigue experiments and the role of grain size and number of grains per sample volume will be analyzed.

2 Experimental details

2.1 Film deposition and microstructure analysis

The Cu samples were produced by photolithographic process and electrolytic deposition from liquid solution, for details see [28]. Three different electrolyte compositions were used for Cu deposition with the aim to modify the grain size. All Cu films were annealed at 400 °C for 30 min directly after deposition to stabilize the microstructure at specific grain sizes. The microstructure of all samples was characterized by scanning electron microscopy (SEM) and electron backscatter diffraction (EBSD). No surface treatment (e.g. electro-polishing) was needed to achieve high quality EBSD patterns.

Grain size distributions of the micro-tensile beams were measured using SEM-EBSD images. The individual grain sizes were determined along the sample length with the line intercept method using a total line length of 100 µm for each sample. The coarse-grained material utilized more than 60 grains in the measurement, leading to statistically significant median grain size values. A lateral measurement of the grain size width was not performed because sometime grains extend over the complete line width. Furthermore, some samples possessed a curved surface which would lead to projection artifacts if the grain size width would have been determined.

2.2 Mechanical testing

Tensile tests and low cycle fatigue experiments were performed *in situ* using a SEM (LEO 440) with a micro tensile module from Kammrath & Weiss [29]. The sample dimension for the static and cyclic tension-tension loading was nominally 20 • 20 µm^2 in cross-section and 130 µm in loading-axis excluding the sample head. The sample head was placed into a silicon gripper by moving the sample stage first horizontally and then vertically as described in detail in [28]. The samples were loaded to the maximum stress σ_{max} and then cyclically unloaded to the minimum stress σ_{min} = 20 ± 10 MPa with a frequency f = 0.05 ± 0.03 Hz. The maximum stress values for the cyclic experiments were chosen based on the ultimate tensile strength of the tensile test providing the upper limit (i.e. 291 MPa, see Tab. 1) and 110 ± 10 MPa as

a lower limit. The lower stress limit was selected such that the cyclic *in situ* experiment lasted less than 6 days, i.e. less than about 15,000 cycles.

Fig. 1 shows a typical LCF experiment with σ_{max} = 200 MPa, σ_{min} = 20 MPa (R = 0.1) and N = 1650. The scatter of the stress level by ± 10 MPa is mainly caused by the reaction time of the load controller and by stress drift induced by slight changes in temperature during the *in situ* experiment. All experiments were performed at 293 ± 2 K. The individual undeformed sample dimensions (height and width) were measured in a SEM (Zeiss 1525) in order to calculate the engineering stresses during straining. The curvature of the surfaces of fine-grained sample B and coarse-grained sample D, which was measured by SEM in a FIB cross-section, was considered for cross-section calculation.

The maximum accepted misalignment between sample and gripper was < 1 °. During cycling SEM images were taken for digital image correlation (DIC) at σ_{max} with a recording time of 30 seconds. All stress-strain data is presented as engineering stress-strain curves. The yield stress (σ_{ys}) was measured at a plastic strain (ε_{pl}) of 0.2 %.

For calculation of the Young's modulus (E) the first unloading cycle was used rather than the first loading cycle because unintentional deformation of the sample head could occur leading to a significant underestimation of the Young's modulus. More than 60 LCF experiments were performed, at least 10 for each material with an experiment duration of 10 seconds to 50 hours. Elongation was determined automatically with an optical grid (crosshead shift) and test readings were verified by DIC. The plastic strain per cycle, i.e. the creep strain per cycle ($\Delta\varepsilon_{cr}$), was calculated from the cumulated plastic strain $\Delta\varepsilon_{cum}$ (Fig. 1) divided by the number of cycles. Load sensing was based on measurements of the eigenfrequency of a loaded tungsten wire as described in [20]. The standard deviation for all obtained values is shown by the measurement error.

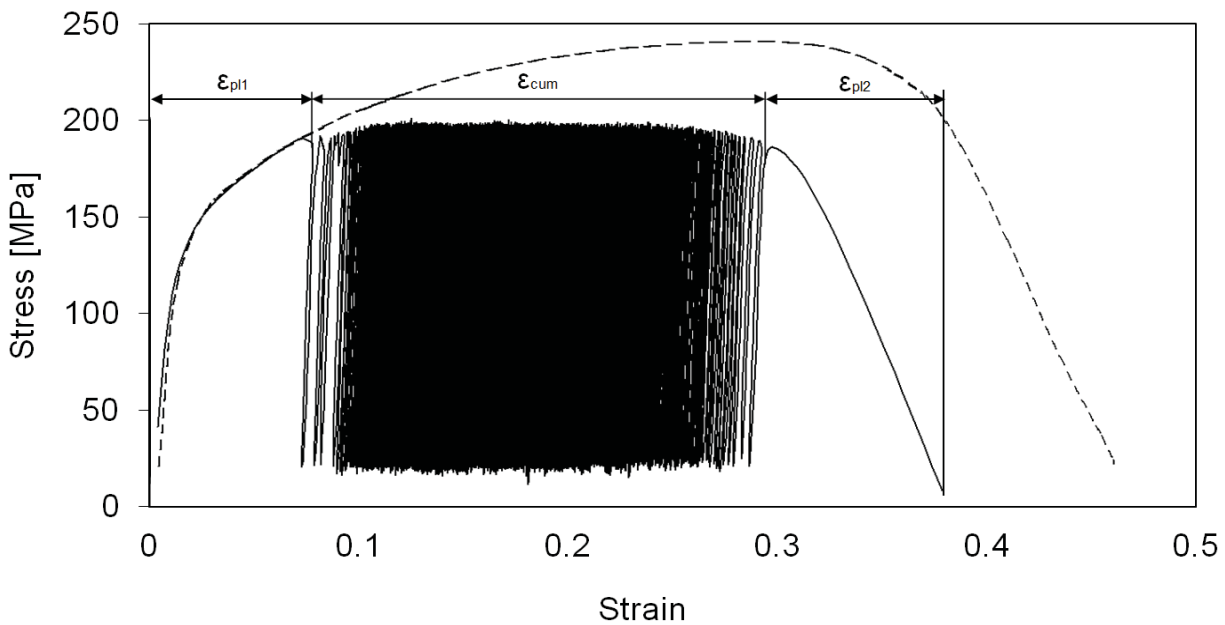

Fig. 1. Typical stress-strain curve for sample B of a tensile test (dashed line; σ_{max} = 240 MPa and N = 1) and fatigue experiment (solid line; σ_{max} = 200 MPa, σ_{min} = 20 MPa and N = 1650).

2.3 Calculation of individual sample global Young's modulus

For the calculation of the global Young's modulus EBSD/SEM images of the sample were virtually divided into 2,600 elements with an area of 1 • 1 µm^2 along the sample width (x-direction) and length (y-direction). For each area element the orientation was determined from the EBSD information and the local Young's modulus E_{xy} (x = 1,2 ,…,20; y = 1,2,…,130) was calculated depending on the orientation [30]. The global Young's modulus of the sample was calculated by a serial connection,

$$E = \frac{130}{\sum_{y=1}^{130} \frac{1}{\sum_{x=1}^{20} \frac{E_{xy}}{20}}} \quad (1)$$

or a parallel connection:

$$E = \sum_{x=1}^{20} \frac{130}{\sum_{y=1}^{130} \frac{20}{E_{xy}}} \quad (2)$$

of the elements with their local Young's modulus.

Eq. 1 assumes a constant strain in all elements E_{xy} (x = 1, 2,…,20; y = const.) of the sample, while Eq. 2 assumes a constant strain in all elements E_{xy} (x = const.; y = 1, 2,…,130). As these two equations describe the two extreme cases, the average of both was taken as the global Young's modulus of the

corresponding sample. However, the difference between the serial and parallel connection model was always < 5 %.

3 Results and Interpretation

In this section the microstructural findings are reported first before presenting the results concerning the static tensile deformation including the Young's modulus. Subsequently, the dynamic tension-tension data and the *in situ* SEM observations are provided.

3.1 Microstructure and morphology

SEM studies of the samples reveal differences in the surface morphology (Figs. 2a-d). Sample A had a smooth surface (R_{max} = 0.1 µm) and sample C had the roughest surface (R_{max} = 2 µm). Samples B and D, which were deposited using the same electrolyte, had a smooth (R_{max} = 0.1 µm), but rounded surface. Recall that the shape of the micro-samples was considered in calculation of the cross-sectional area. These observations were revealed in more detail in the cross-sectional SEM images, where the channeling contrast provides also first information on the grain size (Figs. 2e-h). Although only 3 different growth conditions had been used the samples were divided into 4 types (labeled as samples A to D) since one electrolyte composition resulted in a bimodal grain size distribution (distinguished as samples B and D). EBSD/SEM measurements of the Cu lines confirm the cross-sectional SEM images and clearly revealed the four different grain size distributions (Fig. 3).

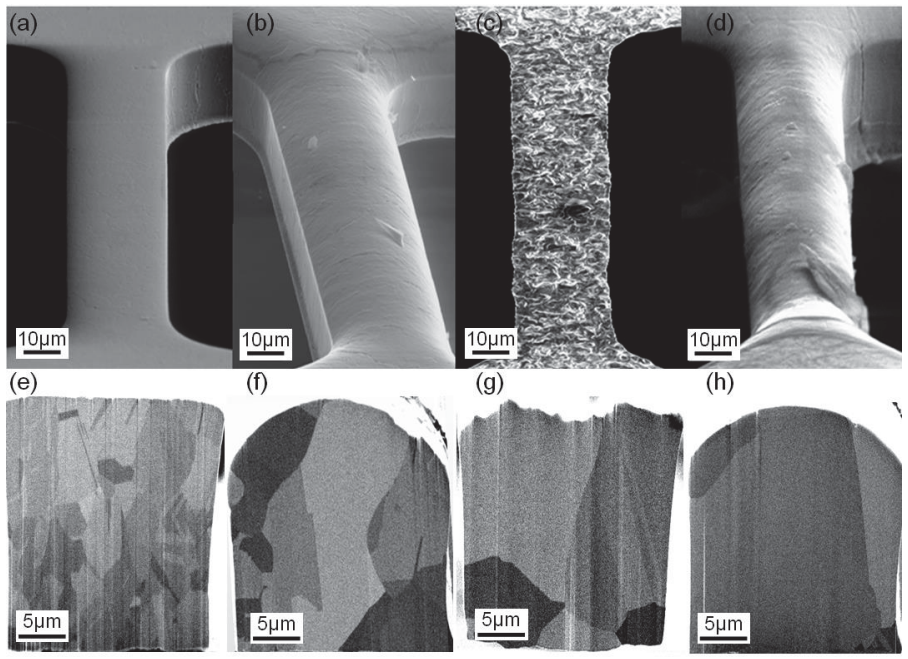

Fig. 2. SEM images of the surface (a-d) and cross-sections (e-h) of the undeformed tensile samples. Note that the grain size increases from the left to the right. (a,e) sample A, (b,f) sample B, (c,g) sample C, and (d,h) sample D.

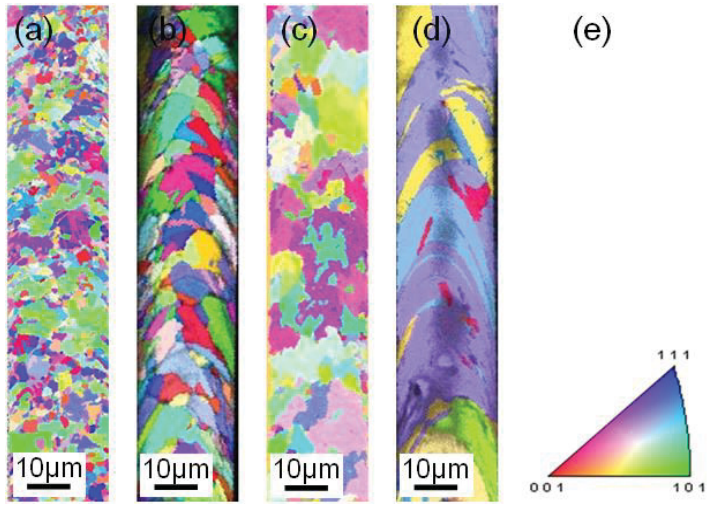

Fig. 3. EBSD/SEM images of undeformed (a) micro-grained Cu (sample A), (b) fine-grained Cu (sample B), (c) medium-grained Cu (sample C), (d) coarse-grained Cu (sample D), and (e) color code of the inverse pole figure corresponding to the grain orientations. Grains of samples B and D can be distorted in lateral direction because of the surface curvature (see Fig. 2f, h).

The cumulative grain size distributions based on the line intercept measurements of the smallest to the largest grains of each sample type (A to D) are presented in Fig. 4. The median grain sizes of the four samples are determined at a cumulative area fraction of 50 % (Fig. 4). The median grain size varies between 2.7 and 13.5 µm. However, more importantly is the number of grains per sample cross-

section. The micro-grained Cu (sample A) with its grain size of only 2.7 µm results in approximately 50 grains per cross-section (Fig. 2). The fine-grained Cu (sample B, grain size of 7.7 µm) and the medium-grained Cu (sample C, grain size of 8.6 µm) possess on average 5 - 10 grains per cross-section, and the coarse-grained Cu (sample D, grain size 13.5 µm) has 1 - 4 grains per cross-section (Fig. 2). As a consequence it can be expected that any single-grained cross-section in sample D will dominate the mechanical properties and may result in a significant spread of the mechanical properties. Tab. 1 indicates the grain sizes of the four different samples; moreover it exhibits the mechanical properties which will be represented later on.

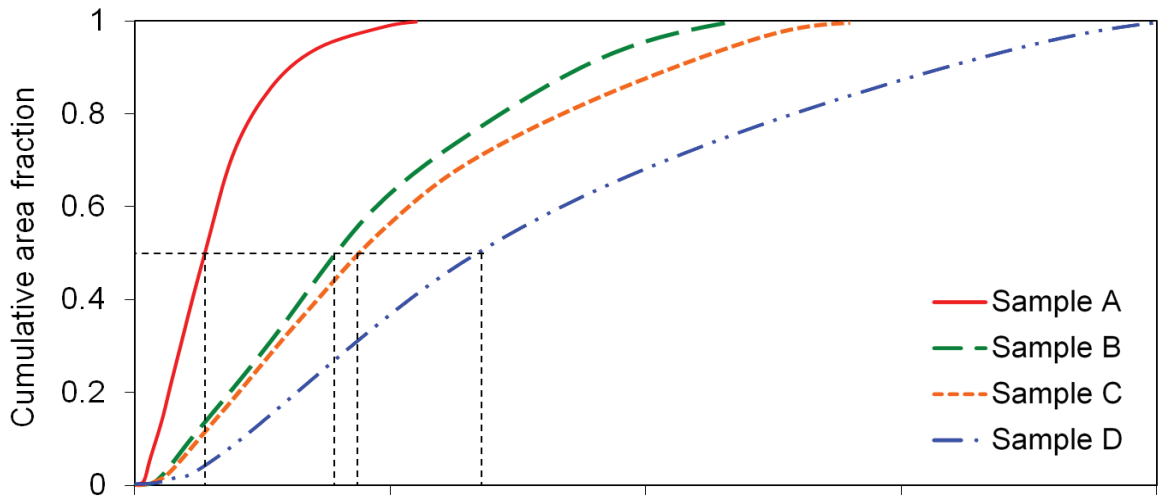

Fig. 4. Cumulative grain-size distribution of the materials. The median grain size, which is defined at a cumulative area fraction of 50 %, is marked with dashed lines. Note that the median grain size increases from sample A to D.

Tab. 1. Grain sizes and mechanical properties of the investigated materials deduced by tensile testing: The median grain size (d), the yield stress (σ_{ys}), ultimate tensile strength (UTS), Young's modulus (E) and elongation to fracture $\varepsilon_{failure}$. The grain size increases from sample A to sample D, the mechanical properties decrease constantly from sample A to sample D.

	d [µm]	σ_{ys} [MPa]	UTS [MPa]	E [GPa]	$\varepsilon_{failure}$
Sample A	2.7 ± 0.3	146 ± 7	291 ± 5	100 ± 15	0.46 ± 0.05
Sample B	7.7 ± 2.9	82 ± 9	235 ± 9	90 ± 10	0.42 ± 0.05
Sample C	8.6 ± 1.0	70 ± 10	196 ± 19	75 ± 10	0.40 ± 0.06
Sample D	13.5 ± 4.7	60 ± 12	177 ± 15	70 ± 20	0.39 ± 0.02

3.2 Static behavior

Fig. 5 shows typical stress strain curves of the four Cu samples. The tensile experiments revealed that the yield stress (σ_{ys}) and ultimate tensile strength (UTS) increased with decreasing grain size (see e.g. Fig. 5, Tab. 1). Even the elongation at fracture showed a slight increase from 0.39 ± 0.02 to 0.46 ± 0.05 with decreasing grain size, i.e. the materials get stronger and on average slightly more ductile. The *in situ* SEM observations during tensile testing showed that the reason for the higher ductility of small-grained samples was their uniform deformation across the whole sample length. In contrast, the coarse-grained material necks preferentially localized in a few large, soft oriented grains (weakest link) while all other grains have hardened or remain nearly undeformed. In large grains, dislocations can escape easily through the free surface, therefore, a high local ductility resulting in a high local elongation is possible. However, as deformation is only localized in a small number of grains the overall sample elongation is on average slightly smaller compared to the fine-grained material where many grains participate in a rather homogenous deformation. Furthermore, the coarse-grained material is in some areas single-crystalline (bamboo-structure), resulting in typical single-crystalline mechanical behavior (Fig. 5). After elastic deformation, the sample showed single slip followed by multiple slip during the first 3 % of straining. This type of behavior is typical for a single-crystalline cross-section.

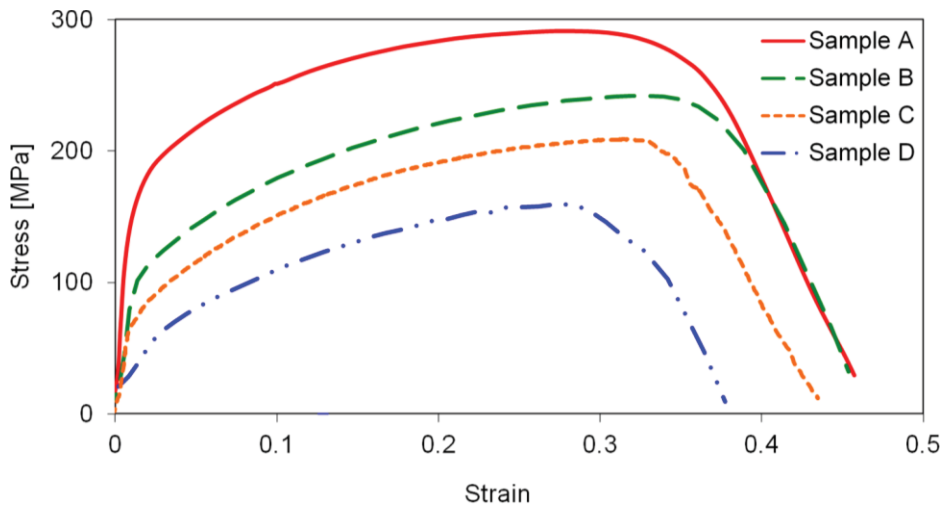

Fig. 5. Typical stress-strain curves of the four different sample types: sample A (red) shows the highest yield stress (σ_{ys}), ultimate tensile strength (UTS) and elongation to fracture. With increasing grain size from sample A (red) over sample B (green) and C (yellow) to sample D (blue) the mechanical performance decreases.

The standard deviation of the yield stress and UTS is caused by a variation of the grain size and orientation between individual samples resulting in varying mechanical properties from one sample to another of the same sample type. The nearest neighbor orientations play a crucial role especially for the coarse-grained samples. Changes in orientation cause a massive change in strength and stiffness resulting in stress concentrations. Consequently, deformation is fostered in the softer <100> grain. For example, if small grains with a hard orientation of <111> are adjacent to large grains with <100> soft orientation along the tensile direction, deformation will tend to be localized in the softer <100> grain. There is a complex interdependency between grain size, grain orientation and deformation behavior of large grains and their nearest neighbor grains. Consequently, *in situ* measurements of grain orientation evolution during deformation are necessary to make a quantitative analysis of the grain-grain interactions. This, however, is beyond the scope of the present work.

For polycrystalline bulk Cu, a Young's modulus of 100 - 130 GPa is usually obtained depending on the average grain orientation. Surprisingly, the Young's modulus also varies for the different samples A to D. This must be ascribed to the local grain orientations in the tensile samples as Cu possesses a high elastic anisotropy. The Young's modulus of a single crystal varies between 65 GPa for the soft <100> orientation and up to 189 GPa for the hard <111> orientation [31]. If there are only a few grains in the sample, significant influence of any soft oriented grain was observed. The experiments indicated that with increasing yield stress (and decreasing grain size) the Young's modulus also increased (Fig. 6). This point will be addressed in the next section where the Young's moduli of the samples are calculated based on the grain orientations of the samples obtained by EBSD studies.

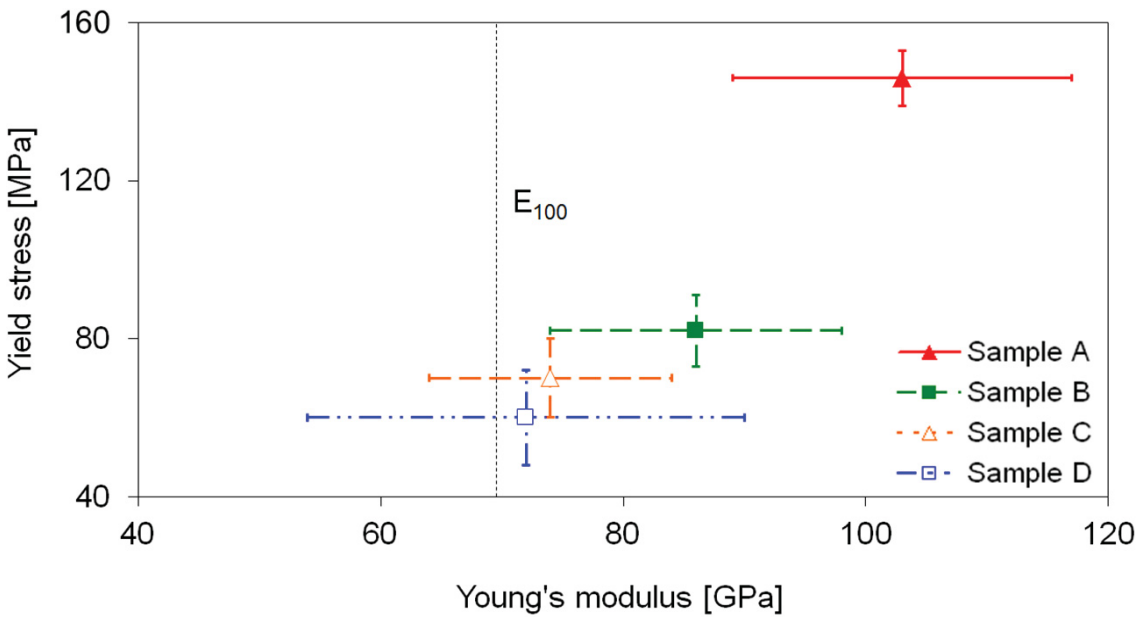

Fig. 6. Yield stress (σ_{ys}) plotted against the Young's modulus (E). With increasing yield stress (decreasing grain size) also the Young's modulus increases. E_{100} marks the Young's modulus of Cu in <100> tensile direction (weakest direction). For comparison the Young's modulus of bulk Cu starts at ≈ 100 GPa [31].

3.3 Estimation of the Young's modulus from EBSD maps

The interaction of grain size on the yield stress or UTS is undisputed [10, 11], however the influence of the grain size on the Young's modulus has had less attention. An explanation for the low Young's modulus of the coarse-grained samples is that one large, weak grain in the specimen could reduce the Young's modulus significantly. 2D-calculations performed using the crystallographic orientation of the grains in tensile directions (measured by EBSD) reveal that a single <100> grain (weakest orientation) covering 25 % of the sample volume can lead to a global Young's modulus of 100 GPa (Fig. 7a). In case of a large, <100> oriented grain which covers 75 % of the sample, the Young's modulus decreases to 70 GPa (Fig. 7b).

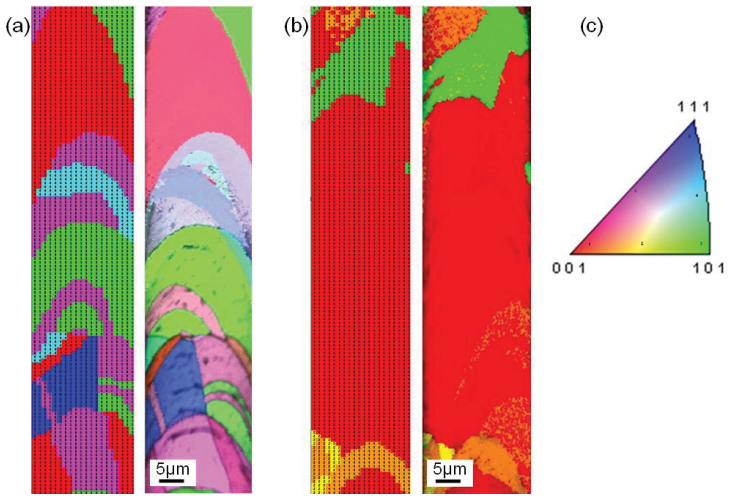

Fig. 7. Calculation of the Young's modulus for typical samples by using the crystallographic information obtained by EBSD/SEM (for mathematical details see 2.3). (a) Simulated microstructure (left) and corresponding EBSD/SEM image (right), 25 % of the grains are <100> oriented, resulting in a Young's modulus of 100 GPa, (b) Simulated microstructure (left) and corresponding EBSD/SEM image (right), 75 % of the grains are <100> oriented, resulting in this case in a Young's modulus of 70 GPa, (c) color code of the inverse pole figure corresponding to the grain orientations in tensile direction.

Another possibility for the reduced Young's modulus could be pre-existing voids or cracks, which would also decrease the measured strengths. However, this is an unlikely explanation because defects had not been found neither in the SEM surface images nor the FIB cross-sectional images. Influences of voids and cracks on Young's modulus were described for nanocrystalline Cu with a grain size < 10 nm [32].

3.4 Low cycle tension-tension behavior

All tested materials show an increase in cycles to failure with decreasing plastic strain (caused by decreasing the load amplitude) per cycle (Fig. 8). There is a linear relationship between the creep strain per cycle and the cycles to failure in a log-log plot. There was no significant difference between the four different types of Cu, but there was still a tendency for a higher lifetime at the same creep strain per cycle for the high strength sample A and a lower lifetime for the softest kind of Cu (sample D) as strain and damage was localized in the largest grains. It has been found, that there was no significant difference in the elongation to fracture between a static and cyclic tensile test (see e.g. Fig. 2), which showed that the lifetime is determined by the creep strain per cycle. The surface of the cycled samples showed no intrusions or extrusions, but rather they showed the same evolution as samples in a static tensile test.

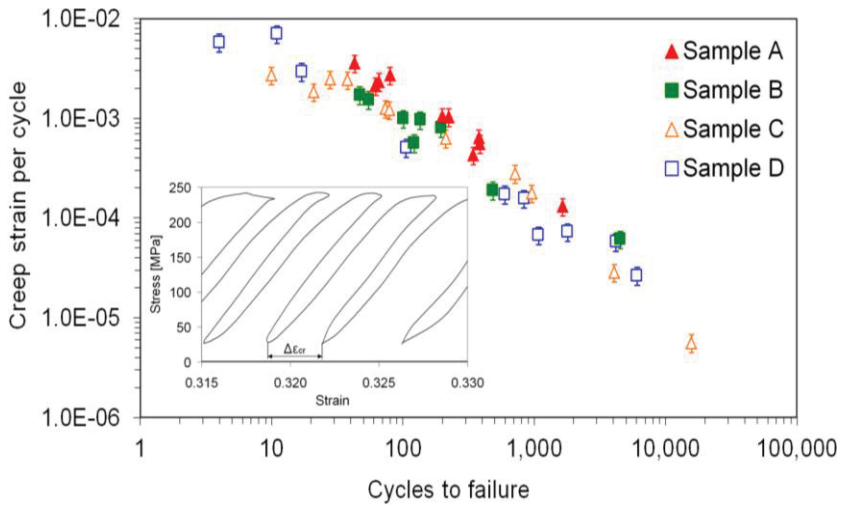

Fig. 8. Creep strain per cycle $\Delta\varepsilon_{cr}$ as a function of the number of cycles to failure. The time to failure increases with decreasing creep strain per cycle. The stress-strain-curve in the insert, which was used for determining the creep strain per cycle, shows a magnified section of Fig. 1.

3.5 *In situ* SEM observations

Depending on the grain size, the samples showed different deformation behaviors. Small-grained samples (A and B) showed a constant deformation during the whole cyclic testing (Fig. 9). Coarse-grained samples (C and D) had a strong deformation at the beginning of the experiment; there was no significant change in topography of the surface between the SEM images after 3 % of lifetime (Fig. 9, top) and 70 % of lifetime (Fig. 9, centre). Only the last cycles before fracture revealed changes in the surface morphology either by necking (samples A-C) or localized slip (sample D) (Fig. 9, bottom). The reason for the insignificant deformation after the first few cycles is that massive hardening in the soft, coarse-grained samples during the first few cycles. Slip bands were becoming visible at the surface of the samples, especially on samples B and D (Fig. 9 and 10) with their smooth surfaces. Sample D, with its bamboo-microstructure, showed a deformation behavior resembling that of a single crystal with slip lines extending across the entire surface. The other three materials showed polycrystalline behavior, since always several grains were contained in the cross-section of the tested samples.

The coarse-grained samples showed in most cases a typical bamboo-structure, i.e. a single grain extended over the entire cross-section. During the first load cycle strong deformation in the weakest grain was observed. Through this deformation, there was a rotation of the grain into a harder direction where multiple

slip replaced the single slip. If there were other grains with a similar soft initial orientation, it became likely that the deformation zone moved into another grain (see Fig. 11). The elongation at fracture was low as the deformation was again localized in another weak grain and the remaining sample was hardly strained.

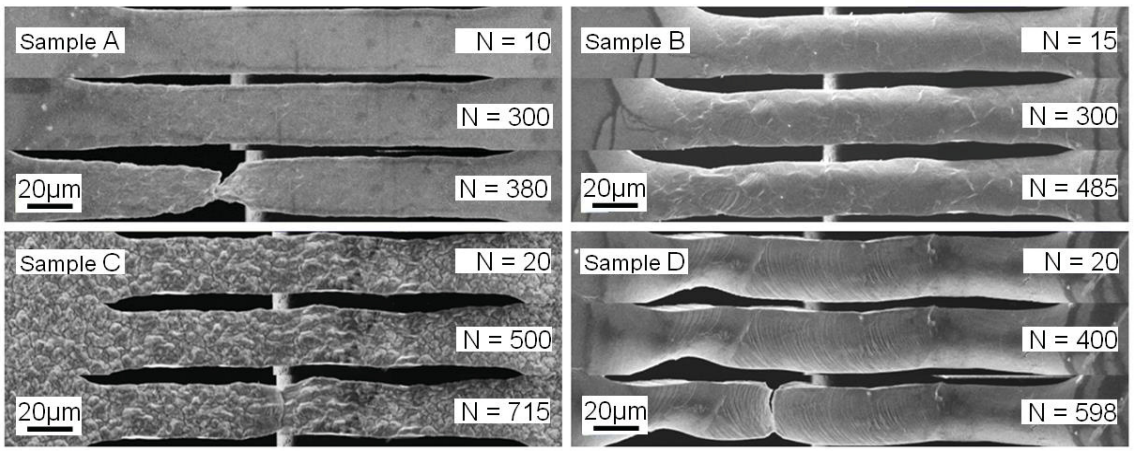

Fig. 9. *In situ* microstructural evolution of the four different materials; deformation up to ≈ 3 % (top), ≈ 70 % (centre) and ≈ 100 % (bottom) of cycles to failure (N). Number of cycles to ≈ 3 % deformation ($N_{0.03}$), to ≈ 70 % deformation ($N_{0.70}$) and to failure (N) are indicated in the pictures. The maximum stress σ_{max} values were: (a) σ_{max} = 238 MPa, (b) σ_{max} = 199 MPa, (c) σ_{max} = 188 MPa, and (d) σ_{max} = 172 MPa.

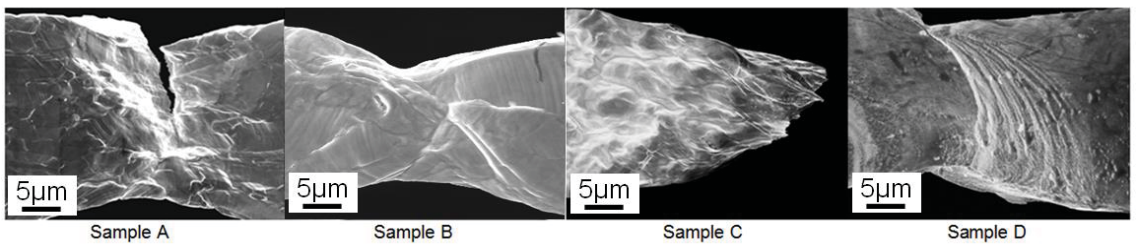

Fig. 10. SEM fracture surfaces of the four different materials. Samples A, B and C show polycrystalline behavior, while sample D with its large median grain size of 13.5 µm shows single-crystalline behavior with mainly single slip in one grain fully extends across the sample diameter.

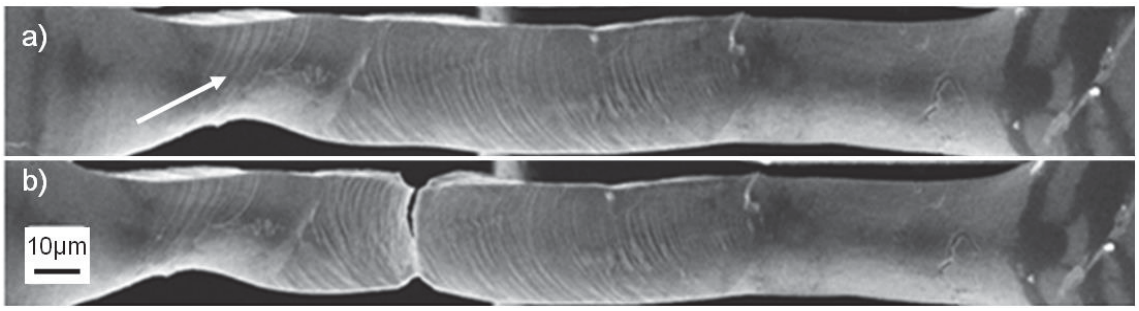

Fig. 11. (a) Strong deformation on the left side (see arrow) during the first cycle, (b) but finally sample D breaks 40 µm to the right of the necked zone.

4 Discussion

In this section the main results concerning the static and dynamic tension tests will be discussed. We will first focus on the influence of grain size on yield stress, UTS and strain to failure before comparing the cyclic creep experiments with $R \approx 0$ to the static tension test and $R = -1$ fatigue tests reported in literature. Differences in the deformation mechanism between experiments with $R = 0$ and $R = -1$ will be analyzed followed by the application of the Basquin equation. An equation will be presented to calculate the time to failure of a sample by the creep strain per cycle. Finally, the influence of the microstructure on the deformation behavior as observed by the *in situ* SEM images recorded during cyclic loading will be discussed.

4.1 Mechanical properties

4.1.1 Static behavior

The σ_{ys} and UTS of the analyzed material was in good accordance with that of macro-sized, small-grained materials [33 - 35] and other micromechanical experiments [12, 20, 36] (see Tab. 2). For single-crystalline microscopic samples the strength increased with decreasing sample dimension because of smaller dislocation sources [37]. Contrary to that, the strength of polycrystalline microscopic samples can increase with increasing sample dimension because for larger sample dimensions unhindered deformation on the free surface becomes negligible [12]. These observations are well known as a mechanical “size-effect” which depends on grain size and sample dimension [12, 37 - 41]. Although the surface roughness plays an important role for the fatigue behavior of macro-size samples [42], the rough surface of the medium-grained sample C (R_{max} = 2 µm) shows no significant disadvantages compared to the smooth surface of the fine-grained Cu (R_{max} = 0.1 µm) in our structures. The reason for this is that the “notches”, which were caused by the rough surface, show a rounded notch base resulting in a negligible notch effect.

There was also a good agreement in the strain to failure to other micromechanical experiments [36]. Others have reported that with increasing sample dimensions and grain-size the strain to failure decreases [20, 33 - 35] (see Tab. 2).

The reason for a decreasing strain to failure with increasing grain size is a localization of deformation in the weakest grain.

Theoretically, the strain-hardening exponent *n*, which is defined by Eq. 3, is between 0 (perfectly plastic solid) and 1 (perfectly elastic solid):

$$n = \frac{d\sigma}{d\varepsilon}\frac{\varepsilon}{\sigma}. \tag{3}$$

The strain hardening exponent, *n*, is the slope of the true stress strain curve (σ-ε curve) in a log-log plot. In this study $n = 0.5 \pm 0.10$ for all analyzed materials taking true stress-strain curves, which agrees well with $n = 0.54$ of macro-sized Cu samples [43].

Tab. 2. Comparison of the mechanical properties of Cu as a function of grain size *d*.

d [µm]	σ_{ys} [MPa]	UTS [MPa]	$\varepsilon_{failure}$	Ref.
2.7 (Sample A)	146 ± 7	291 ± 5	0.46 ± 0.05	this study
7.7 (Sample B)	82 ± 9	235 ± 9	0.42 ± 0.05	this study
8.6 (Sample C)	70 ± 10	196 ± 19	0.40 ± 0.06	this study
13.5 (Sample D)	60 ± 12	177 ± 15	0.39 ± 0.02	this study
0.2*	470	505	0.18	[31]
0.25*	390	440	0.22	[35]
1*	430	460		[44]
3.1	130	235	0.43	[28]
3.1	145 ± 7.8	267.5 ± 1.3		[12]
3.4*	80	245	0.31	[33]
5.0	70 ± 4	208 ± 3		[12]
10*	220	250		[44]
12	43.2	221.5	0.21	[20]
12.5	42.5 ± 3.8	186.3 ± 5.2		[12]
15*	41	230	0.31	[33]
20.1	55	155	0.37	[28]
20.5	31.6	240.4	0.26	[20]
21	32.0 ± 2.7	180.8 ± 5		[12]
100*	80	150		[44]

*…macroscopic samples

In a macroscopic experiment the Young's modulus is only approximated, consequently in a micromechanical experiment the Young's modulus is even more prone to measurement errors. However, the obtained values for the Young's modulus are in the expected range. The standard deviation of up to ± 20 GPa for the softest samples shows that the measurement of the Young's modulus is not very accurate, but an evidence for a good experimental set-up and accurate strain measurement. It is still possible to make a qualitative comparison between the samples. In most other micromechanical studies DIC was not applied with a few exceptions such as [45], where the elastic properties of a ceramic thin film were analyzed. Consequently the displacement resolution is usually insufficient for Young's modulus measurements in micromechanical experiments.

There was a good agreement of the observed yield stress for samples B, C and D with the Hall-Petch relationship (Fig. 12) [10, 11]. Contrary to bulk samples [46 - 48], micron-sized Cu samples with a grain size in the range of 3 µm show a much higher yield stress (Tab. 2). The yield stress observed in this study was in good accordance with that of other studies (Fig. 12) [12, 33, 36]. The most probable reason for the lower yield stress in [12] is the higher purity of the copper (99.998 % compared to 99.99 % in this study). Furthermore, samples in [12] were annealed immediately before mechanical testing in a vacuum furnace at temperatures up to 900 °C, resulting in a lower impurity level and lower dislocation density. The significantly higher values for the yield stress of reference [44] are caused by a pre-deformation resulting in a higher initial dislocation density, however the UTS is in good accordance with this study. For the coarse-grained sample D with a w : d ratio of 1.5, a yield stress of 60 MPa was found, which means a decrease of 60 % compared to the micro-grained sample A with a yield stress of 146 MPa (Tab. 1). This is in good accordance with size dependent experiments on Pt: If the w : d ratio for Pt nanopillars was below 5, a decrease in the yield stress of 36 % compared to bulk Pt was found in the compression test [13].

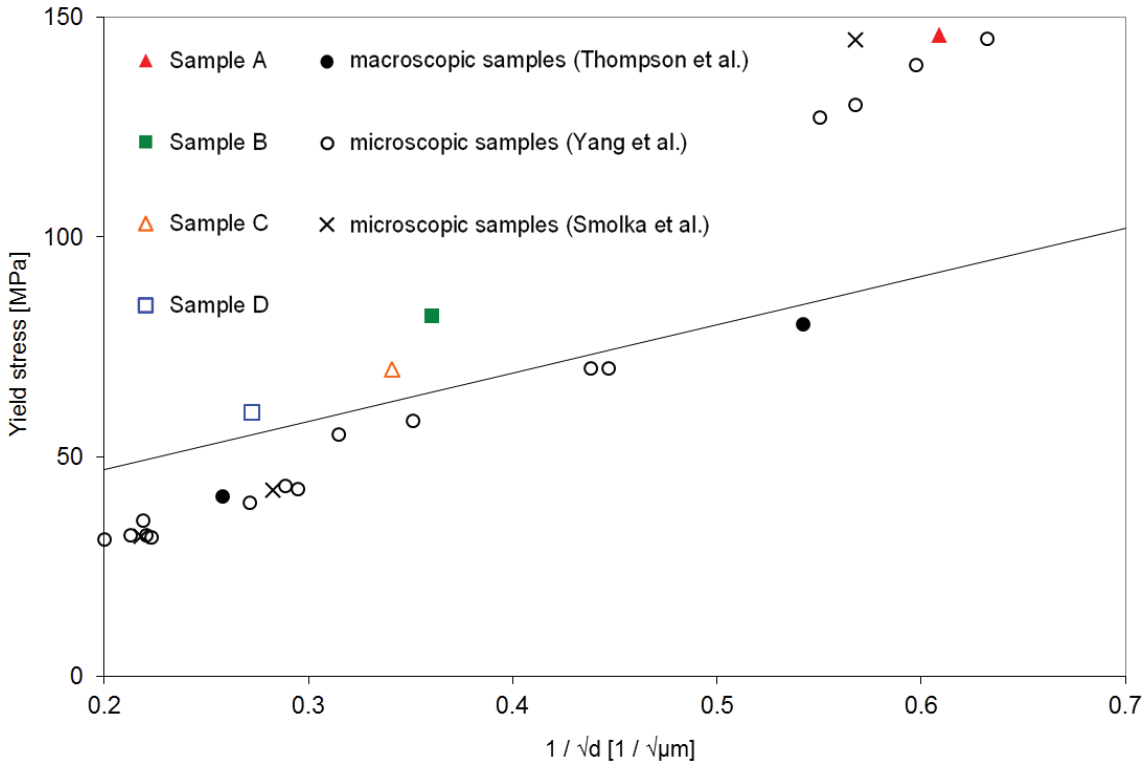

Fig. 12. Hall-Petch plot of the data of Tab. 2, massive line: Hall-Patch relationship [10, 11] using $\sigma_y = \sigma_0 + k / \sqrt{d}$ (lattice friction stress σ_0 = 25 MPa, Hall-Petch slope k = 110 MPa√µm).

4.1.2 Cyclic properties

The surface damage evolution of the samples tested at $R \approx 0$ was close to the surface appearance of samples which underwent static tensile tests. Combining the information obtained from static tension experiments (Tab. 2) and the cyclic tension-tension tests (Fig. 8) one can notice that the statically measured strain to failure also determines how much plastic (creep) strain can be accumulated in the cyclic test. Consequently, the elongation to fracture, ε_f, cumulative creep strain, $\Delta\varepsilon_{cum}$, and the creep strain per cycle, $\Delta\varepsilon / \Delta N$, was plotted against the number of cycles (Fig. 13). Using Fig. 13 it becomes evident that a linear relationship between the creep strain per cycle $\Delta\varepsilon_{cr}$ and the number of cycles to failure N (Eq. 4) was observed:

$$N = \frac{\varepsilon_f - \varepsilon_{pl1} - \varepsilon_{pl2}}{\Delta\varepsilon_{cr}}, \tag{4}$$

where $\varepsilon_f - \varepsilon_{pl1} - \varepsilon_{pl2} = \Delta\varepsilon_{cum}$, ε_f is the elongation to fracture, ε_{pl1} the deformation until the first unloading cycle and ε_{pl2} the deformation after the last unloading cycle (Fig. 2). In other words, the elongation to fracture was constant and independent of the type of experiment. This shows if the Cu reaches a total strain of 0.3 ± 0.05, the sample starts narrowing until fracture occurs at a total strain of 0.4 ± 0.06,

independent of the grain size as revealed in the experiments. In former studies [38] it has been shown, that $\Delta\varepsilon_{cum}$ is constant for a high number of cycles to failure, however no relationship between $\Delta\varepsilon_{cum}$ and the elongation to fracture has been shown.

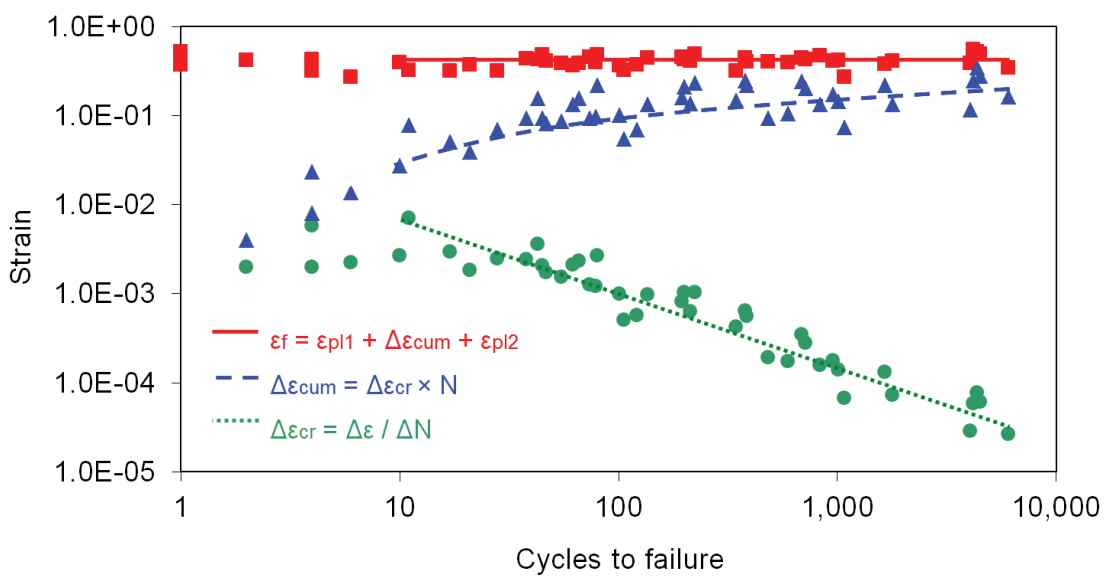

Fig. 13. Elongation to fracture ε_f, cumulative creep strain $\Delta\varepsilon_{cum}$ and creep strain per cycle $\Delta\varepsilon_{cr}$. As the strain values below 10 cycles are prone to inaccuracies because of high static creep during holding time at the maximum stress, lines for the strain start at N = 10.

Although the current experiments with $R \approx 0$ were typical ratcheting experiments, the applicability of a modified Basquin equation [49] was probed as in other ratcheting experiments where the Basquin equation has been successfully applied [20]. Indeed in fatigue experiments with $R \approx 0$ tension deformation is dominating [24] compared to tension and compression deformation at $R \approx -1$, which means a different deformation mechanism. This can be concluded from the *in situ* SEM observations which show no change in surface topography between 3 % and 70 % of the cycles to failure (Fig. 9) and is an indication that there is no significant hardening during cycling. The mechanical behavior reveals the physical background behind Eq. 3, because if hardening and irreversible slip of dislocations would appear an increasing elongation to fracture would be expected.

The Basquin equation

$$\sigma_a = \sigma_f' \bullet (2N)^{-b} \tag{5}$$

was modified to

$$\sigma_{\max} = \sigma_f'' \bullet (2N)^{-b'} \tag{6}$$

Because of the different deformation mechanisms in experiments with $R \approx -1$ and $R \approx 0$. In the Basquin equation the parameters are σ_a (stress amplitude), σ_f' (fatigue stress coefficient) and b (fatigue stress exponent). The parameters of the modified Basquin equation are σ_f'' (static tensile strength) and b' (modified fatigue stress exponent) as shown in Tab. 3. There is a significant difference between the four types of Cu samples. Sample A (fine-grained Cu, 2.7 µm grain size) shows the highest strength under the static conditions as well as in the low cyclic regime when compared to sample D (coarse-grained Cu, 13.5 µm grain size). However, the slope is steeper indicating a lower strength in the high cyclic regime and agrees with experiments on ufg Cu [25, 26]. Referring to the Hall-Petch equation, the tensile strength increases with decreasing grain size [1, 11, 33], consequently also the LCF properties with respect to strength were improved with decreasing grain size (Fig. 14) [31, 34, 50]. The outlier at 110 MPa and 4,000 cycles to failure in Fig. 14 is demonstrating that a small median grain size can be made useless by some large grains, which are dominating the mechanical properties (weakest link).

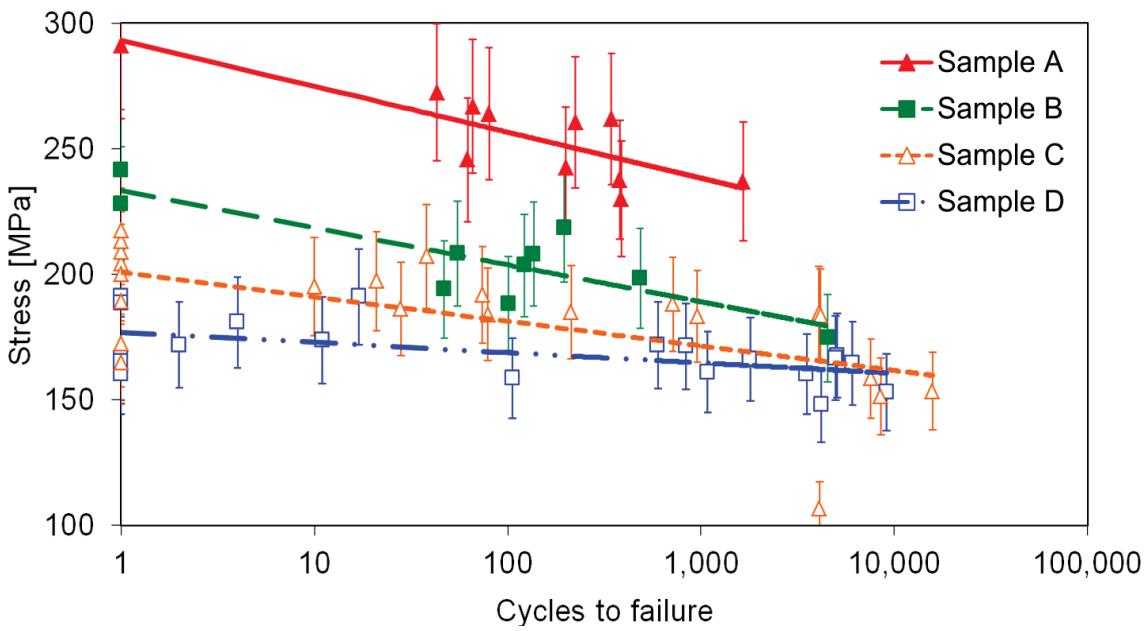

Fig. 14. Stress over cycles to failure. The number of cycles to failure increases with decreasing maximum load, the slope of the curves corresponds to the modified fatigue stress exponent *b*'.

Tab. 3. Cyclic parameters of the analyzed materials: static tensile strength σ_f'', and modified fatigue stress exponent *b*'. With increasing grain size *d* the parameters decrease, e.g. the cyclic behavior gets worse.

	σ_f'' [MPa]	*b*'	*d* [µm]
Sample A	291	0.03	2.7 ± 0.3
Sample B	235	0.03	7.7 ± 2.9
Sample C	196	0.02	8.6 ± 1.0
Sample D	177	0.01	13.5 ± 4.7

For macroscopic samples it is known that for the Basquin equation the slope *b* decreases with increasing grain size, which could lead to better performance of larger grain sizes in the HCF or at least the UHCF (ultra high cycle fatigue) regime [51]. The formula for the cyclic strain hardening exponent *n*'

$$n' = \frac{\ln(\frac{\sigma_a}{K'})}{\ln(\Delta\varepsilon_{pl})} \tag{7}$$

was modified to

$$n' = \frac{\ln(\frac{\sigma_{max}}{K'})}{\ln(\Delta\varepsilon_{cr})}. \tag{8}$$

In a log-log plot of the maximum stress (σ_{max}) and creep strain per cycle ($\Delta\varepsilon_{cr}$) the cyclic strength coefficient (*K*') is the intercept of the curve with the ordinate, and *n*' is the slope of the curve (Fig. 15).

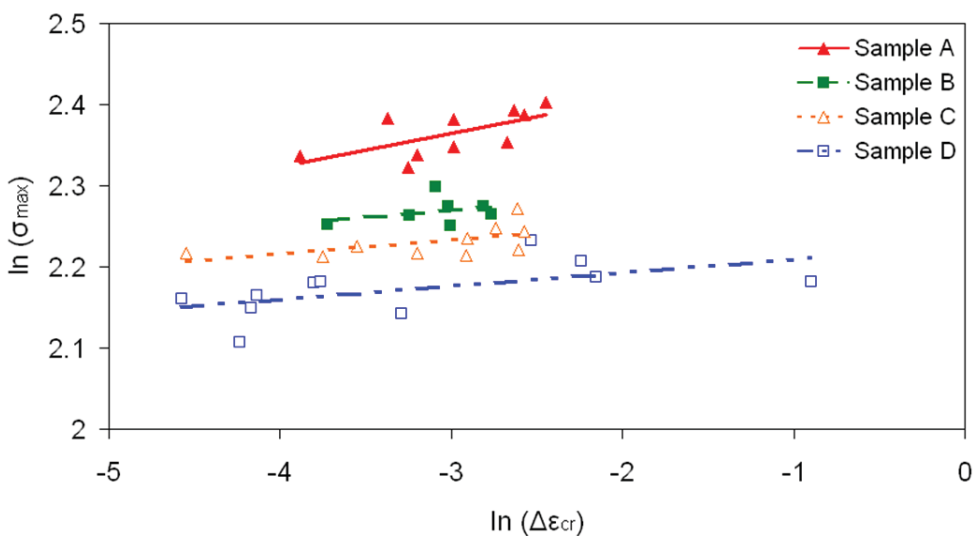

Fig. 15. Log-log plot of σ_{max} and $\Delta\varepsilon_{cr}$, the slope of the curves corresponds to *n*'.

In this study *n*' is between 0.016 and 0.041, which shows a small hardening during cyclic tensile-tensile testing with $R \approx 0$, and agrees well with the *in situ* SEM observations mentioned before. The reason for hardening during cyclic tensile-tensile test is that reversible dislocation movement compared to irreversible dislocation movement with strong hardening in fatigue experiments with $R \approx -1$ and *n*' ranging from 0.1 – 0.2 [24]. In nanograined, macroscopic samples an unexpectedly high value of *n*' = 0.3 was observed [52, 53], meaning significant hardening during cycling and cannot be explained. The following formula describes a relationship between *b* and *n*' [54]:

$$b = \frac{n'}{(1+5n')}. \tag{9}$$

The calculated values for *b* using Eq. 9 and Fig. 15 were between 0.015 (sample D) and 0.034 (sample A), which was in good accordance with the values for *b*' obtained from Eq. 6 using Fig. 14 and were between 0.01 (sample D) and 0.03 (sample A).

4.2 Deformation behavior

Comparing the fatigued samples of this study (with $R \approx 0$ and uniaxial loading) with fatigued samples of thin films on a substrate (with $R \approx -1$ and biaxial loading), there was a significant difference in surface damage. The thin films on a substrate samples with $R \approx -1$ showed intrusions and extrusions formed by tension and compression deformation, especially in large, <100> grains [24]. While the fatigued samples of this study with $R \approx 0$ showed surface evolution similar to a tensile test (Fig. 10). Tension-tension experiments of polycrystalline Cu thin films on a polymer substrate also showed the formation of intrusions and extrusions resulting from residual tensile stress in the polymer substrate inducing compression stress in the Cu thin film [55]. The deformation behavior in combination with Eq. 3 showed that experiments in the tension-tension regime can be described more precisely as ratcheting or cyclic creep experiments instead of fatigue experiments. In a typical fatigue experiment (with $R \approx -1$) $\varepsilon_{pl} \cdot N$ is 100 – 1,000 times larger than the elongation to fracture. Furthermore, the cycles to failure were determined by three phases: crack initiation, crack propagation and final failure. In the presented ratcheting experiments (with $R \approx 0$) $\Delta\varepsilon_{cr} \cdot N$ was on the order of the elongation to fracture, as there is only an irreversible plastic deformation. The tension-tension low cyclic experiments showed no significant crack initiation and propagation, rather the experimented showed plastic deformation with necking and a sudden failure. Nevertheless, it is possible to describe the cycles to failure in the ratcheting experiments with a modified Basquin equation (Eq. 6).

5 Summary and conclusions

Tensile samples with a cross-section of 20 • 20 μm^2 and a length of 130 µm were produced by electrolytic deposition from aquatic solutions with different process conditions to produce tensile samples with four different grain sizes. The samples were cyclically loaded in a tension-tension LCF experiment with the number of cycles ranging between 1 (tensile test) and 15,000. When the grain size was much smaller than the sample width, the samples showed polycrystalline behavior with multiple slip. When the grain size was on the order of the sample cross-section dimensions, the samples behaved like single crystals with mostly single slip of the weakest grain during deformation. A linear relationship between the creep strain per cycle (damage per cycle) and the lifetime was found. In addition, a strong linear relationship between the maximum tension stress and the number of cycles to failure (Basquin equation) was also observed. Not only the number of cycles to failure in the fatigue test, but also the yield stress and UTS increased with decreasing grain size. A similar effect can be observed for the Young's modulus as a consequence of the grain orientations of the grains in the sample.

The micro-grained Cu (sample A), which has by far the smallest and most uniform grain size, possesses the most outstanding mechanical properties with the highest yield stress and UTS of this study. However it does not make sense to relate the mechanical properties to the median grain size as there can be a large variation in grain size distribution which can lead to poor mechanical properties. It was shown that for the Cu structures a small median grain size can be made ineffectual in the presence of a few large grains. This is because deformation will be localized in large grains and prevents homogenous deformation. In other words, the mechanical properties depend on the maximum grain size and orientation, and not the median grain size of the sample.

Acknowledgment

Part of this work was jointly funded by the Austrian Research Promotion Agency (FFG, Project No. 831163) and the Carinthian Economic Promotion Fund (KWF, contract KWF-1521|22741|34186). The authors want to thank M. Cordill, J. Fugger and M. Smolka. Thanks for technical assistance is expressed to M. Augustin, H. Felber, R. Grilz, H. Groß, F. Hubner, M. Krug, R. Leuschner, C. Lindner, K. Matoy, S. Modritsch, G. Moser, T. Ostermann, G. Reiter, H. Schönherr and K. Schrettlinger.

References

1 SM Sze, Semiconductor Devices: Physics and Technology, Wiley-Interscience, (2012).

2 R Doering, Y Nishi, Handbook of Semiconductor Manufacturing Technology, CRC Press 2, (2012).

3 S de Filippis, V Košel, D Dibra, S Decker, H Köck, A Iracea, Microel. Reliab. 51, 9–11, (2011), 1954-1958.

4 QG Zhang, X Zhang, BY Cao, Appl. Phys. Lett. 89, (2006), 114102.

5 W Wu, SH Brongersma, M Van Hove, K Maex, Appl. Phys. Lett. 84, 15, (2004), 2838-2840.

6 O Kraft, R Schwaiger, P Wellner, Mat. Sci. Eng. A 319–321, (2001), 919-923.

7 R Huang, W Robl, H Ceric, T Detzel, G Dehm, IEEE Transactions on Device and Materials Reliability 10, 1, (2010), 47-54.

8 M Seita, CM Pecnik, S Frank, R Spolenak, Acta Mater. 58, (2010), 6513-6525.

9 P Sonnweber-Ribic, P Gruber, G Dehm, E Arzt, Acta Mater. 54 (2006) 3863-3870.

10 EO Hall, Proc. Roy. Soc. B 64, (1951), 747-753.

11 NJ Petch, J. Iron Steel 174, (1953), 25-28.

12 B Yang, C Motz, M Rester, G Dehm, Phil. Mag. 92, 25-27, (2012), 3243-3256.

13 XW Gu, CN Loynachan, Z Wu, YW Zhang, DJ Srolovitz, JR Greer, Nano Lett. 12, (2012), 6385-6392.

14 DC Jang, JR Greer, Scr. Mater. 64, (2011), 77.

15 GP Zhang, CA Volkert, R Schwaiger, P Wellner, E Arzt, O Kraft, Acta Mater. 54, (2006), 3127-3139.

16 DT Read, Int. J. Fatigue 20, 3, (1998), 203-209.

17 S Hong, R Weil, Thin Solid Films 283, 1-2, (1996), 175-181.

18 N Murata, K Tamakawa, K Suzuki, H Miura, International Conference on Electronic Materials and Packaging, (2008), EMAP 2008.

19 R Hofbeck, K Hausmann, B Ilschner, HU Kunzi, Scripta Metall. 20, 11, (1986), 1601-1605.

20 B Yang, C Motz, W Grosinger, G Dehm, Mat. Sci. Eng. A 515, (2009), 71-78.

21 HJ Maier, P Gabor, N Gupta, I Karaman, M Haouaoui, Int. J. of Fat. 28, (2006), 243-250.

22 YB Park, R Mönig, CA Volkert, Thin Solid Films 504, (2006), 321-324.

23 GP Zhang, CA Volkert, R Schwaiger, R Mönig, O Kraft, Microel. Reliab.47, (2007), 2007-2013.

24 YB Park, R Mönig, CA Volkert, Thin Solid Films 515, (2007), 3253-3258.

25 SZ Han, M Goto, C Lim, CJ Kim, S Kim, Journal of Alloys and Compounds 434–435, (2007), 304-306.

26 G Khatibi, J Horky, B Weiss, MJ Zehetbauer, Int. J. of Fat. 32, (2010), 269-278.

27 L Kunz, P Lukáš, L Pantělejev, O Man, Proc. Eng. 10, (2011), 201–206.

28 M Smolka, C Motz, T Detzel, W Robl, T Griesser, A Wimmer, G Dehm, Rev. Sci. Instrum. 83, 6, (2012), 064702.

29 B Yang, C Motz, W Grosinger, W Kammrath, G Dehm, Int. J. Mater. Res. 99, (2008), 716-724.

30 D Armstrong, A Wilkinson, S Roberts, J. Mater. Res. 24, 11, (2009), 3268-3276.

31 A Vinogradov, M Maruyama, S Hashimoto, Scripta Mater. 61, (2009), 817-820.

32 PG Sanders, JA Eastman, JR Weertman, Acta Mater. 45 (1997), 4019-4025.

33 AW Thompson, WA Backofen, Acta Metall. 19, 7, (1971), 597-606.

34 HM Ledbetter, ER Naimon, J. Phys. Chem. Ref. Data 3, 4, (1974), 897-931.

35 SR Agnew, AY Vinogradov, S Hashimoto, JR Weertman, J. Electr. Mater. 28, (1999), 1038-1044.

36 M Smolka, PhD-Thesis, University of Leoben, (2011).

37 D Kiener, W. Grosinger, G. Dehm, R. Pippan, Acta Mater. 56, (2008), 580-592.

38 DY Lee, JH Song, Int. J. of Fat. 38, (2012), 1-6.

39 X Hou, NM Jennett, Acta Mater. 60, (2012), 4128-4135.

40 DJ Dunstan, JU Gallé, XD Hou, KMY P'ng, AJ Bushby, B Yang, D Kiener, Phil. Mag. 92, 25-27, (2012), 3199-3215.

41 NM Jennett, R Ghisleni, J Michler, Appl. Phys. Lett. 95, (2009), 123102.

42 JH Ryu, SW Nam, Int J. Fat. 11, 6, (1989), 433-436.

43 JR Low, F Garofalo, Proc. Sec. Exp. Stress Anal. 4, 2, (1947), 16-25.

44 S Scheriau, Master-Thesis, University of Leoben, (2005).

45 C Eberl, DS Gianola, X Wang, MY He, AG Evans, KJ Hemker, Acta Mater. 59, (2011), 3612-3620.

46 PG Sanders, CJ Youngdahl, JR Weertman, Mater. Sci. Eng. A 234–236, (1997), 77-82.

47 RA Masumura, PM Hazzledine, CS Pande, Acta Mater. 46, (1998), 4527-4534.

48 WF Smith, J Hashemi, Foundations of Mat. Sci. and Eng., McGraw-Hill, New York, (2006).

49 OH Basquin, Proc. of the American Society for Testing and Materials, 10, (1910), 625.

50 L Kunz, P Lukáš, M Svoboda, Mat. Sci. Eng. A 424, (2006), 97-104.

51 A Zhao, J Xie, C Sun, Z Lei, Y Hong, Int. J. of Fat. 38, (2012), 46-56.

52 H Mughrabi, HW Höppel, M Kautz, Scripta Mater. 51, (2004), 807-812.

53 HZ Ding, H Mughrabi, HW Höppel, Fatigue & Fracture of Eng. Mat. & Struct. 25, 10, (2002), 975-984.

54 JD Morrow, Internal Friction, Damping and Cyclic Plasticity, ASTM STP 378, (1965), 72.

55 O Kraft, P Wellner, M Hommel, R Schwaiger, E Arzt, Z. Metallkd. 93, (2002), 392-400.

Paper C

Micro-tension and ratcheting study of miniaturized Cu lines at variable temperature

A. Wimmer [a], W. Heinz [a], A. Leitner [b], T. Detzel [c], W. Robl [d], C. Kirchlechner [b,e], G. Dehm [e,f]

a Kompetenzzentrum Automobil- und Industrie-Elektronik GmbH, A-9524 Villach, Austria
b Department Materials Physics, Montanuniversitaet Leoben, A-8700 Leoben, Austria
c Infineon Technologies Austria AG, A-9500 Villach, Austria
d Infineon Technologies Germany AG, D-93049 Regensburg, Germany
e Max-Planck-Institut für Eisenforschung GmbH, D-40237 Düsseldorf, Germany
f Erich Schmid Institute of Materials Science, Austrian Academy of Sciences, A-8700 Leoben, Austria

submitted manuscript (2014)

Abstract

In this study static tension and cyclic tension-tension (ratcheting) experiments on Cu micro-samples at temperatures up to 873 K (tensile testing) and 673 K (cyclic testing), respectively, were performed. In static tensile experiments the influence of grain size, temperature and strain rate on the mechanical properties was studied. Finally the activation energy and evolution of the dislocation density have been analyzed to identify the deformation mechanisms with respect to strain rate, grain size and temperature. A transition from bulk-like to stochastic, small scale behavior has been found with increasing grain size. Furthermore a change from dislocation based plasticity to diffusion controlled deformation was observed.

The ratcheting experiments were used to obtain stress- and temperature-dependent lifetime curves. It is demonstrated, that for cyclic experiments the number of cycles to failure is dominated by the plastic strain per cycle independent of the temperature. Scanning electron microscopy observations revealed that the deformation mechanisms of cyclic tension-tension experiments at elevated temperatures are similar to that of a tensile test.

1 Introduction

For microelectronic applications both the electrical and mechanical properties of Cu must be optimized. Usually, an improvement of the electrical properties by e.g. increasing the grain size or incorporation of a grain boundary allocation with well-defined impurities [1] has adverse effects on the mechanical properties. Furthermore mechanisms such as grain boundary pinning by non-metallic elements, which optimize both the electrical and mechanical properties at 293 K, can result in embrittlement at elevated temperatures [2]. Consequently the microstructural optimization has to be handled with care in order to find an optimum balance for opposing property trends.

In several studies it has been shown, that a small grain size has positive effects both on static and dynamic mechanical properties [3 - 10]. The ongoing trend for miniaturizing of microelectromechanical systems (MEMS) and the systematic study of mechanical properties of materials at the micro length scale revealed a

transition of the bulk like behavior to stochastically controlled small scale behavior at room temperature if the sample size to grain size ratio D : d is below 5 [6, 11, 12]. Consequently with tensile tests at elevated temperatures the influence of temperature on the deformation behavior can be studied. These static experiments can be also used for the determination of activation energies and volumes which can be subsequently utilized for confirming the deformation mechanisms observed in the scanning electron microscope (SEM).

Furthermore the dynamic mechanical properties of metallic thin films at elevated temperatures are of great interest for microelectronic applications, as most devices are operated at various temperatures (e.g. caused by Joule heating) with up to 10^{10} loading cycles prior to fracture. However, up to now no cyclic tests of micron-sized samples at variable temperatures have been reported in literature.

In a previous study the dynamic behavior of micron-sized Cu samples at 293 K was reported [13]. In the present study the focus is placed on static and cyclic tension-tension experiments at variable temperatures with up to 8,500 cycles to failure. The static tensile tests were performed between 143 and 873 K. Analysis of the strain-rate sensitivity, activation energy and *in situ* like electron backscatter diffraction (EBSD) observations have been used to identify the underlying deformation mechanism across the temperature regime.

2 Experimental details

2.1 Preparation and characterization of the samples

Cu samples were deposited from a sulfuric acid based copper electrolyte onto silicon wafers. Dependent on the additives in the electrolyte system 3 different kinds of samples with an average grain size of 2.7 ± 0.6 µm, 8.6 ± 1.0 µm and 10.1 ± 2.6 µm were achieved. Finally the silicon was etched away to get free standing tensile samples; details about deposition and structuring processes are described in [14]. Some grains spread across the entire cross-section of the micron sample (comparable to a bamboo-like microstructure) leading to a single-crystal like mechanical response. In such a case the sample is not listed within the 10.1 µm grain size samples but rather called “bamboo” sample. Note that the samples in [13]

with a grain size of 13.5 µm comprise the samples subdivided in this study into a grain size of 10.1 µm and bamboo samples.

2.2 *In situ* mechanical testing between 293 K and 873 K inside a SEM

In total 125 static and 95 cyclic experiments were performed *in situ* with a micro-tensile device [14, 15] from Kammrath & Weiss inside a scanning electron microscope (SEM). The set-up has a load noise floor level of ≈ 0.05 mN, which is close to the resolution limit of 0.01 mN. The sample dimensions, which were measured in a SEM and used for stress calculation, were approximately 20 • 20 μm^2 in cross-section and 130 µm in length, excluding the sample head. For static experiments three different strain rates of 0.001 s^{-1}, 0.01 s^{-1} and 0.1 s^{-1} were used, resulting in an experimental time between 5 and 500 s. In case of the cyclic loading experiments the strain-rate was kept constant at 0.001 s^{-1}. The movement of the gripper was performed in displacement controlled mode until an upper and lower engineering stress limit of up to 272 MPa and ≈ 25 MPa was reached. The cyclic loading and unloading was performed between the selected upper and lower stress limits. During the cyclic tension-tension experiments several holding periods of up to 30 s were implemented to record SEM images to follow the damage evolution.

For experiments at elevated temperatures up to 873 K resistive heating elements were used as described in [14]. The thermocouples for temperature measurements are located at a distance of 3 mm from the tensile samples. Finite element simulations predict a sample temperature 15 K lower than the measured temperature at 673 K, for 873 K a difference of 40 K was prognosticated. Three additional thermocouples were installed, recording the temperature of the load cell, the optical elongation sensor and the ground plate of the strain stage to ensure that during the experimental time of up to 72 h the device temperature remains below 373 K. The temperature was kept constant for 30 min prior to deformation, resulting in a maximum drift lower than 4 mN / h independent of the measurement temperature. This linear drift was subsequently corrected in the mechanical data. The maximum scatter in temperature recorded by the thermocouple for the static experiments was ± 2 K and ± 5 K for the cyclic experiments. Even after cyclic experiments at 673 K and experimental times exceeding 3 h EBSD patterns with a low noise level were obtained after cooling to 293 K, demonstrating negligible surface contamination or oxidation during the experiment.

Elongation of the samples was calculated from the displacement of the gripper, measured by an optical grid. The machine compliance analyzed via digital image correlation (DIC) was corrected in the stress vs. strain curves. The load was measured by a tungsten wire oscillating at its load dependent eigenfrequency [16, 17].

The yield strength σ_{ys} was measured both for static and cyclic experiments at a plastic strain ε_{pl} of 0.002. The maximum stress σ_{max} for the cyclic experiments was calculated from the average peak load. For the cyclic tension-tension experiments at variable temperatures we follow the nomenclature of reference [13] for room temperature tests and summarized below: Three strain intervals are considered: ε_{pl1} is the static plastic strain up to the first unloading cycle, $\Delta\varepsilon_{cum}$ is the cumulated plastic strain during cycling and ε_{pl2} is the plastic strain taken from the last loading cycle until rupture, which is defined here if the stress level drops below σ_{final} = 30 ± 30 MPa (see Fig. 1). The experiments were stopped before the sample failed completely (i.e. the load drops to 0) to keep the entire gauge section for post mortem analysis. The plastic strain per cycle, $\Delta\varepsilon_{cr}$ was calculated by dividing the cumulative plastic strain during cyclic loading, $\Delta\varepsilon_{cum}$, by the number of cycles N [13]. The elongation to fracture, ε_f, is defined as:

$$\varepsilon_f = \varepsilon_{pl1} + \Delta\varepsilon_{cum} + \varepsilon_{pl2}\,. \qquad (1)$$

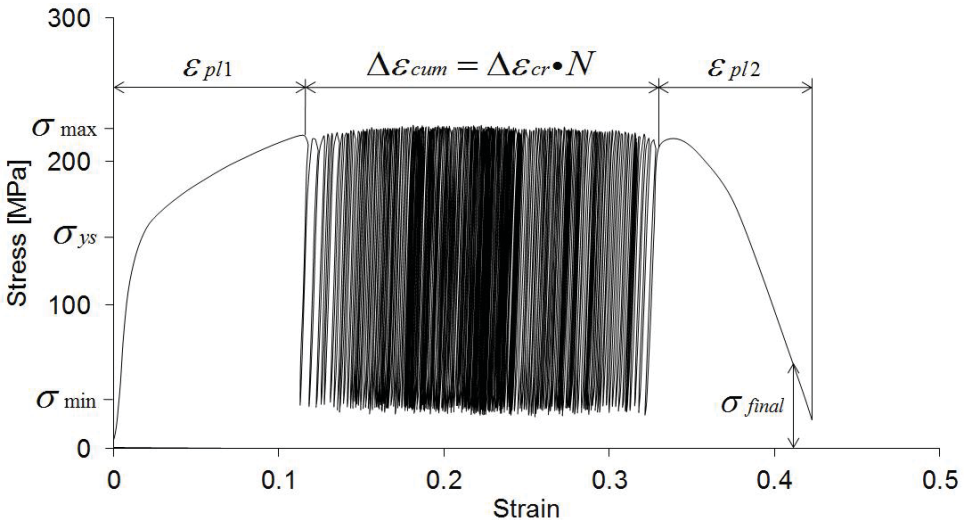

Fig. 1. Typical stress-strain curve of a cyclic tension-tension test at 293 K (σ_{max} = 224 MPa, σ_{min} = 30 MPa, σ_{ys} = 144 MPa and N = 200). σ_{final} indicates the stress range where the experiments were stopped.

2.3 Mechanical testing between 143 K and 293 K under an optical microscope

The low temperature experiments were only performed on the material with 2.7 µm grain size. The tensile tests were conducted under an optical microscope (Olympus SZX16, SDF PLAPO 1XPF) with the same tensile test device as used for the *in situ* SEM experiments. The clamps with the sample and gripper were cooled with liquid nitrogen (N_2) by dipping a pin into a small polystyrol (PS) bowl with liquid N_2 (Fig. 2). As soon as the experimental temperature was reached the experiment was started. To keep the measured temperature changes during the experiment low (< 10 K) a medium strain rate of 0.01 s^{-1} was used to ensure an experimental time below 60 s. During the experiment the N_2 level decreases as no N_2 was refilled to prevent vibrations, resulting in a noise floor level < 1 mN. As a consequence, an increase of the temperature of about 10 K/min was measured by the thermocouples inside the clamps holding the gripper and the tensile sample, resulting in a thermal drift of the load cell of < 3.5 mN / min for all experiments between 143 K and 293 K. The maximum drift leads to an uncertainty of less than 2 % of the ultimate tensile strength (UTS) which is considered to be negligible. Furthermore, finite element simulations, performed under the assumption of steady state conditions, indicate that at 103 K the sample temperature is expected to be up to 30 K higher than the measured temperature of the thermocouple which is attached at the closest possible distance, which is approximately 3 mm next to the tensile samples. Formation of ice on the sample surface by condensation of atmospheric H_2O was minimized by using a transparent polyethylene (PE) shielding (Fig. 2).

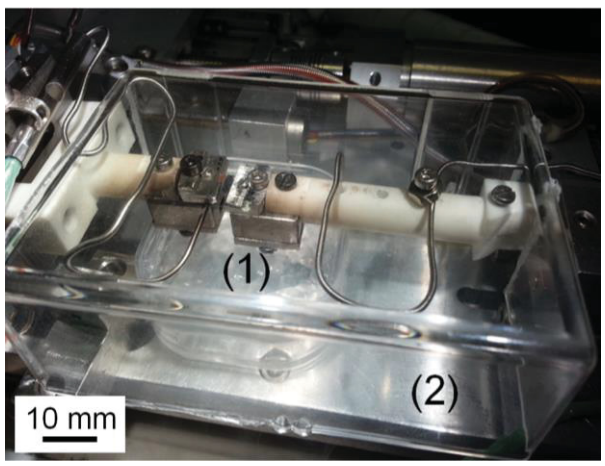

Fig. 2. Experimental set-up for *in situ* testing between 143 K and 293 K. The plastic bowl (1) below the clamps contains liquid N_2 for cooling. The transparent PE shielding (2) on the top reduces H_2O condensation on the tensile sample and gripper.

2.4 *In situ* like EBSD and calculation of the GND density

For the *in situ* like EBSD measurement the set up was tilted to 70° and installed inside a Zeiss LEO 1525 equipped with an EDAX DigiView 1612 EBSD system. The mechanical tests were paused at certain strain values to record EBSD scans and then continued leading to *in situ* like EBSD observations.

A step size of 0.5 µm for the area of interest (20 • 130 μm^2) was used with 8 • 8 camera binning in order to find a good compromise between short recording time (typically 5 min) and high pattern quality. Except for the *in situ* like EBSD experiments of the 10.1 µm grained samples, where a little cusp caused by electrolytic deposition was removed by focused ion beam (FIB), no surface treatment was required to obtain EBSD patterns for the Cu samples. EBSD images were processed with TSL OIM 5.31 software to determine the local Kernel average misorientation (KAM). Based on the KAM a lower bound of the geometrically necessary dislocation (GND) density ρ_{GND} was estimated under the assumption that the misorientation is caused by two perpendicular arrays of screw dislocations as described in [18] by Kubin and Mortensen. In that case the GND density is calculated by:

$$\rho_{GND} = \frac{2\kappa}{b}, \tag{2}$$

where b = 2.56 • 10^{-10} m is the Burgers vector and κ [rad] is the lattice curvature (approximated by the KAM, measured between a point and its second nearest neighbor to minimize noise) over a unit length x (two times the step size of 0.5 µm in case of the second nearest neighbor):

$$\kappa = \frac{KAM}{x}. \tag{3}$$

The theoretical resolution limit of EBSD is ± 0.2°, consequently the resolution for the apparent GND density is ± 3 • 10^{13} m^{-2}; furthermore, this is also the lowest detectable GND density. This value was confirmed by a slightly higher apparent GND density in the undeformed sample of 7.0 ± 3.0 • 10^{13} m^{-2}. The higher value is mainly caused by the used camera binning of 8 • 8.

Lattice curvatures > 15° between two measurement points were defined as a grain boundary, consequently the upper limit for the GND density is 2 • 10^{15} m^{-2}. This limit is rather theoretical, as such high GND densities would degrade the quality of the Kikuchi patterns and consequently prevent their analysis. The *in situ* like EBSD

experiments presented here focus on one annealed (5 h, 1073 K) sample with a grain size of 15.9 ± 3.4 µm and partially bamboo-like microstructure. However, experiments have been performed on several samples with different grain sizes which can be found in appendix B.

2.5 Calculation of the activation energy

For calculation of the apparent activation energy, Q, the temperature dependence of the yield strength is considered [19]:

$$Q = \frac{R}{m} \frac{d(\ln(\sigma_{ys}))}{d(\frac{1}{T})}, \tag{4}$$

where R = 8.314 J K^{-1} mol^{-1} is the universal gas constant, m = 0.01 [21, 22] the strain-rate sensitivity and T [K] the temperature. Hence, if the logarithmic yield strength is plotted against the reciprocal temperature 1 / T the slope of the curve can be used to determine the activation energy.

3 Results

3.1 Deformation patterns depending on grain sizes and temperature

The post mortem SEM images of samples deformed at room temperature (Fig. 3, left column) shows extensive slip steps and necking, both well known to occur when dislocation slip mechanisms are active. For the largest and intermediate grain size samples this observations hold true also at high temperatures. However, in the samples with the smallest grain size a change in deformation mechanism is observed (Fig. 3, lowest line): Already at intermediate temperatures cracks open at grain boundaries which is more extensively observed at high temperatures. At 873 K pores can be found at grain boundaries and triple junctions (Fig. 4).

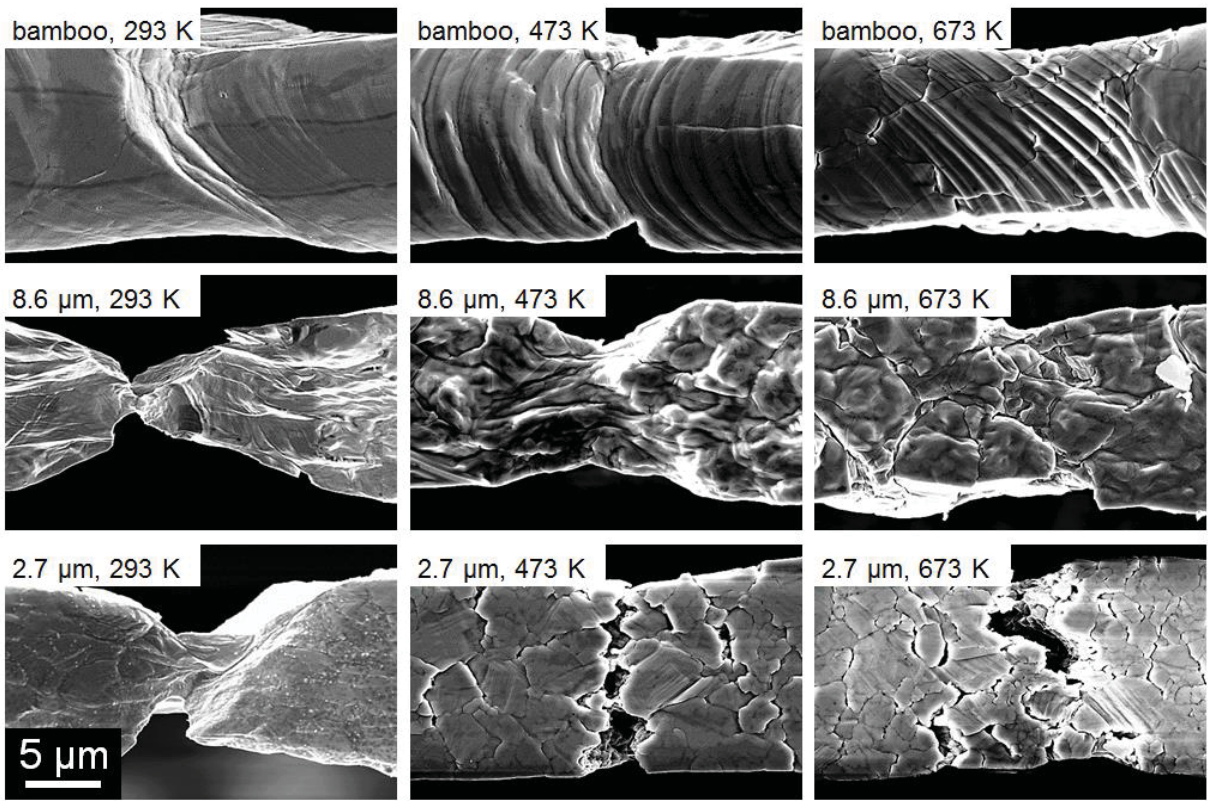

Fig. 3. Post mortem SEM images of the investigated sample types: 1st line bamboo-grained samples, 2nd line 8.6 µm grained samples and 3rd line 2.7 µm grained samples at various temperatures *T*: 1st row 293 K, 2nd row 473 K and 3rd row 673 K. Note, that for the material with 2.7 µm grain size the deformation behavior changes from ductile, intragranular fracture to brittle, intergranular fracture at 473 K and 673 K.

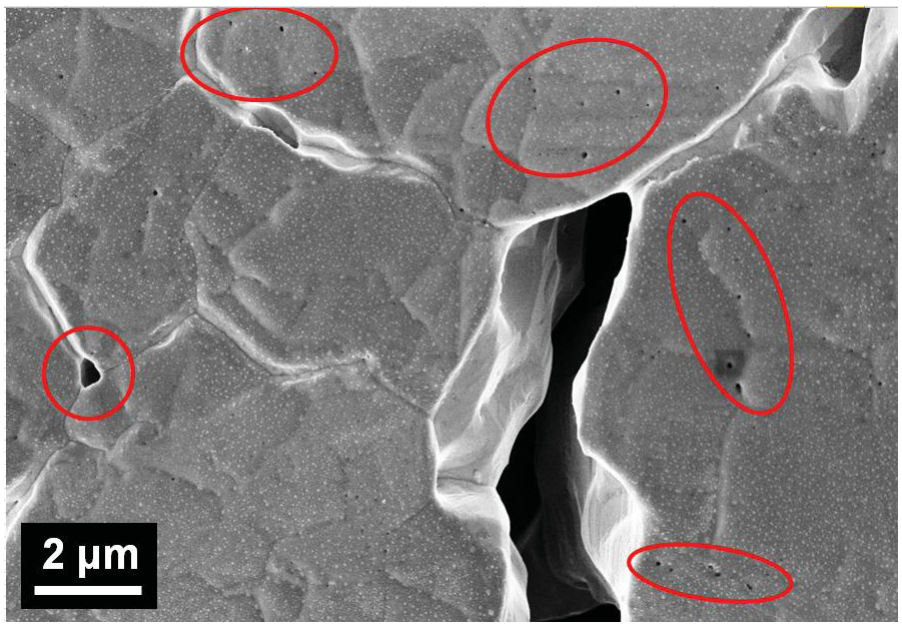

Fig. 4. Fracture appearance of samples with 2.7 µm initial grain size after tensile-testing at 873 K at a strain rate of 0.001 s^{-1}. The deformation is dominated by intergranular cracks and creep pore formation (red circles). Note, that during tensile testing at 873 K grain growth has occurred.

3.2 Temperature dependence of the mechanical response

Overall the σ_{ys} (also the UTS) decreased with increasing temperature and grain size, resulting in the lowest σ_{ys} for the bamboo-grained samples at 673 K (Tab. 1). For the material with a grain size of 2.7 µm a significant decrease in elongation to fracture between 293 K and 473 K was observed (Fig. 5), which is related to segregation of S and Cl to grain boundaries but is not within the focus of this work and reported in details elsewhere [20]. The static tensile tests performed for this material at low temperatures reveal an increase in elongation to fracture, yield strength and UTS with decreasing temperature (Fig. 5, Tab. 1). The influence of the strain rate on the mechanical properties of the 8.6 µm grained samples is demonstrated in Fig. 6 (for a complete set of data see Appendix A). With increasing strain rate there is a tendency for increasing strength. Compared to a previous study [13], the tensile samples with a median grain size of 2.7 µm possess an approximately 10 % smaller cross-section and larger spread of ± 0.6 µm in grain size caused by a different photolithographic production process, resulting in an approx. 10 % lower UTS.

As shown in Fig. 7 the yield strength σ_{ys} was analyzed with respect to temperature for the three different grained materials. By using Eq. 4 and a constant strain rate sensitivity of m = 0.01 [21, 22] apparent activation energies between 47 and 212 kJ/mol have been calculated for the various grain sizes (Tab. 2). Below 293 K for the material with 2.7 µm grain size the apparent activation energy decreases to 55 kJ/mol. Note that for the calculation of the apparent activation energy between 293 and 673 K in total 29 yield strength values and in the range between 143 – 293 K in total 13 yield strength values have been considered. If the two temperature regimes are not separated only one apparent activation energy of Q = 109 ± 20 kJ/mol over the entire temperature range would be calculated.

For the material with 2.7 µm it has to be considered that between 293 K and 473 K embrittlement takes place, where the intragranular-ductile fracture changes to an intergranular-brittle fracture, which could alter the apparent activation energy. Furthermore, above 673 K there is very little remaining plasticity and the observed yield strength is prone to measurement errors, consequently no activation energy for plastic flow has been evaluated. In addition, for testing temperatures above 673 K the samples underwent grain growth during heating and testing. The apparent activation energy of the bamboo-samples is prone to inaccuracies because of the few number of tested samples and the strong scattering in yield strength between the samples.

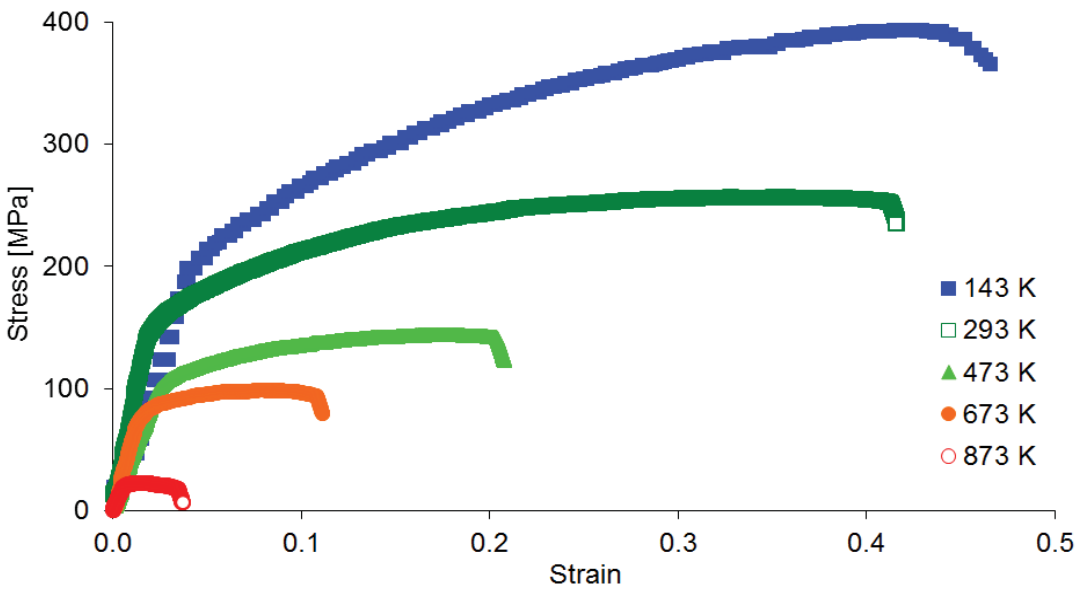

Fig. 5. Stress-strain curves of the material with 2.7 µm grain size at 143 K (blue), 293 K (green), 473 K (lime), 673 K (orange) and 873 K (red). Note, that with increasing temperature the yield strength σ_{ys}, UTS, and elongation to fracture are decreasing. For temperatures exceeding 673 K grain growth occurs. The tensile test at 143 K was performed at a strain rate of 0.01 s^{-1}, all other tests were recorded at a strain rate of 0.001 s^{-1}.

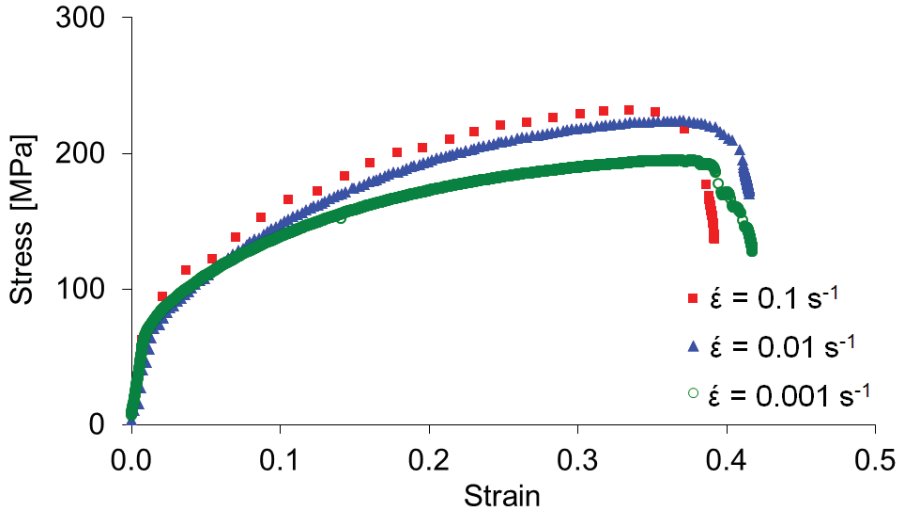

Fig. 6. Stress-strain curves of the material with 8.6 µm grain size at 293 K with a strain rate of 0.1 s^{-1} (red), 0.01 s^{-1} (blue) and 0.001 s^{-1} (green). Note that σ_{ys} and UTS are slightly increasing with increasing strain rate $\dot{\varepsilon}$.

Tab. 1. Yield strength σ_{ys}, UTS and elongation to fracture ε_f obtained from engineering stress-strain measurements as a function of grain size d, temperature T and strain rate $\dot{\varepsilon}$. n gives the number of tested samples. Bamboo stands for samples with a bamboo-like microstructure. Such samples reveal a single-crystalline deformation behavior. Values without an error bar display a single measurement; error bars represent the standard deviations. For temperatures exceeding 673 K the samples showed grain growth during tensile testing, consequently values for the grain size are written in brackets.

d [μm]	T [K]	$\dot{\epsilon}$ [s^{-1}]	σ_{ys} [MPa]	UTS [MPa]	ε_f	n
2.7	143	0.01	201	393	0.46	1
2.7	163	0.01	157	365	0.45	1
2.7	203	0.01	193	364	0.42	1
2.7	223	0.01	186	343	0.5	1
2.7	233	0.01	183	328	0.47	1
2.7	248	0.01	165	323	0.43	1
2.7	293	0.001	142 ± 5	254 ± 6	0.39 ± 0.01	4
2.7	293	0.01	152 ± 6	262 ± 1	0.36 ± 0.01	3
2.7	293	0.1	155 ± 10	270 ± 1	0.45 ± 0.04	3
2.7	373	0.001	140	200	0.32	1
2.7	398	0.001	130 ± 7	189 ± 5	0.27 ± 0.02	2
2.7	398	0.01	135	201	0.27	1
2.7	423	0.001	125	175	0.20	1
2.7	473	0.001	107 ± 5	153 ± 8	0.20 ± 0.06	3
2.7	473	0.01	106 ± 9	156 ± 1	0.28 ± 0.09	3
2.7	473	0.1	115 ± 3	168 ± 7	0.34 ± 0.10	3
2.7	673	0.001	79 ± 13	104 ± 7	0.10 ± 0.03	3
2.7	673	0.01	104 ± 6	133 ± 6	0.19 ± 0.01	3
2.7	673	0.1	104 ± 6	151 ± 19	0.29 ± 0.01	2
(2.7)	773	0.001	68 ± 13	73 ± 9	0.08 ± 0.01	4
(2.7)	873	0.001	19 ± 2	22 ± 3	0.06 ± 0.02	5
8.6	293	0.001	70 ± 1	206 ± 9	0.37 ± 0.05	4
8.6	293	0.01	70 ± 7	222 ± 13	0.39 ± 0.05	4
8.6	293	0.1	73 ± 9	217 ± 11	0.36 ± 0.03	4
8.6	473	0.001	55 ± 6	126 ± 9	0.36 ± 0.05	5
8.6	473	0.01	61 ± 6	143 ± 8	0.34 ± 0.04	5
8.6	473	0.1	71 ± 7	150 ± 7	0.33 ± 0.04	5
8.6	673	0.001	44 ± 8	70 ± 2	0.26 ± 0.06	3
8.6	673	0.01	51 ± 4	92 ± 5	0.39 ± 0.08	4
8.6	673	0.1	61 ± 4	117 ± 5	0.43 ± 0.06	2
10.1	293	0.001	64 ± 10	181 ± 31	0.40 ± 0.06	5
10.1	293	0.01	66 ± 17	205 ± 30	0.39 ± 0.02	3
10.1	293	0.1	89 ± 10	203 ± 22	0.39 ± 0.08	5
10.1	473	0.001	66 ± 7	129 ± 15	0.36 ± 0.05	4
10.1	473	0.01	62 ± 12	149 ± 13	0.38 ± 0.10	6
10.1	473	0.1	87 ± 8	160 ± 14	0.35 ± 0.04	3
10.1	673	0.001	60 ± 7	77 ± 2	0.26 ± 0.07	5
10.1	673	0.01	60 ± 17	96 ± 11	0.34 ± 0.11	5
10.1	673	0.1	44 ± 10	92 ± 11	0.32 ± 0.08	2
bamboo	293	0.001	35	123	0.34	1
bamboo	293	0.01	39 ± 6	131 ± 6	0.35 ± 0.01	2
bamboo	293	0.1	52	134	0.38	1
bamboo	473	0.001	39	88	0.34	1
bamboo	473	0.01	39	88	0.32	1
bamboo	473	0.1	43 ± 6	113 ± 8	0.32 ± 0.03	2
bamboo	673	0.001	27	60	0.27	1
bamboo	673	0.01	42	73	0.19	1

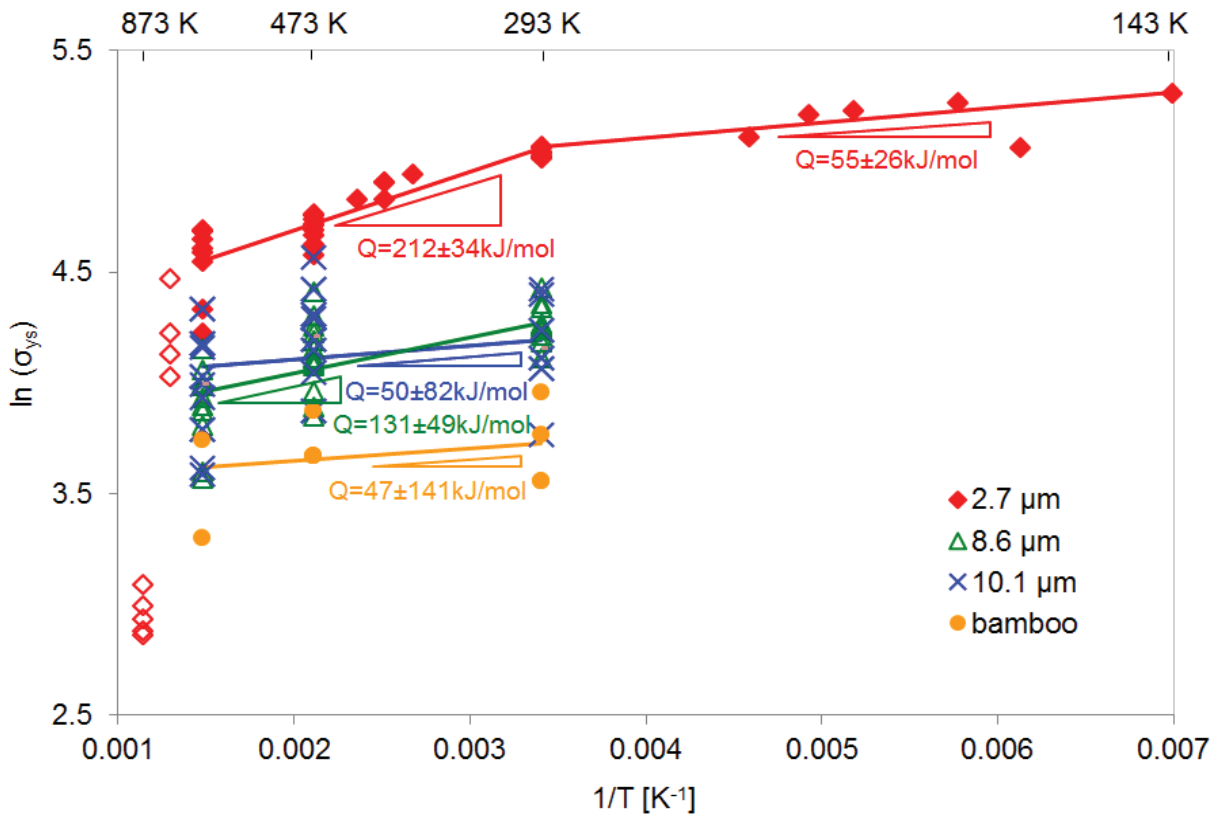

Fig. 7. Yield strength σ_{ys} plotted versus the reciprocal temperature for the 2.7 µm samples (red), 8.6 µm samples (green), 10.1 µm samples (blue) and samples with bamboo-like microstructure (orange). The slope of the curve is a measure of the apparent activation energy *Q*. Yield strength values for the material with 2.7 µm grain size are plotted with open symbols above 673 K and were not considered in calculation of the activation energy as there was a drastic drop in strength preventing to determine a meaningful activation energy. Furthermore, for experiments with a strain rate of 0.001 s^{-1} above 673 K grain growth occurred.

Tab. 2. Apparent activation energy *Q* as a function of the grain size *d* in the temperature range 293 - 673 K. Note that with increasing grain size the activation energy decreases. Values for the bamboo-grained samples are written in brackets because of the high standard deviations due to the stochastic nature of these samples.

d [µm]	*Q* [kJ/mol]	*Q* [eV/atom]
2.7	212 ± 34	2.2 ± 0.4
8.6	131 ± 49	1.4 ± 0.5
10.1	50 ± 82	0.5 ± 0.9
bamboo	(47 ± 141)	(0.5 ± 1.5)

3.3 Local GND analysis by EBSD

In situ like EBSD measurements revealed that the sample's average GND density is increasing from 7.0 ± 3.0 • 10^{13} m^{-2} to 2.1 ± 0.3 • 10^{14} m^{-2} during the tensile test until final fracture (see Fig. 8, black diamonds). The GND density of the deformation zone (= maximum GND density $\rho_{GND,max}$) is increasing from 7.0 ± 3.0 • 10^{13} m^{-2} to 3.7 ± 0.3 • 10^{14} m^{-2} until a strain $\varepsilon \approx 0.285$ is reached (Fig. 8, red rectangles). Assuming, that the plastic strain

$$\varepsilon_{pl} = \rho \bullet b \bullet y \,, \tag{5}$$

with y as the mean free path length of a moving dislocation. In case of coarse-grained, precipitation free metals with primarily dislocation-dislocation interaction it can be argued that

$$y \approx \frac{1}{\sqrt{\rho}} \text{ (i.e. } \rho \approx \frac{1}{y^2}\text{).} \tag{6}$$

which further leads to an square root dependency of the plastic strain and the dislocation density according to Eq. 7.

$$\varepsilon_{pl} = \rho \bullet b \bullet \frac{1}{\sqrt{\rho}} = b \bullet \sqrt{\rho} \,. \tag{7}$$

Even though this estimation is simplified and – for instance – the role of grain boundaries and statistically stored dislocations are neglected completely, the evolution of the analyzed GND density follows this $\Delta\rho_{GND,\max} \sim \varepsilon^2$ trend, as can be seen in Fig. 8 (red curve).

Furthermore, also an estimation of the flow stress with the measured increase in GND density using

$$\Delta\sigma = M \bullet \Delta\tau = M \bullet \alpha_1 \bullet G \bullet b \bullet \sqrt{\Delta\rho_{GND}} \text{ [23],} \tag{8}$$

where M = 3.06 [24] is the Taylor factor, $\alpha_1 \approx 0.3$ a constant, G = 42.1 GPa the shear modulus, and b = 2.56 • 10^{-10} m the Burgers vector, can be made. The maximum GND density increased from 0.7 • 10^{14} m^{-2} at ε = 0 to 3.7 • 10^{14} m^{-2} at $\varepsilon \approx 0.285$ (Fig. 8), which results in an expected $\Delta\sigma$ of 172 MPa. The measured global true stress increases from σ_{ys} = 24 MPa to σ = 153 MPa at ε ≈ 0.285, corresponding to an increase in flow stress of approximately 129 MPa, which is in a comparable range to the calculated local $\Delta\sigma$ of 172 MPa. If the average dislocation density $\rho_{GND,av}$ is used for calculation of the increase in flow stress instead of the maximum GND density $\rho_{GND,max}$, there is also a good accordance with the evolution of the true stress (Fig. 8 and Appendix B).

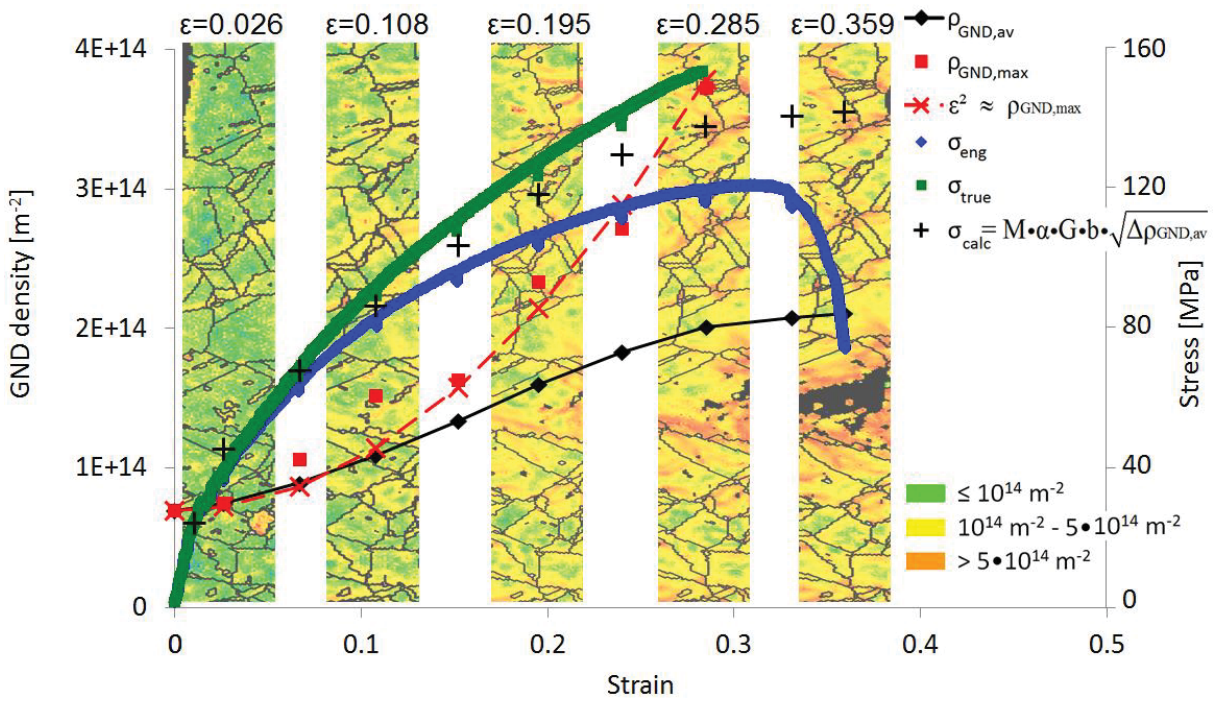

Fig. 8. Evolution of the average GND density $\rho_{GND,av}$, maximum local GND density $\rho_{GND,max}$, engineering, true and calculated stress (σ_{eng}, σ_{true} and σ_{calc}) plotted against the strain of an annealed (5h, 1073 K) sample with 15.9 µm grain size and a partially bamboo-like microstructure. The SEM/EBSD images taken at different strains (see inset) illustrate the local GND density evolution during straining. Note that the maximum local GND density $\rho_{GND,max}$ is reached at a strain of 0.285. Because of strong necking and roughening of the surface during the experiment it was not possible to obtain reliable values for $\rho_{GND,max}$ above a strain of 0.285, however below this value the GND density $\rho_{GND,max}$ follows an ε^2 dependency (red crosses).

3.4 Temperature dependent cyclic tension-tension experiments

At 293 K the yield strength, UTS and number of cycles to failure increase with decreasing grain size, while at 473 K the strength increasing effect of a small grain size on σ_{ys}, UTS and N becomes smaller. At 673 K the sample with the smallest grain size has static mechanical properties comparable to that of samples with 10.1 µm grain size, however the samples with 2.7 µm grain size show the lowest lifetime in the cyclic tension-tension experiments. In the present case this is caused by embrittlement of grain boundaries, which also eliminates the strength increasing effect of the Hall-Petch effect of smaller grains at elevated temperatures during cyclic testing.

Independent of the grain size and temperature it has been found, that with decreasing maximum stress σ_{max} the lifetime (number of cycles N) is increasing (Fig. 9). If the maximum stress σ is plotted versus the number of cycles N in a log-log

plot a linear relationship is observed. Furthermore, the slope of the curve is slightly increasing with increasing temperature. In a recent work [13] it was demonstrated, that the stress-lifetime relationship at room temperature can be described by a modified Basquin relation. In this study again it is shown, that the intersections of the stress-lifetime curves with the ordinate corresponds to the modified fatigue stress coefficient σ_f'' and the slope of the curves to the modified fatigue stress exponent b' (Fig. 9, Tab. 3). Although the samples with 2.7 µm grain size show the highest UTS, they also reveal the steepest slope at all temperatures. This indicates that for applications exceeding the low cycle fatigue regime the samples with 2.7 µm grain size have the lowest cyclic strength σ_{max}.

Tab. 3. Parameters for description of the stress-lifetime (*S-N*) relationship depending on temperature and grain size *d*. Note that the modified fatigue stress exponent *b'*, describing the slope of the *S-N* curve, increases with temperature.

d [µm]		293 K	473 K	673 K
2.7	σ_f'' [MPa]	295 ± 5 [13]	165 ± 5	95 ± 5
	b'	0.03 ± 0.02 [13]	0.09 ± 0.03	0.19 ± 0.04
8.6	σ_f'' [MPa]	196 ± 19 [13]	130 ± 15	75 ± 15
	b'	0.02 ± 0.01 [13]	0.03 ± 0.02	0.07 ± 0.05
10.1	σ_f'' [MPa]	177 ± 15 (13.5 µm, [13])	120 ± 15	70 ± 15
	b'	0.01 ± 0.02 (13.5 µm, [13])	0.05 ± 0.03	0.07 ± 0.03

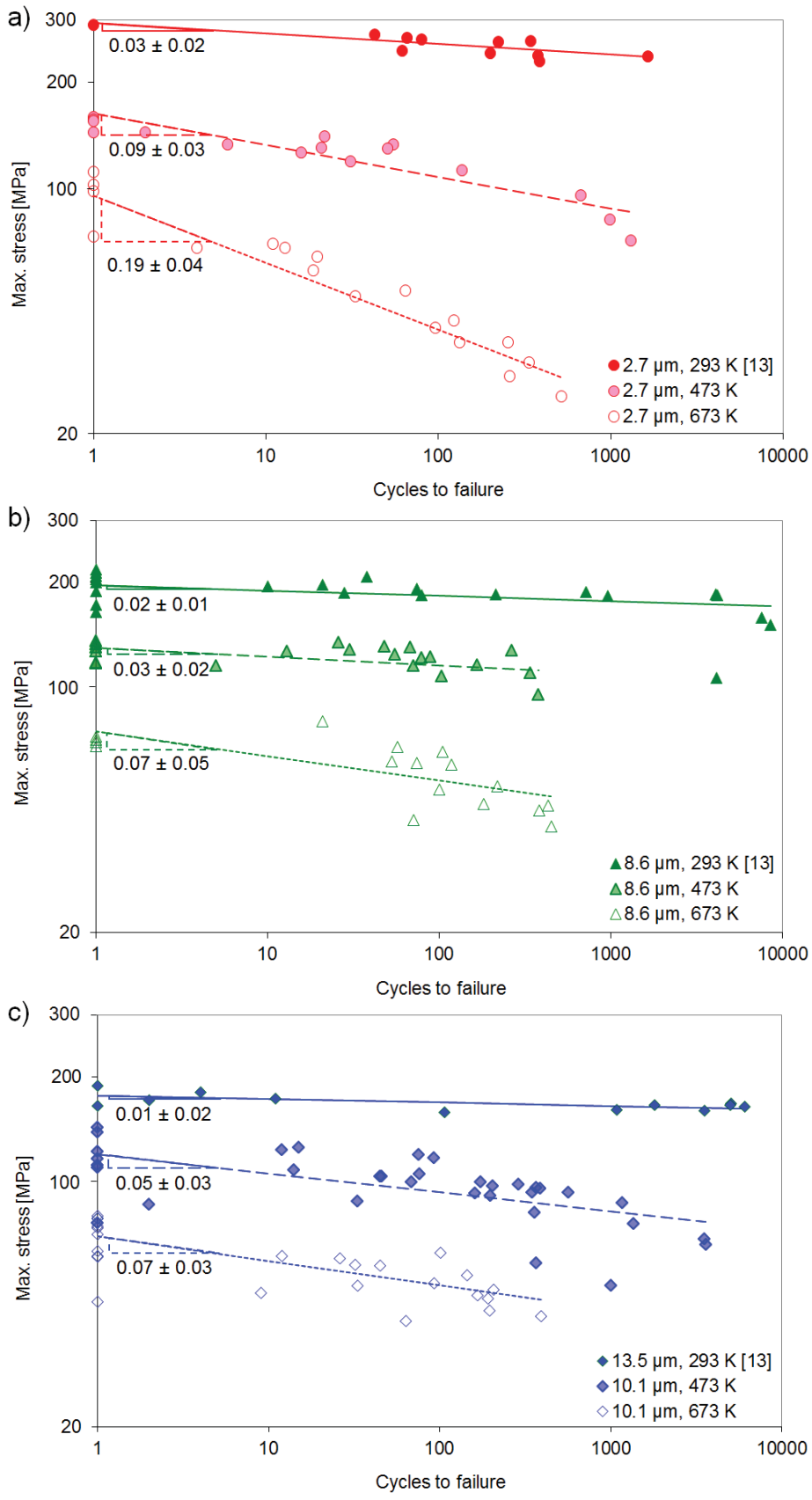

Fig. 9. Stress over cycles to failure for (a) Cu with 2.7 µm grain size (red), (b) Cu with 8.6 µm grain size (green) and (c) Cu with 10.1 µm grain size (blue). The number of cycles to failure increases with decreasing maximum stress and decreasing temperature. The 95 % confidence interval of the fitted slope is attached.

4 Discussion

4.1 Deformation behavior

At room temperature all materials show a ductile behavior independent of grain size and the number of cycles to failure (Fig. 3, left). In case of the finest grain size bulk-like behavior with extensive elongation before necking and small scatter of the mechanical response was found. In contrast, the 10.1 µm and bamboo-grained samples show necking starting right after yield and the deformation by individual grains dominates the deformation. Both match the previous observations [6, 11, 12] of a critical D : d ratio of 5. This observation holds true for static experiments and cyclic experiments. Especially in the material with bamboo-like microstructure slip steps are dominating the surface of the post mortem sample, indicating a deformation dominated by dislocation based plasticity between 293 and 673 K. The material with 8.6 µm grain size shows also a ductile behavior at elevated temperatures, due to the smaller grain size glide steps are not as clearly visible as in the samples with bamboo-like microstructure. Finally, the material with 2.7 µm sized grains exhibits an embrittlement of the grain boundaries and failure along them at elevated temperatures, especially at low strain rates of 0.001 s^{-1} (Fig. 3, also see Fig. A3 in Appendix). At 873 K (Fig. 4) the deformation is dominated by diffusion and creep pore formation along grain boundaries accompanied by grain growth during testing. The change of the deformation mechanism between 293 and 473 K was also confirmed by a change of the observed apparent activation energy and will be discussed later.

4.2 Temperature dependent tensile tests

It has been shown, that the strength of the material (σ_{ys} and UTS) is increasing with decreasing temperature, decreasing grain size and increasing strain rate, which can be explained by the thermal activation of deformation [25 - 27], the Hall–Petch effect [28, 29], and strain rate sensitivity of materials [30]. This has been reported in early works [e.g. 31], but also in more recent studies [21, 32 - 34].

The activation energy, which was obtained by analysis of the temperature dependence of the yield strength at 0.2 % plastic strain, increases from 50 ± 82 kJ/mol

for the Cu samples with 10.1 µm grain size to 212 ± 34 kJ/mol for those with 2.7 µm grain size. It has to be considered, that the apparent activation energy strongly depends on the used value for the strain rate sensitivity *m*, consequently the values for the activation energy *Q* should be seen as a tendency. However, for all samples the same value of m was used as from literature only a slight increase of m is expected between 293 and 473 K [31]. Furthermore the experiments in this study reveal no changes of *m* in the analyzed temperature and grain size regime. Consequently a qualitative comparison between the obtained values for *Q* is feasible. The activation energy for grain boundary diffusion in Cu is decreasing with increasing purity (standard purity 99.99 % Cu: 104 kJ/mol [35], high-purity 99.999 % Cu: 84.75 kJ/mol and highest-purity 99.9998 % Cu: 72.47 kJ/mol [36]), the activation energy for lattice self-diffusion in Cu is approximately 200 kJ/mol [37]. For cross-slip, the dominating process during dislocation multiplication and strain hardening, in Cu thin films activation energies of 30 - 64 kJ/mol, depending on which kind of lock is formed, were observed [38]. In creep experiments performed at 550 – 1025 K on bulk Cu activation energies of 100 - 200 kJ/mol, dependent on the creep rate and temperature, were found at a stress level of 75 MPa. In these creep experiments lattice self-diffusion and non-conservative motion of jogs have been identified as the most probable deformation mechanism [39].

Cross-slip, intersection of dislocations and strain hardening coincide well with the measured apparent activation energies of 47 - 50 kJ/mol as obtained for bamboo-grained and 10.1 µm median grain sized samples independent of temperature and for the 2.7 µm median grain sized samples up to 293 K. This matches well with the post mortem SEM images presented in Fig. 8 showing deformation features typically observed in materials deforming via dislocation plasticity. At higher temperatures it is hard to identify individual slip steps in the 2.7 µm and 8.6 µm grain sized samples. The comparable higher apparent activation energies of 131 – 212 kJ/mol (see. Fig. 7) in these samples compared to 47 – 50 kJ/mol in the bamboo-like samples suggest the activation of grain boundary diffusion and/or dislocation climb.

To confirm whether a strain-rate sensitivity value of m = 0.01 as reported in literature [21] can be used to calculate the activation energies independent strain-rate tests have been performed in this study. The strain-rate-sensitivity has been only analyzed for the samples with 2.7 µm grain size, as for the materials with a larger

grain size there was a strong scatter of the flow strength due to the relatively small number of grains in the sample volumes leading to statistical variations (see Fig. A1 in Appendix A).

The flow stress at 0.2 % plastic strain (σ_{ys}) and 10 % total strain ($\sigma_{0.1}$) was analyzed as a function of strain rate $\dot{\varepsilon}$. By plotting log σ against log $\dot{\varepsilon}$ the slope of the curve corresponds to the strain rate sensitivity *m*. Both, for a plastic strain of 0.2 % and a total strain of 10 % strain-rate-sensitivities of ≈ 0.010 ± 0.003 were observed (Fig. 10) in agreement with the value from literature [21].

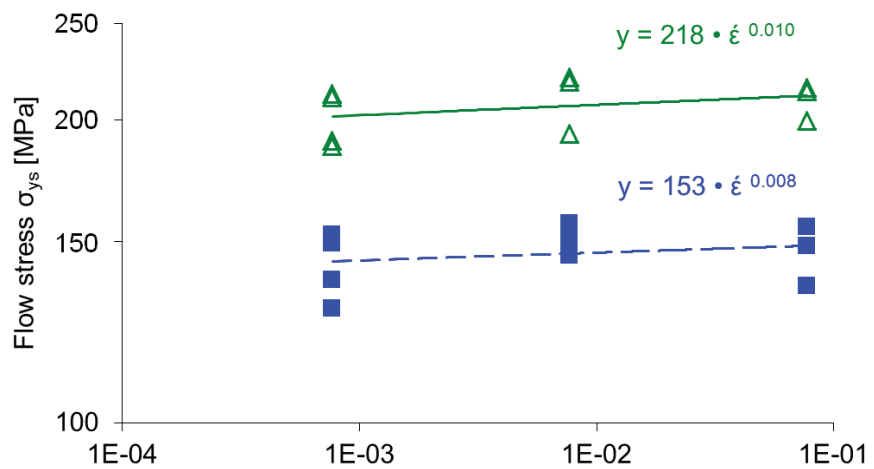

Fig. 10. Log-Log plot of σ versus $\dot{\varepsilon}$. The dashed blue curve corresponds to a plastic strain ε of 0.002, the continuous green curve to a total strain of 0.1. The slope of the curve provides the strain rate sensitivity *m*. The increase of the pre-exponential coefficient from 153 MPa to 218 MPa is caused by strain hardening.

The dislocation density can be used to approximate the activation volume [40] based on the geometrical definition of the activation volume where dislocation interactions are assumed – in that case the dislocation density ρ is:

$$\rho \approx \frac{1}{\lambda^{*2}}, \tag{9}$$

where λ^* [m^{-2}] is the upper limit for the dislocation segment length with

$$\lambda^* = \frac{V^*}{b^2}, \tag{10}$$

and consequently the activation volume:

$$V^* \approx \frac{b^2}{\sqrt{\rho}}, \tag{11}$$

where $b = 2.56 \cdot 10^{-10}$ m is the Burgers vector. *In situ* like EBSD measurements have shown a maximum GND density in the necking zone of $3.7 \pm 0.3 \cdot 10^{14}$ m^{-2}, which

would correspond to an apparent activation volume of 200 b^3. Since statistically stored dislocations (SSDs) have not been considered for this first approximation the presented apparent activation volume is an upper bound [41]. However, with increasing strain SSDs become more important and can finally dominate the deformation behavior.

EBSD measurements on the undeformed samples have shown an initial GND density of $< 7 \pm 3 \cdot 10^{13}$, corresponding to a lower limit for V^* of 470 b^3. This is in a comparable range to the activation volumes obtained by the approximation using the activation energy (Tab. 4). Furthermore a comparable dislocation density has been reported for Cu thin films on substrates [42 - 44].

Other studies on Cu thin films obtained activation volumes ranging from 60 b^3 (80 nm thin film [45]) to 2,384 b^3 (25 µm thin film [46]) at room temperature. In micro-indentation experiments a value of 1,000 b^3 was found for 99.999 % bulk Cu for large indentation depths [47]. Bulk Cu with an initial grain size of 60 µm revealed an activation volume of < 300 b^3, measured at 293 K in a strain rate change test by torsion [48]. For macro-sized 99.99 % Cu samples with a grain size of 36 µm activation volumes of 2,100 b^3 in creep experiments and 1,400 b^3 in tensile experiments were found at 300 K [49].

Differences in activation volume are mainly caused by different extrinsic (geometric) and intrinsic (e.g. grain size) sample dimensions. It is observed, that the apparent activation volume increases with the film thickness, as reported for silver thin films [50] and aluminum thin films [51]. Consequently, bulk materials can show a significant higher activation volume than thin films [52 - 55]. Furthermore, the obtained activation volumes depend on the mode of the experiment: For relaxation experiments the obtained values are larger than in strain-rate-jump tests [56].

Finally, also the strain-rate sensitivity m can be used to estimate the activation volume [22, 57]:

$$V^* = \frac{\sqrt{3}kT}{m\sigma}, \tag{12}$$

whereby $k = 1.38 \cdot 10^{-23}$ J/K the Boltzmann's constant, T [K] the temperature, m the strain-rate-sensitivity and σ [MPa] the flow stress of the deformation zone. For $m = 0.010$ and $T = 293$ K an apparent activation volume V^* of 290 b^3 (2.7 µm grain size) was determined. During the experiment the activation volume decreases to 80 b^3

(2.7 µm grain size) when the UTS is reached, which is in good accordance with the observed increase in dislocation density with increasing strain (Fig. 8).

However, in other works [58] instead of the factor $\sqrt{3}$ the Taylor factor $M = 3.06$ [24], is used, resulting in an apparent activation volume $V^* = 510\ b^3$ at σ_{ys} and $V^* = 150\ b^3$ when the stress reaches the UTS. Independent whether $\sqrt{3}$ or M is used, V^* is in a comparable range to V^* calculated from the dislocation density and with results from mechanical threshold stress (MTS) models [59]. For fcc metals a V^* of 10^2 - 10^3 b^3 is expected for forest dislocation interaction [60], which points towards the same deformation mechanism as deduced from the activation energy.

Tab. 4. Apparent activation energy Q, calculated apparent activation volume $V^* = \frac{\sqrt{3}kT}{m\sigma}$, GND density from *in situ* like EBSD measurements and therefrom calculated apparent activation volume $V^* = \frac{b^2}{\sqrt{\rho_{GND,\max}}}$ at 293 K as a function of the grain size d and the true stress level (considering the cross-section reduction in the necking zone for σ_{UTS}^{true}). Values marked with $^+$ are based on an assumed strain rate sensitivity of 0.01. The activation energy for the bamboo-grained samples is reported in brackets because of the high measuring uncertainty.

d [µm]	Q [kJ/mol]	$V^* = \frac{\sqrt{3}kT}{m\sigma}$ [b³]		$\rho_{GND,max}$ [m^{-2}]	$V^* = \frac{b^2}{\sqrt{\rho_{GND,\max}}}$ [b³]
		$\sigma = \sigma_{ys}$	$\sigma = \sigma_{UTS}^{true}$		
2.7	212 ± 34	290	80	$6.5 \pm 0.3 \cdot 10^{14}$	150
8.6	131 ± 49$^+$	300$^+$	100$^+$	-	-
10.1	50 ± 82$^+$	650$^+$	110$^+$	$5.5 \pm 0.3 \cdot 10^{14}$	170
15.9	(47 ± 141)$^+$	1670$^+$	140$^+$	$3.7 \pm 0.3 \cdot 10^{14}$	200

4.3 Temperature dependent cyclic tension-tension experiments

In this study it has been shown, that also at elevated temperatures the number of cycles to failure in ratcheting experiments is determined by the ratio of elongation to fracture, ε_f, to creep strain per cycle, $\Delta\varepsilon_{cr}$, ratio (Fig. 11), which has been recently shown for experiments at 293 K [13]:

$$N \approx \frac{\varepsilon_f - \varepsilon_{pl1} - \varepsilon_{pl2}}{\Delta\varepsilon_{cr}}, \qquad (13)$$

where $\varepsilon_f - \varepsilon_{pl1} - \varepsilon_{pl2} = \Delta\varepsilon_{cum}$. ε_{pl1} is the deformation until the first unloading cycle and ε_{pl2} the deformation after the last loading cycle. The elongation to fracture as well as the fracture appearance are independent of the mode of experiment, regardless if it is a static tensile or a ratcheting experiment.

At elevated temperatures ($T \geq 473$ K) there are no significant differences in ε_f between the samples with 8.6 and 10.1 µm grain size, however due to grain boundary embrittlement a reduction of ε_f is observed for the samples with 2.7 µm grain size. At 293 K $\Delta\varepsilon_{cum}$ is in good accordance with the observed values of Yang et al. on Cu wires with 30 and 50 µm diameter and 12 and 20.5 µm sized grains, where $\Delta\varepsilon_{cum}$ was approximately 10 % [16]. A value of 9.43 % for the final monotonic plastic strain was also found in high-cycle ratcheting experiments (10^4 – 10^7 cycles to failure, mean stress > 0) for 12 µm thick, 500 µm wide and 5 mm long electrodeposited, freestanding Cu thin film samples [61].

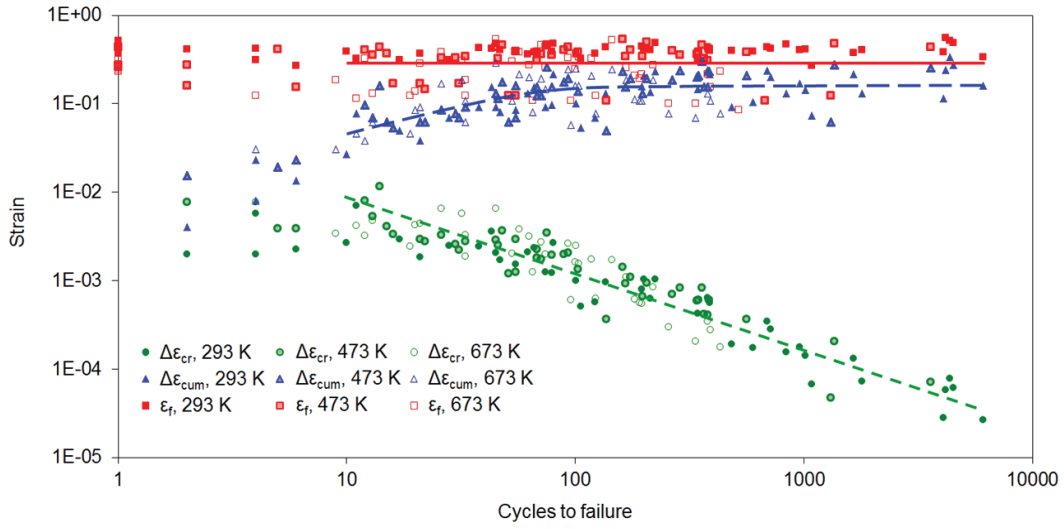

Fig. 11. Elongation to fracture ε_f (red), cumulative creep strain $\Delta\varepsilon_{cum}$ (blue) and creep strain per cycle $\Delta\varepsilon_{cr}$ (green). Note that strain values below 10 cycles are prone to inaccuracies because of high static creep during holding time at the maximum stress, consequently lines for the strain start at $N = 10$. Values at 293 K are from [13].

5 Summary and conclusions

Static and cyclic tension-tension experiments at variable temperatures have been used to identify the deformation mechanism in micron sized, polycrystalline copper lines. The evolution of the yield strength, which is decreasing significantly with increasing temperature, was used to calculate the activation energy. The obtained

apparent activation energies of approximately 50 kJ/mol for the 10.1 µm and bamboo-grained samples and complementary SEM images indicate that dislocation-dislocation interactions, forest hardening and cross-slip are the strength controlling mechanisms between 293 and 673 K. This is in good accordance with the obtained GND densities and thereof calculated apparent activation volumes. Below 293 K dislocation-dislocation interactions, forest hardening and cross-slip are the dominating deformation mechanisms also for the 2.7 µm grained samples. However, for the samples with 2.7 and 8.6 µm grain size with apparent activation energies between 131 and 212 kJ/mol the non-conservative motion of jogs, grain-boundary and lattice diffusion are the main deformation mechanisms between 293 and 673 K.

Stress-lifetime curves have been obtained during cyclic testing, allowing a lifetime prediction based on grain size, temperature and stress level. While at room temperature both for static and cyclic experiments a small grain size is favorable, the optimum grain size for a high dynamic strength increases with temperature. Strain-lifetime curves indicate that the number of cycles to failure is independent of temperature and grain size. The lifetime is mainly dominated by the creep strain per cycle. However, there is still a tendency for a lower elongation to fracture at elevated temperatures. In the case of the material with 2.7 µm grain size this is caused by embrittlement of the grain boundaries. In addition to the strain-lifetime curves, where the elongation to fracture is independent of the number of cycles to fracture, also SEM observations have shown a deformation behavior comparable to a tensile test. This is in contrast to cyclic bending experiments, which normally show typical fatigue deformation microstructures such as extrusions and intrusions due to alternating tensile and compressive stresses.

Acknowledgement

Part of this work was jointly funded by the Austrian Research Promotion Agency (FFG, Project No. 831163) and the Carinthian Economic Promotion Fund (KWF, contract KWF-1521|22741|34186). The authors want to thank J. Fugger. Thanks for technical assistance is expressed to M. Augustin, H. Felber, R. Grilz, H. Groß, F. Hubner, M. Krug, R. Leuschner, C. Lindner, K. Matoy, S. Modritsch, T. Ostermann, G. Reiter, H. Schönherr and K. Schrettlinger.

References

1 E Glickman, M Molotskii, Materials Lett. 26, (1996), 65-68.

2 PJ Henderson, SKB technical report 92-04.

3 WD Nix, Metallurgical Transactions A 20, 11, (1989), 2217-2245.

4 GW Nieman, JR Weertman, RW Siegel, Scripta Metall. 23, 12, (1989), 2013-2018.

5 X.Z Liao, YH Zhao, YT Zhu, RZ Valiev, DV Gunderov, J. Appl. Phys. 96, 1, (2004), 636-640.

6 B Yang, C Motz, M Rester, G Dehm, Phil. Mag. 92, 25-27, (2012), 3243-3256.

7 DT Read, Int. J. Fatigue 20, 3, (1998), 203-209.

8 S Hong, R Weil, Thin Solid Films 283, 1-2, (1996), 175-181.

9 N Murata, K Tamakawa, K Suzuki, H Miura, International Conference on Electronic Materials and Packaging, EMAP 2008, (2008).

10 R Hofbeck, K Hausmann, B Ilschner, HU Kunzi, Scripta Metall. 20, 11, (1986), 1601-1605.

11 XW Gu, CN Loynachan, Z Wu, YW Zhang, DJ Srolovitz, JR Greer, Nano Lett. 12, (2012), 6385-6392.

12 DC Jang, JR Greer, Scr. Mater. 64, (2011), 77.

13 A Wimmer, A Leitner, T Detzel, W Robl, W Heinz, R Pippan, G Dehm, Acta Mater. 67, (2014), 297-307.

14 M Smolka, C Motz, T Detzel, W Robl, T Griesser, A Wimmer, G Dehm, Rev. Sci. Instrum. 83, 6, (2012), 064702.

15 B Yang, C Motz, W Grosinger, W Kammrath, G Dehm, Int. J. Mater. Res. 99, (2008), 716-724.

16 B Yang, C Motz, W Grosinger, G Dehm, Mat. Sci. Eng. A 515, (2009), 71-78.

17 C Kirchlechner, J Keckes, JS Micha, G Dehm, Adv. Eng. Mat. 13, 8, (2011), 837-844.

18 LP Kubin, A Mortensen, Scripta Mater. 48, (2003), 119-125.

19 A Smolej, B Skaza, M Fazarinc, RMZ – Materials and Geoenvironment 56, 4, (2009), 389-399.

20 A Wimmer, M Smolka, W Heinz, T Detzel, W Robl, C Motz, V Eyert, E. Wimmer, F Jahnel, R Treichler, G Dehm, submitted to Mat. Sci. Eng. A.

21 M Dao, L Lu, YF Shen, S Suresh, Acta Mater. 54, (2006), 5421-5432.

22 J Chen, L Lu, K Lu, Scripta Mater. 54, (2006), 1913-1918.

23 N Hansen, Mat. Sci.and Eng. A 409, (2005), 39-45.

24 RE Stoller, SJ Zinkle, J. Nucl. Mater. 283-287, (2000), 349-352.

25 UF Kocks, Encyclopedia of Materials: Science and Technology, (2001), 7084-7088.

26 PW Osborne, Acta Metall. 11, 8, (1963), 998-999.

27 UF Kocks, H Mecking, Prog. in Mat. Sci. 48, (2003), 171-273.

28 EO Hall, Proc. Roy. Soc. B 64, (1951), 747-753.

29 NJ Petch, J. Iron Steel 174, (1953), 25-28.

30 H Huh, K Ahn, JH Lim, HW Kim, LJ Park, J. of Mat. Proc. Techn. 214, 7, (2014), 1326-1340.

31 RP Carreker, WR Hibbard, Acta Metall. 1, (1953), 654-663.

32 T Suo, Y Li, F Zhao, X Fan, W Guo, Mech. of Mater. 61, (2013), 1-10.

33 JY Zhang, G Liu, J Sun, Int. J. of Plast. 50, (2013), 1-17.

34 L Lu, R Schwaiger, ZW Shan, M Dao, K Lu, S Suresh, Acta Mater. 53, (2005), 2169-2179.

35 HJ Frost, MF Ashby, Deformation-mechanism maps, Pergamon Press, Oxford, (1982).

36 T Surholt, C Herzig, Acta Mater. 45, 9, (1997), 3817-3823.

37 DB Butrymowicz, JR Manning, ME Read, J. Phys. Chem. Ref. Data 2, 3 (1973), 643-648.

38 SI Rao, DM Dimiduk, TA Parthasarathy, J El-Awady, C Woodward, MD Uchic, Acta Mater. 59, (2011), 7135-7144.

39 M Pahutova, J Cadek, P. Rys, Phil. Mag. 23, 183, (1971), 509-517.

40 D Weiss, PhD-Thesis, University of Stuttgart, (2000).

41 NA Fleck, GM Muller, MF Ashby, JW Hutchinson, Acta Metall. Mater. 42, 2, (1994), 475-487.

42 A Gangulee, J. Appl. Phys. 43, (1972), 867-873.

43 S Sen, SK Halder, SP Sen Gupta, J. Phys.D: Appl. Phys. 8, (1975), 1709-1721.

44 RM Keller, SP Baker, E Arzt, Acta Mater. 47, (1999), 415.

45 II Solonovich, Fizika Metallov i Metallovedenie 40, 3, (1975), 633-7.

46 AI Il'inski, LS Palatnik, GY Lakh, TA Nguen, Fizika Metallov i Metallovedenie 38, 1, (1974), 217-219.

47 RJ Klassen, BJ Diak, S Saimoto, Mat. Sci. Eng. A 387–389, (2004), 297-301.

48 M Zehetbauer, V Seumer, Acta Metall. Mater. 41, 2, (1993), 577-588.

49 RP Reed, NJ Simon, RP Walsh, Mat. Sci. Eng. A 147, (1991), 23-32.

50 MJ Kobrinsky, CV Thompson, Acta Mater. 48, (2000), 625-633.

51 W Heinz, PhD-Thesis, University of Leoben, (2010).

52 AS Argon, GH East, Proc. of the 5th Int. Conf. on the Strength of Metals and Alloys 1, (1979), 9.

53 H Conrad, WD Cao, in Proc. of the Johannes Weertman Symposium, The Minerals, Metals & Materials Society, (1996), 321.

54 YVRK Prasad, DH Sastry, KI Vasu, J. Mater. Sci. 5, (1970), 495.

55 ME Kassner, AK Mukherjee, Scripta Metall. 17, (1983), 741-744.

56 UF Kocks, AS Argon, MF Ashby, Prog. Mater. Sci. 19, (1975), 26.

57 RJ Asaro, S Suresh, Acta Mater. 52, (2005), 3369-3392.

58 FH Dalla Torre, EV Pereloma, CHJ Davies, Scripta Mater. 51, (2004), 367-371.

59 MC Cai, LS Niu, XF Ma, HJ Shi, Mech. of Mater. 42, (2010), 774-781.

60 MA Meyers, A Mishra, DJ Benson, Prog. in Mat. Sci. 51, (2006), 427-556.

61 Y Hwangbo, JH Song, Int. J. of Fat. 38, (2012), 1-6.

62 PJ Imrich, C Kirchlechner, C Motz, G Dehm, Acta Mater. 73, (2014), 240-250.

Appendix

In Appendix A all performed tensile tests are shown. The grain size was 10.1, 8.6 and 2.7 μm, the strain rate 0.001 s^{-1}, 0.01 s^{-1} and 0.1 s^{-1} and the temperature ranges from 293 to 673 K. Note that for the material with 2.7 μm grain size the elongation to fracture ε_f increases with increasing loading speed at 473 and 673 K.

Appendix B shows the results of tensile tests performed *in situ* inside the SEM with EBSD for different grained materials.

Appendix A

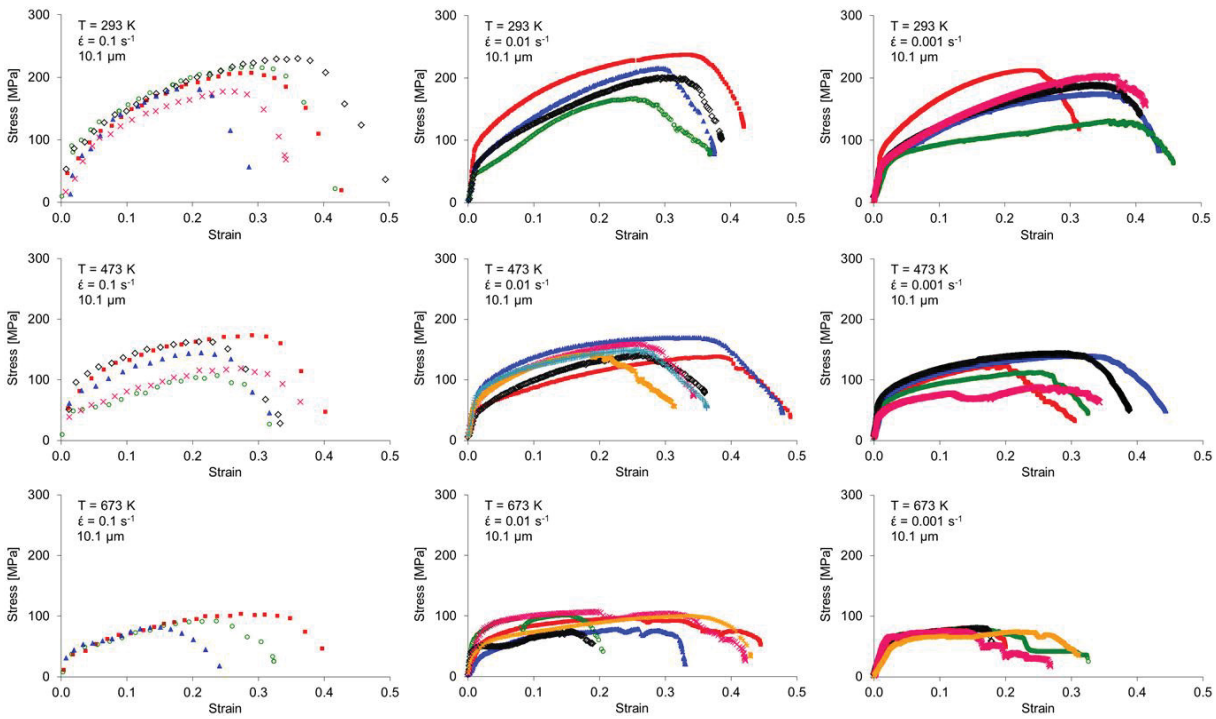

Fig. A1. Stress-strain curves of the samples with 10.1 μm grain size

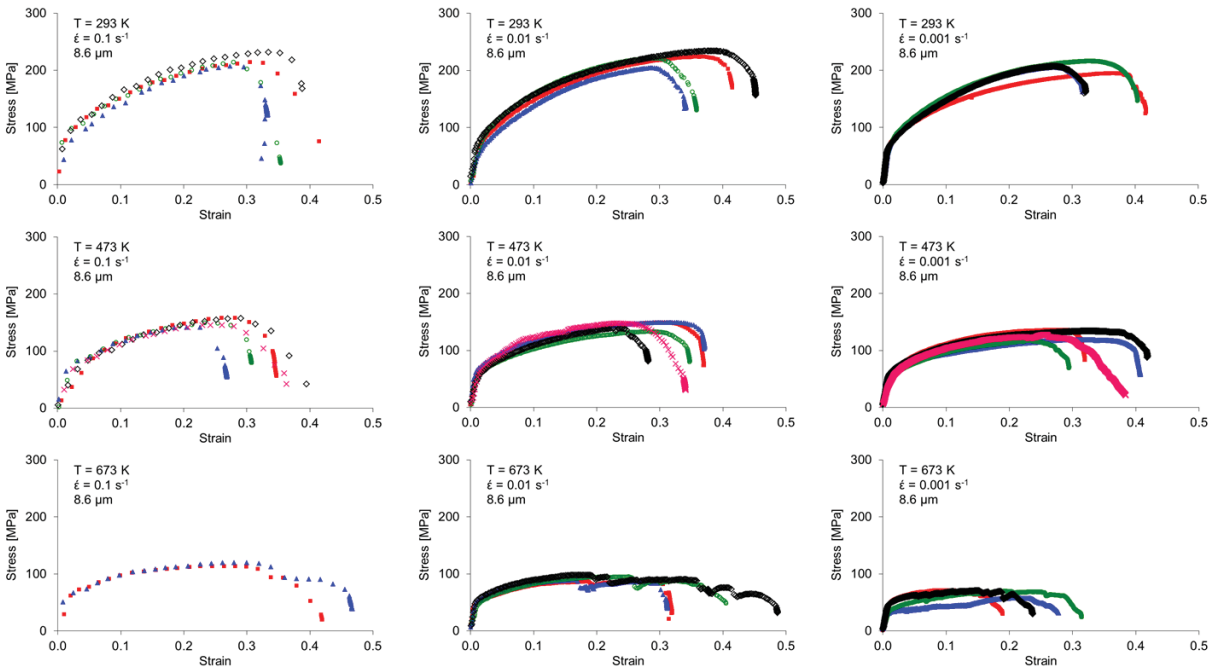

Fig. A2. Stress-strain curves of the samples with 8.6 μm grain size

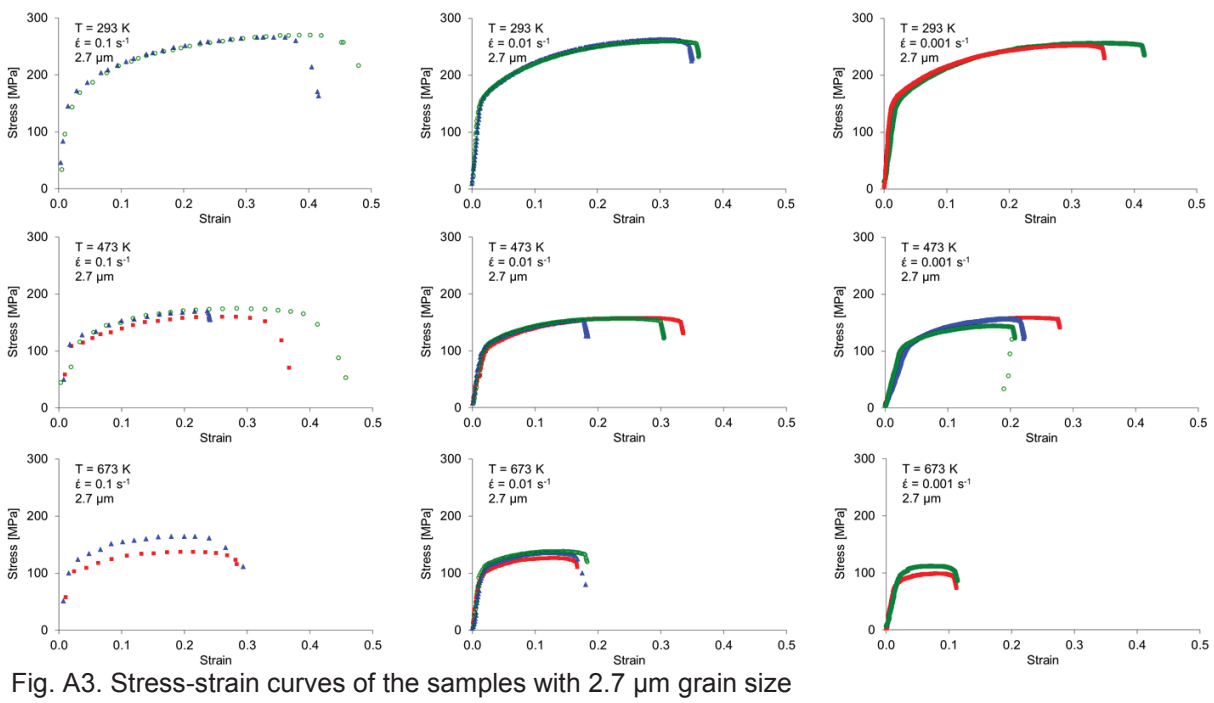

Fig. A3. Stress-strain curves of the samples with 2.7 μm grain size

Appendix B

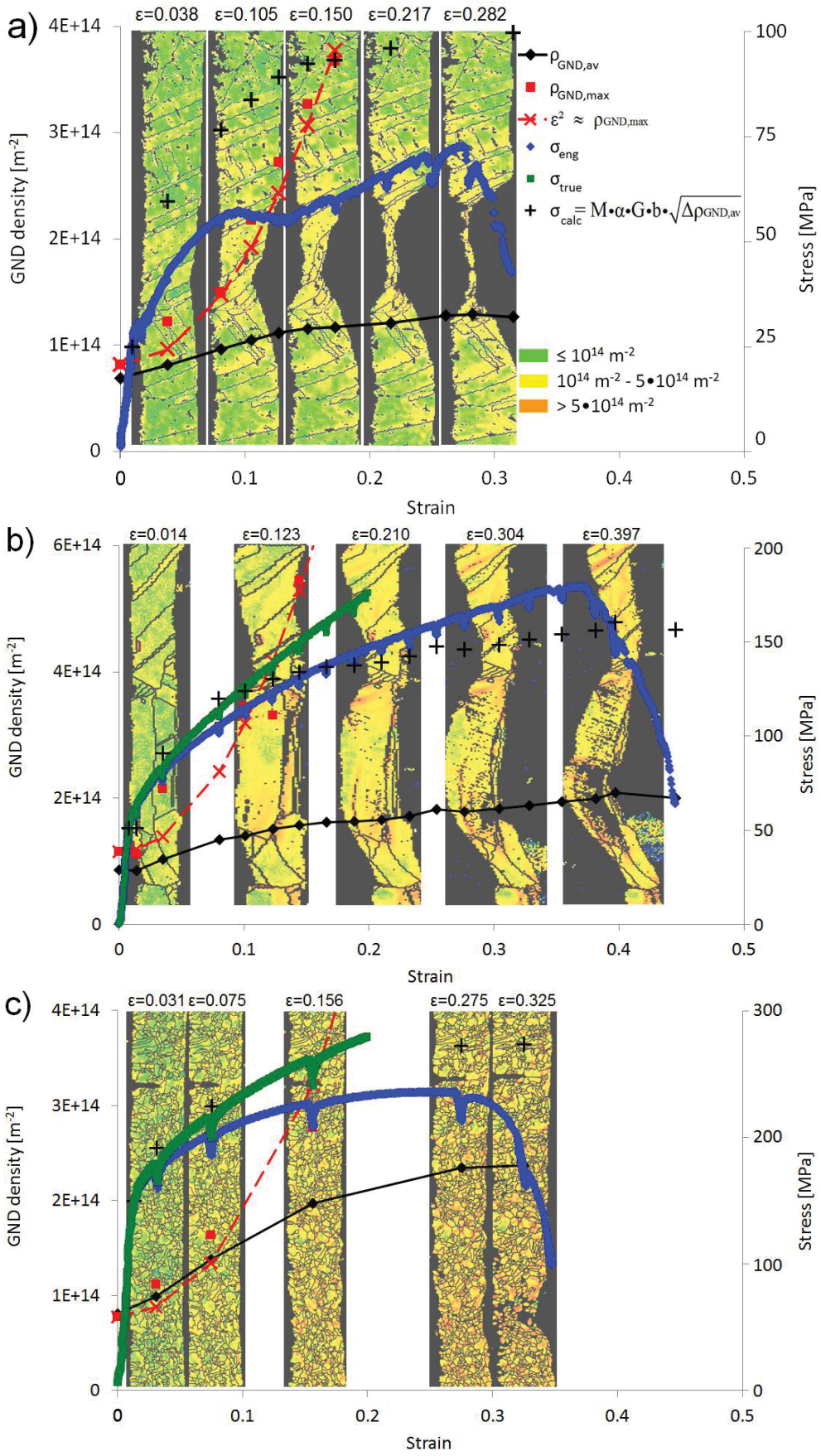

Fig. B1. Evolution of the average GND density $\rho_{GND,av}$, maximum local GND density $\rho_{GND,max}$, engineering, true and calculated stress (σ_{eng}, σ_{true} and σ_{calc}) plotted against the strain. The

SEM/EBSD images taken at different strains (see inset) illustrate the local GND density evolution during straining. Note that the maximum local GND density $\rho_{GND,max}$ is reached at a strain of approximately 0.15. Because of strong necking and roughening of the surface during the experiment it was not possible to obtain reliable values for $\rho_{GND,max}$ above a strain of $\varepsilon \approx 0.15$, however below this value the GND density $\rho_{GND,max}$ follows an ε^2 dependency (red crosses).

(a) Annealed (5 h, 1073 K) sample with 15.9 µm grain size and a partially bamboo-like microstructure The maximum GND density increased from $1 \cdot 10^{14}$ m^{-2} at $\varepsilon = 0$ to $2 \cdot 10^{14}$ m^{-2} at $\varepsilon = 0.105$, subsequently a $\Delta\sigma$ of approximately 100 MPa is expected. The engineering stress increases from $\sigma_{ys} = 25$ MPa to $\sigma = 56$ MPa at $\varepsilon = 0.105$. Under the assumption of a cross-section reduction of approximately 50 % at $\varepsilon = 0.105$ this would result in an increase of flow stress from 25 to 112 MPa, which is in good accordance with the calculated $\Delta\sigma$ of 100 MPa. Note that the EBSD image underestimates the cross-section of the necking zone due to faceting of the surface (post mortem SEM observations indicate a final cross-section in the necking zone of 25 % of the initial cross-section). Consequently it was not possible to calculate an appropriate true stress-strain curve.

(b) Sample with 10.1 µm grain size. The maximum GND density increased from $1.1 \cdot 10^{14}$ m^{-2} at $\varepsilon = 0$ to $5.5 \cdot 10^{14}$ m^{-2} at $\varepsilon = 0.144$, subsequently a $\Delta\sigma$ of approximately 205 MPa is expected. The true stress increases from $\sigma_{ys} = 51$ MPa to $\sigma = 137$ MPa at $\varepsilon = 0.144$, corresponding to an increase in flow stress of approximately 86 MPa, which is significant lower than the calculated value, most probably caused by a non-uniform cross-section reduction. However, if a twin boundary is traversable for GNDs, no significant hardening is expected [62]. Note that a little cusp caused by electrodeposition process has been removed by FIB. Furthermore, the EBSD images get distorted during tensile testing due to bending and facetting of the twinned area.

(c) Sample with 2.7 µm grain size. The maximum GND density increased from $0.8 \cdot 10^{14}$ m^{-2} at $\varepsilon = 0$ to $2.8 \cdot 10^{14}$ m^{-2} at $\varepsilon = 0.156$, subsequently a $\Delta\sigma$ of approximately 150 MPa is expected. The true stress increases from $\sigma_{ys} = 150$ MPa to $\sigma = 261$ MPa at $\varepsilon = 0.156$, corresponding to an increase in flow stress of approximately 111 MPa, which is in good accordance with the calculated value.

Paper D

Cyclic bending experiments on freestanding Cu micron lines observed by EBSD

A. Wimmer [a], W. Heinz [a], T. Detzel [b], W. Robl [c], M. Nellessen [d], C. Kirchlechner [d,e], G. Dehm [d,f]

a Kompetenzzentrum Automobil- und Industrie-Elektronik GmbH, A-9524 Villach, Austria
b Infineon Technologies Austria AG, A-9500 Villach, Austria
c Infineon Technologies Germany AG, D-93049 Regensburg, Germany
d Max-Planck-Institut für Eisenforschung GmbH, D-40237 Düsseldorf, Germany
e Department Materials Physics, Montanuniversitaet Leoben, A-8700 Leoben, Austria
f Erich Schmid Institute of Materials Science, Austrian Academy of Sciences, A-8700 Leoben, Austria

to be submitted

Abstract

Polycrystalline Cu samples with 20 • 20 µm² in size have been cyclically bent inside a scanning electron microscope until fracture occurred. The microstructural changes were investigated by secondary electron imaging and electron backscatter diffraction. The *in situ* experiments revealed for the coarse-grained samples that not the external stress dominates the cyclic deformation, but the local internal strength. This is in strong contrast to macroscopic bending samples, where deformation always happens near the fixed end of the bending beam and decreases constantly with increasing distance from the fixation. For micron-sized polycrystalline samples, the grain dimensions, dislocation density evolution, and grain orientation (Taylor factor) can define the location of failure if the grain size and sample diameter become similar in size.

A comparison with cyclic *in situ* tension-tension experiments (ratio of minimum stress to maximum stress $R \approx 0$) reveals that cyclic bending experiments ($R \approx -1$) undergo bulk-like fatigue deformation with extrusions/intrusions, in contrast to the experiments with $R \approx 0$. Both the cyclic tension-tension and bending experiments can be described by a Basquin equation although different mechanisms lead to failure of the samples.

1 Introduction

Static mechanical properties of metallic thin films are of great interest as they are frequently used in microelectronic devices and microelectromechanical systems (MEMS).. Consequently it is necessary to understand the basic mechanical properties of metallic thin films. However, in practical applications the stress state is predominantly cyclic with up to 10^{10} cycles, making it necessary to develop cyclic micromechanical experiments. In the past cyclic thermo-mechanical techniques have been developed such as repeated thermal cycling of thin films on a substrate [1 - 6] or Joule heating by using AC currents to cyclically vary the thermal stress in a conduction line [7, 8]. However, in these experiments the influence of temperature and stress cannot be separated. Consequently experiments for static tensile [9 - 11] and cyclic tension-tension testing [12 - 15] of free standing films have been

developed. As in practical applications cyclic loading with a negative stress ratio $R = \sigma_{min} / \sigma_{max}$ frequently occurs there is demand for micromechanical testing where tensile and compressive stresses alternate to identify the underlying deformation mechanism.

For macro-sized Cu single crystals the formation of persistent slip bands (PSBs) has been found above a critical shear strain value [16]. These PSBs have a thickness in the range of some microns and act as a nucleation site for fatigue cracks due to highly localized and reversible slip. In bulk ultrafine-grained (ufg) Cu (produced by equal channel angular pressing (ECAP)) with a grain size of 350 nm micro shear bands were observed [17]. In samples with bimodal grain size (350 and 5,000 nm) a vein dislocation structure, which was also observed in samples with 40 µm grain size, was found after fatigue testing [17]. Below a grain size of 300 nm grains are too small to allow the formation of cell structures [17]. However, due to fatigue induced bimodal coarsening large grains are built with shear bands and extrusions/intrusions on the free surface [18]. Finally ufg Cu shows a more significant Bauschinger effect than coarse-grained Cu due to the higher internal stresses [19, 20]. However, also impurities on grain boundaries play a crucial role for the fatigue lifetime of ufg Cu [21].

Bending experiments on micro-mechanical samples have shown monotonic hardening accompanied by activation of new glide planes, but no cyclic hardening [22]. In 20 µm thick Cu films the formation of PSBs and few extrusions, acting as crack initiation sites, have been reported for traction-traction experiments [23]. The extrusion width is decreasing with decreasing grain size and film thickness [24, 25]. However, if the grain size or film thickness is small, the deformation mechanisms are changing. Below 1-3 µm film thickness or grain size dislocation cell/wall structures are not formed and damage signs as extrusions and intrusions are not generated during fatigue testing [24, 25]. Fatigue damage mechanism maps for thin films [25] indicate different deformation mechanisms compared to bulk metals.

As surface grains are dominating the fatigue behavior in thin films [26], electron backscatter diffraction (EBSD) studies could give insights to fatigue damage. However up to now no *in situ* cyclic bending experiments inside the scanning electron microscope (SEM) accompanied by EBSD measurements have been performed to resolve hardening and deformation mechanisms in polycrystalline thin films.

In this study cyclic bending experiments with up to 146,000 cycles have been performed at 293 K. Stress-lifetime and strain-lifetime relationships have been analyzed for samples with 2 different grain sizes. Furthermore the deformation behavior of both kinds of samples is compared and the local evolution of the GND density as estimated from EBSD orientation gradients is analyzed. Finally differences in the deformation behavior of the bending experiments with $R \approx -1$ compared to cyclic tension-tension experiments with $R \approx 0$ are discussed.

2 Experimental details

The bending samples with a nominal cross-section of 20 • 20 µm² and a length of 260 µm were produced by a photolithographic process similarly as described in [9]. After electro-deposition one set of samples was annealed at 673 K for 30 min to obtain a stable grain size of 2.7 ± 0.6 µm. A second set of samples with a bamboo-type microstructure was obtained by an additional annealing at 1073 K for 4h. These samples possess a median grain size of 15.9 ± 3.4 µm, which was determined by EBSD analysis. Mechanical testing was performed with a micro-tensile device of Kammrath & Weiss [9, 27, 28]. The device was modified with a piezo-loading tool (see Fig. 1a) operating at 2 Hz. Sample dimensions were measured in the SEM prior to the micro-mechanical experiment. The bending force for calculation of the bending moment was measured with an oscillating tungsten wire [27 - 29].

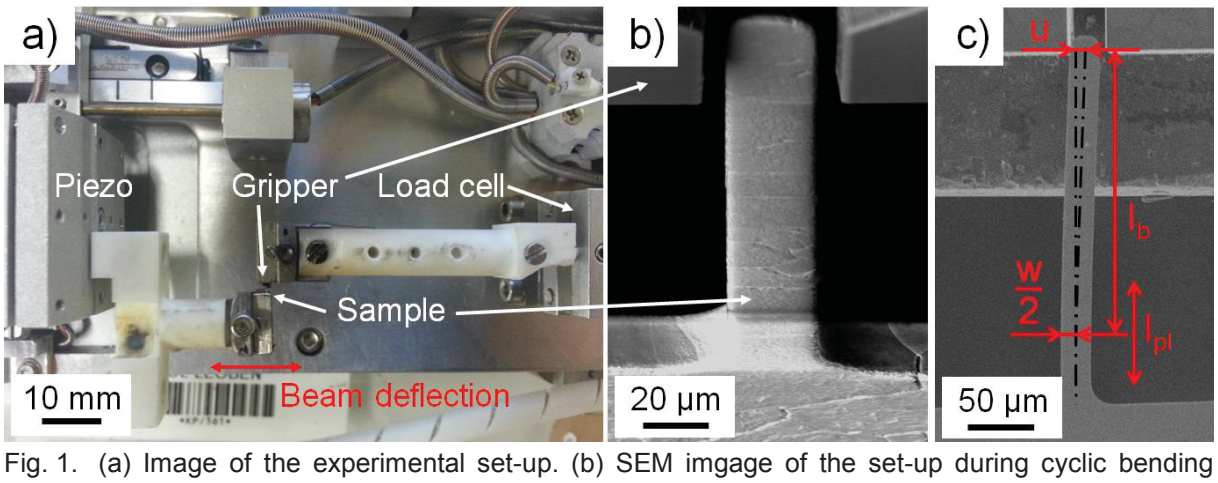

Fig. 1. (a) Image of the experimental set-up. (b) SEM imgage of the set-up during cyclic bending experiments. Note, that the sample and gripper are inclined by 70° for EBSD analysis resulting in a distorted image. (c) Parameters for calculation of plastic strain: u [µm] is the beam deflection, $w / 2$ [µm] the distance between the outer and neutral fiber, l_b [µm] is the bending distance between the gripper and the middle of the plastic zone and l_{pl} [µm] the length of the plastic zone.

The number of cycles to failure *N* was defined as the number of load cycles until the bending force *F*, which was between ± 1.0 and ± 2.5 mN in the beginning, reaches the deflection point where

$$\frac{\partial^2 F}{\partial N^2} = 0\,. \qquad (1)$$

This deflection point corresponds approximately to the number of cycles where *F* drops below F_{max} / 2 due to accumulation of fatigue damage. The bending samples were placed centrically in a silicon gripper (Fig. 1b) and the beam deflection was increased during the first few cycles until the desired bending force (stress level) was reached to prevent an overload at the beginning. The gap between the sample and the gripper was between 3.75 and 7 µm on both sides (Fig. 1b), resulting in a "gap" in the obtained mechanical hysteresis (see e.g. Fig. 2a), which had been corrected in a subsequent post processing step (Fig. 2a). The hysteresis of the load-displacement curve was used for calculation of the accumulated plastic strain. The plastic strain per cycle in the outer fiber ε_{pl} is:

$$\varepsilon_{pl} \approx \frac{u \bullet \frac{w}{2}}{l_{pl} \bullet l_b}\,, \qquad (2)$$

where *u* [µm] is the beam deflection, *w* / 2 [µm] the distance of the outer fiber from the neutral axis (= half sample width *w*), l_{pl} [µm] the length of the plastic zone and l_b [µm] the distance of the force application point from the middle of the plastic zone. The length of the plastic zone was measured from SEM images after cyclic bending. For geometric details see [30]. The maximum beam deflection *u* was varied between 4.5 and 19.5 µm by changing the amplitude of the piezo, resulting in a plastic strain per cycle between 0.01 and 0.05. For the experiment the mean force F_m was 0, consequently the maximum force F_{max} and minimum force F_{min} had the same value, i.e. $F_{max} = -F_{min}$. This results in a stress ratio $R = \sigma_{min} / \sigma_{max}$ of -1. The maximum stress in the outer fiber was calculated by dividing the bending moment $M = (2 - 5) \cdot 10^{-7}$ Nm and the samples axial section modulus

$$W = \frac{h \bullet w^2}{6}\,, \qquad (3)$$

where *w* ≈ 20 - 22 µm is the sample width and *h* ≈ 20 - 24 µm the sample thickness resulting in a section modulus *W* of $1.5 \pm 0.1 \cdot 10^{-15}$ m^3.

For EBSD experiments the piezo-module together with the sample were tilted to 70° and scans were performed at a force *F* = 0 inside a Zeiss LEO 1525 with an

EDAX DigiView 1612 camera. For this configuration EBSD scans can be performed after a certain number of cycles without changing the set-up permitting to follow orientation changes in an "*in situ*" like fashion. The density of geometrically necessary dislocations (GNDs) was calculated from the Kernel average misorientation (KAM) to the second nearest neighbor as described in [31]. For EBSD imaging loading was stopped and the electron beam scanned over an area of 20 • 110 µm². With a step size of 0.5 µm and 8 • 8 camera binning this results in a recording time of ≈ 5 min. The lower resolution limit of the EBSD system is 0.2°, while misorientations above 15° between neighboring positions were identified as grain boundaries. Consequently the lower limit in GND density which can be resolved is $3 \cdot 10^{13}$ m^{-2}. This value also provides an estimate of the minimum measurement error. The upper value in GND density of $2 \cdot 10^{15}$ m^{-2} is a theoretical limit as extrusions and intrusions cause severe surface roughening, resulting in a decreasing pattern quality. GND densities displayed in the figures are averaged over an area of 3 • 3 µm² to eliminate statistical outliers. For a post mortem, high-resolution EBSD study of the fatigued, coarse-grained Cu beam, the sample was embedded in a conductive resin and gently mechanically polished to obtain a smooth surface devoid of extrusions and intrusions. Subsequently, EBSD was performed on the beam with a step size of 100 nm and a camera binning of 5 • 5.

3 Results and discussion

Cyclic bending experiments are resulting in a hysteresis curve in the cyclic force-displacement diagram. An example for a force-displacement curve of the material with 2.7 µm grain size is presented in Fig. 2a. At a plastic strain per cycle ε_{pl} of 0.05 the area inside the curve is corresponding to 80 ± 10 nJ energy dissipation per cycle. This corresponds to 2.5 MJ/m³ if it is assumed that the plastic zone ranges across the whole cross-section and the length of the plastic zone is 80 ± 10 µm as resolved from post mortem SEM images (e.g. Fig. 4b). Similar energy absorption values of 1 – 10 MJ/m³ have been found for bulk Al samples at a plastic strain per cycle ε_{pl} of approximately 1 %, where the energy absorption per cycle dominated the lifetime in a fatigue experiment with R = -1 [33].

To calculate the increase in temperature of the plastic zone

$$\Delta T = \frac{Q}{c_{spec} \bullet m}, \qquad (4)$$

where Q = 80 nJ is the dissipated energy per cycle, m = 2.85 • 10^{-10} kg the mass of copper in the plastic zone and c_{spec} = 385 J kg^{-1} K^{-1} the specific heat capacity of copper [32], resulting in a ΔT of 0.73 K per cycle. Because of the fast heat transport from the plastic zone to the bulk the influence of temperature through energy dissipation in the plastic zone can be neglected, as in all experiments the plastic strain per cycle ε_{pl} was below 0.05.

The applied force of 1.0 – 2.5 mN results in a maximum stress of 100 - 240 MPa in the outer fiber of the Cu bending samples. During the first few bending cycles a deviation of the force-displacement curve from the elastic line (Fig. 2a) during unloading is visible. This is caused by the Bauschinger effect [34], induced by an internal back-stress on dislocations causing reverse plastic flow. While for Cu films subjected to a biaxial tensile stress a Bauschinger effect was only noticed in case of a surface passivation [35, 36], single-crystalline bending beams reveal a strong Bauschinger effect due to dislocation pile-up at the neutral axis [37, 38]. The effect was even enhanced when the neutral axis was sub-structured by a grain boundary [38]. In the present case several grain boundaries exist across the beam width explaining why a Bauschinger effect is also noticed in the unloading curves.

During the strain controlled experiment the maximum force (stress) increases during the first hundred cycles due to strain hardening, then remaining at a nearly constant plateau and finally decreasing (Fig. 2c) due to fatigue damage inside the material, which is also well known for bulk materials [16]. Consequently in the advanced state with increasing number of cycles also the dissipated energy per cycle is decreasing (Fig. 2b and c). After 2,000 cycles the dissipated energy per cycle is reduced to approximately 10 nJ and the cumulative dissipated energy reaches values of 100 µJ. The obtained stress-lifetime curves are shown in Fig. 2d. For the material with 2.7 µm grain size there is a linear relationship between stress and lifetime.

With decreasing plastic strain per cycle the number of cycles prior to failure increases (Fig. 2e), known as the Coffin-Manson relation [39]. If the plastic strain per cycle ε_{pl} is plotted against the number of cycles N, the slope of the curve corresponds to the Coffin-Manson exponent c. In this study a value of - 0.3 ± 0.1 was obtained for

both set of samples. This value is lower than the reported value of - 0.6 for bulk Cu [40], but in good accordance with c = - 0.43 measured in strain-controlled flex fatigue experiments reported by Merchant and Minor [41], where 12 – 35 µm thin electrodeposited Cu foils were bent/unbent around a mandrel as described in [42, 43]. However, the independency of c from the grain size was also found for ultrafine grained (ufg) Cu [18].

The accumulated plastic strain is estimated from the obtained hysteresis curves (Fig. 2a) and Eq. 1. Both set of samples show a linear relation between number of cycles to failure and the accumulated plastic strain, roughly lying on one linear slope (Fig. 2f), indicating a negligible influence of the microstructure. The accumulated plastic strain in the outer fiber exceeds for both materials 1,000 (Fig. 2f). However, as in the material with 15.9 µm grain size deformation was localized in a few grains the estimated size of the plastic zone l_{pl} could be overestimated, as deformation was not uniformly distributed across the whole length l_{pl}. Consequently the plastic strain per cycle and the accumulated plastic strain are prone to measurement errors and could be underestimated for the severely deformed grains where deformation was localized. On the other hand, for undeformed grains the plastic strain per cycle and the accumulated plastic strain could be overestimated. Furthermore, it is possible that during the experiment the zone of deformation is shifted to neighboring grains due to work hardening, resulting in an overestimation of the accumulated plastic strain.

The large accumulated plastic strain points out the significant difference between cyclic tension-tension experiments (ratcheting, $R \approx 0$ [15]) and cyclic tension-compression (bending, $R \approx -1$) experiments: While in ratcheting experiments the accumulated plastic strain is comparable to the elongation to fracture in the tensile test [15], for cyclic bending experiments the accumulated plastic strain exceeds the elongation to fracture of the tensile test by 3 orders of magnitude. This is also well known from macroscopic experiments [35, 44]. Furthermore, the differences in deformation mechanism between ratcheting [15] and cyclic bending experiments are also visible in the *in situ* SEM observations as discussed later.

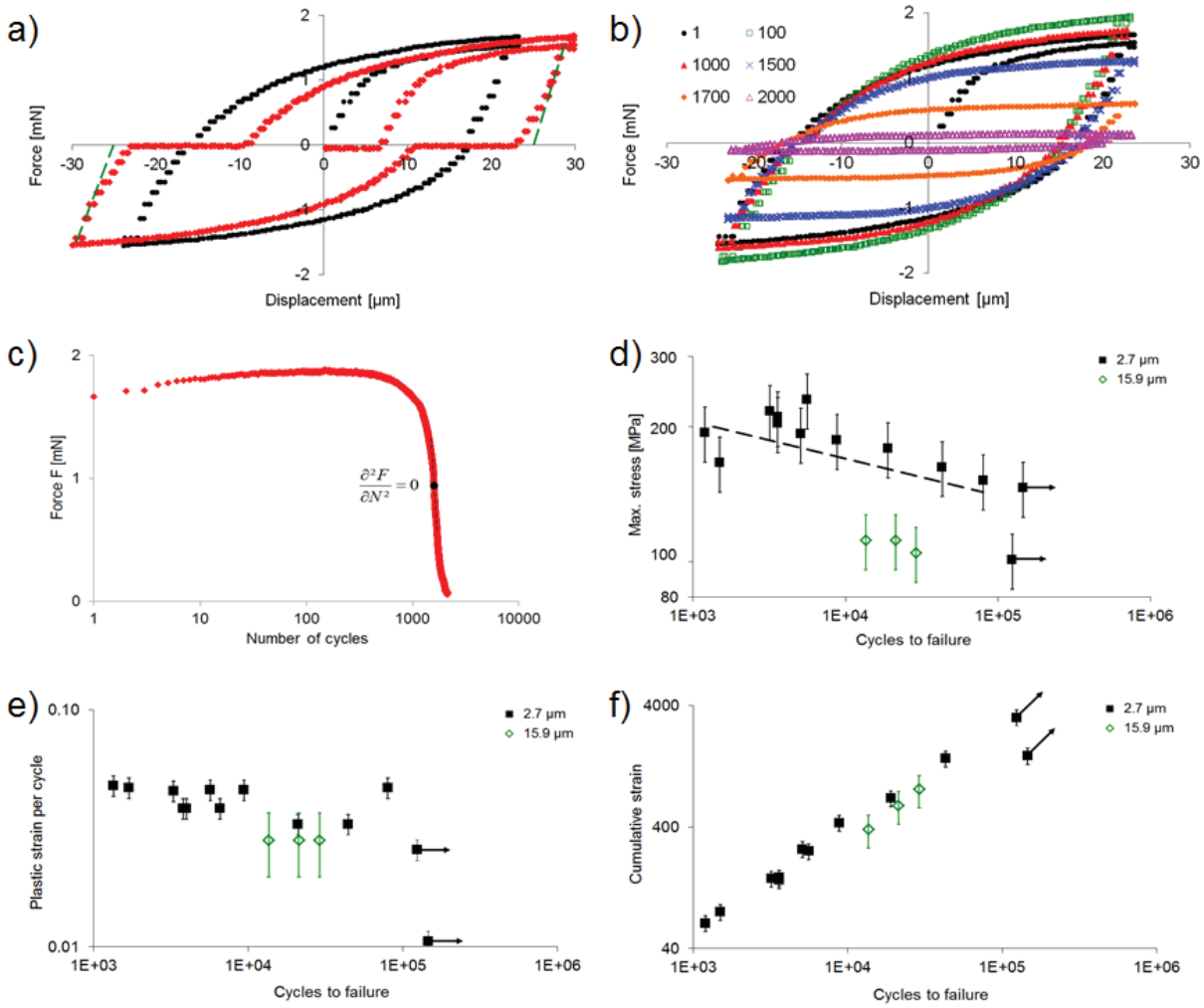

Fig. 2. Mechanical data obtained during cyclic bending experiments. (a) Hysteresis of a bending experiment (red = measured signal) of a sample with 2.7 µm grain size. For calculation of the area inside the hysteresis (black = corrected signal) is used. (b) Evolution of the hysteresis curve with increasing number of cycles. (c) Maximum bending force F plotted against the number of cycles. (d) Stress-lifetime curve for the material with 2.7 µm grain size (black symbols) and the samples with 15.9 µm grain size (green symbols). (e) Plastic strain per cycle plotted against the number of cycles to failure. (f) Cumulative strain-lifetime curves for the samples with 2.7 µm and 15.9 µm grain size.

Deformation behavior of the samples with 2.7 µm grain size

During the first 100 cycles of an experiment with ε_{pl} = 0.03 the sample remains nearly unaffected (Fig. 3a). After 10,000 cycles with ε_{pl} = 0.03 significant extrusions and intrusions can be detected on the surface (Fig. 3b), after 80,000 cycles with ε_{pl} = 0.03 the samples are heavily fatigue damaged (Fig. 3c). As expected the fatigue damage was concentrated close to the point of fixation of the freestanding beam, i.e. the area where the highest stresses occur.

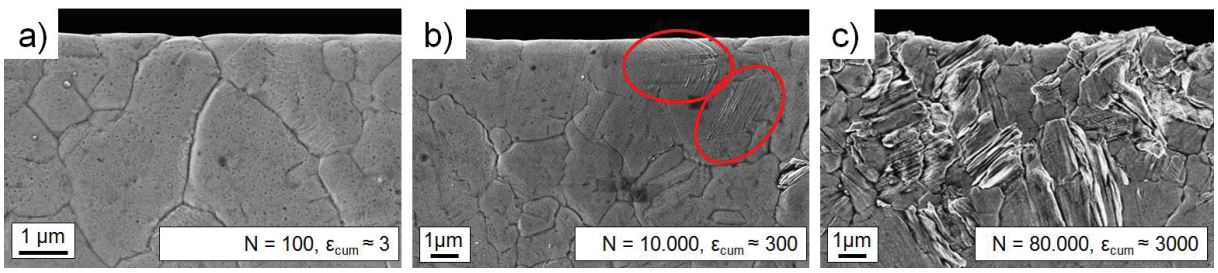

Fig. 3. Deformation behavior of the samples with 2.7 µm grain size and a plastic strain amplitude ε_{pl} of 0.03. (a) During the first 100 cycles no fatigue damage is visible in the SEM images. In some cases glide steps can be resolved. (b) After 10,000 cycles fatigue damage can be clearly resolved on the surface (red circles), and (c) finally after 80,000 cycles the sample is close to fracture due to heavy fatigue damage. Note, that images (a)-(c) are recorded from representative samples.

Deformation behavior and evolution of GND density of the samples with 15.9 µm grain size

Contrary to the samples with 2.7 µm grain size, for the samples with 15.9 µm grain size the fatigue damage is not localized only in the outer fiber close to the fixation, but rather it is extended over single grains up to 100 µm from the fixation. This documents a transition from a bulk-like behavior to a stochastic behavior typically observed when sample dimensions reach the micro-structural length scale.

The corresponding map of the GND density ρ_{GND} indicates the highest GND densities in this first 80-100 µm (Fig. 4c). The associated map of the inverse pole figure (IPF) indicates the strongest fatigue damage in grains with [112] and [212] crystallographic directions along the sample axis (Fig. 4d), where multiple slip (2 slip systems) is dominating [45, 46]. Finally, the heavily damaged grains reveal extrusions and intrusions of one dominating slip plane, which is also known from other cyclic experiments on polycrystalline oxygen-free high conductivity (OFHC) Cu [47]. The related map of the Taylor factor *M* indicates values of 3.5 - 4 in the heavily damaged grains (Fig. 4e). Although the grain orientation plays an important role, the sample dimension to grain size ratio *D* : *d* is dominating the deformation behavior. This holds true for single-crystalline cross-sections, in agreement with recent publications [48 - 50] and discussed later on.

The evolution of the GND density along the sample axis is presented in Fig. 5 (corresponding lines are indicated in Fig. 4). The highest GND densities were found

in the outer fibers (Fig. 5a and c); in the neutral fiber (Fig. 5b) the GND density remains nearly unaffected below 1 • 10^{14} m^{-2}. Beyond that there is a slight increase in the center of the sample close to line 4. However, in contrast to macroscopic bending experiments the evolution of the GND density in the outer fiber along the sample axis does not decrease constantly with apparent decreasing bending moment or respectively the stress in the outer fiber. Rather the GND density and the surface morphology are strongly affected by the microstructure of the samples.

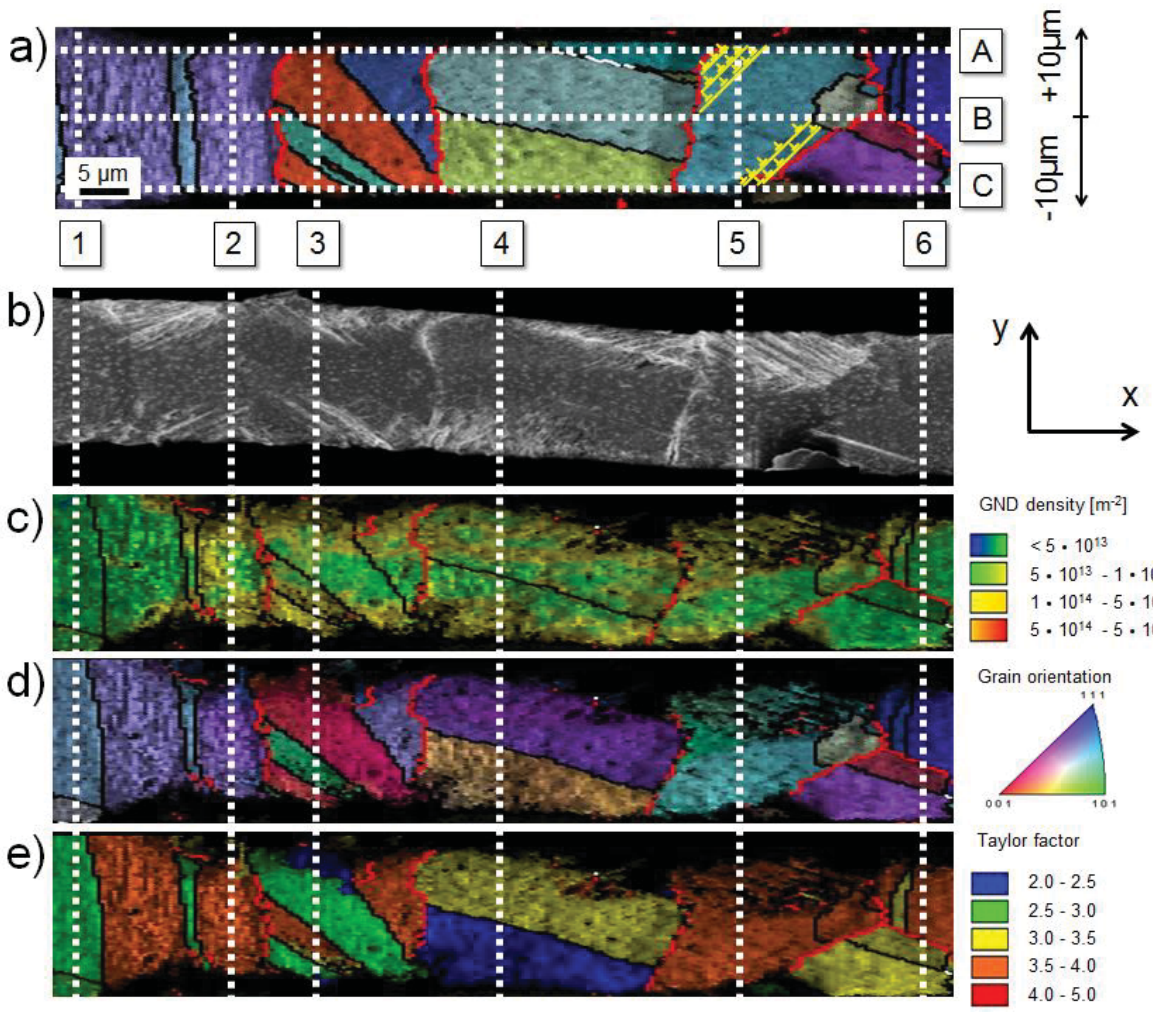

Fig. 4. (a) The initial microstructure of a 15.9 µm grained bending sample (fixation of the sample is on the left side of the images), showing the grain orientation in *x* direction (see Fig. 4d for color code). The evolution of the GND density was followed along the sample axis as positions A, B and C (see Fig. 5). While the lines A and C show the evolution of GNDs along the outer fibers, the line along B reveals the evolution of GNDs in the neutral fiber. Dotted lines 1-6 are used to display the evolution of the GND density across the sample surface in *y* direction (see Fig. 6). The schematic drawing in (a) (yellow) demonstrates a possible GND structure, explaining the evolution of the GND density in line 5 in Fig. 6e. (b) SEM image of the sample surface, showing extrusions and intrusions after 21,300 cycles. The corresponding EBSD images are showing the (c) GND density, (d) grain orientation in *x* direction and (e) Taylor factor. Note, that the scale bar in (a) is also valid for images (b-e).

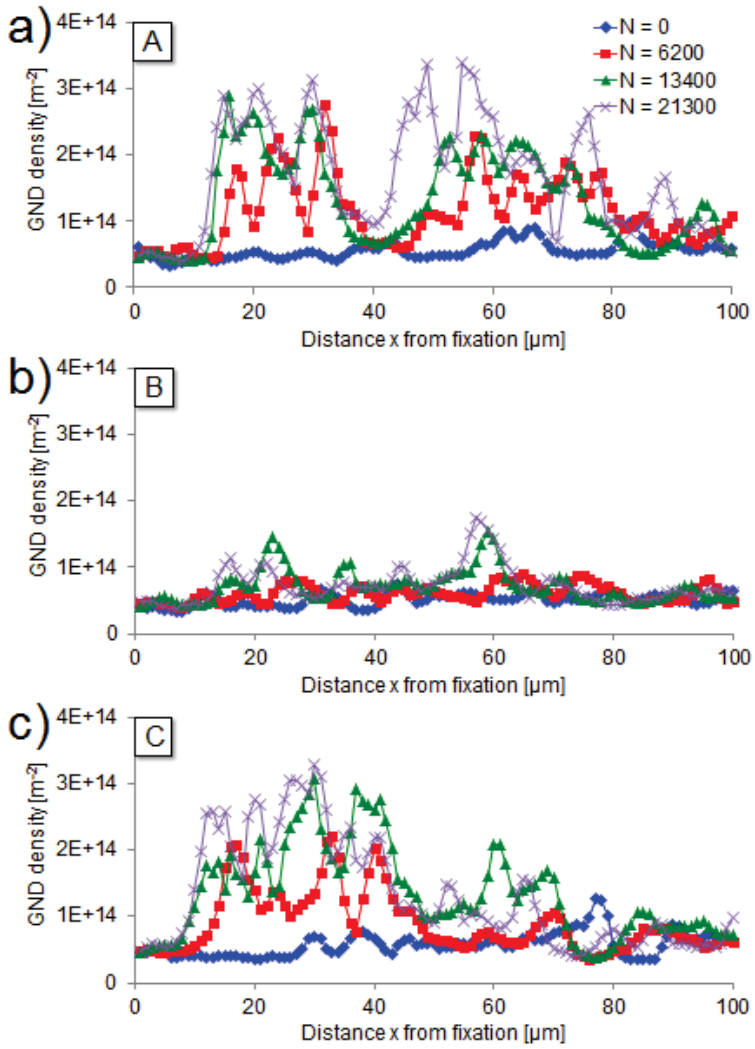

Fig. 5. Evolution of the GND density along the sample axis. N = 0 (blue curve) gives the GND density of the virgin sample, whereas at N = 6,200 (red), N = 13,400 (green) and N = 21,300 (violet) are showing the evolution during the experiment. (a) GND density in the outer fiber at y = + 10 µm, (b) GND density in the neutral fiber and (c) GND density in the outer fiber at y = - 10 µm. The length of the plastic zone l_{pl} is about 80 µm.

If the GND density along the cross-section perpendicular to the sample axis (lines 1-6 in Fig. 4) is analyzed in more detail, for line 1 (Fig. 4 and 6a) there is no increase in GND density during the experiment. The reason for this is the ≈ 40 % larger cross-section, caused by the rounding near the hinge, resulting in an axial section modulus twice as high as in the remaining sample. For line 2 (Fig. 4 and 6b) with a single-crystalline cross-section and line 3 (Fig. 4 and 6c) with a polycrystalline cross-section the GND density is constantly increasing up to $3 \pm 0.3 \cdot 10^{14}$ m^{-2} during the experiment in the outer fibers. In the neutral fiber the density remains below $1 \pm 0.3 \cdot 10^{14}$ m^{-2}. At the positions of line 2 and 3 the GND density increases and roughly follows $\rho_{GND} \sim \varepsilon_{cycle}(y)^2$, where ρ_{GND} is the GND density and $\varepsilon_{cycle}(y)$ is the

local strain per cycle, dependent on the distance from the neutral fiber (Fig. 6b and c). This approach is only valid in early stages of the experiment where strain hardening is dominating (see also Fig. 2b and c) and followed by fatigue damage in the late stages of the experiment where no further hardening takes place. This was also found in the evolution of the stress level and energy dissipation per cycle. This holds true especially for severe damaged grains close to the outer fiber where the maximum stress appears. For line 4 (Fig. 4 and 6d) with a bi-crystalline cross-section both grains show an increase in dislocation density close to the twin boundary and in the outer fibers. The accumulation of GNDs at grain boundaries indicates that the twin boundary acts as an obstacle for GNDs. Micro-compression experiments on single-crystalline and bi-crystalline samples [51] revealed, that the type of grain boundary strongly influences the deformation behavior of a sample: Samples with a certain kind of twin boundary show a comparable behavior to single-crystalline samples, as screw-dislocations can cross-slip through well oriented, coherent ∑3 (111) twin boundaries. Samples with a large angle grain boundary show strong hardening as dislocations accumulate on the impassable grain boundary [51, 52]. Furthermore in other bi-crystalline micro bending beams also a pile-up was found [38].

For line 5 (Fig. 4 and 6e) with a single-crystalline cross-section only the upper part of the grain shows a strong increase in GND density up to $3.2 \pm 0.3 \cdot 10^{14}$ m^{-2}. Up to now such an asymmetric increase in dislocation density was not found for single-crystalline bending beams [53]. Nevertheless, due to the bamboo-structure neighboring grains significantly influence the dislocation activation and storage. As line 5 was measured close to the grain boundary, this could result in an asymmetry as shown in Fig. 6c, a possible GND structure is sketched in the corresponding grain in Fig. 4a. At the position of line 6 (Fig. 4 and 6f) the expected stress level is already reduced to 70 % of the maximum stress due to the large distance from the support of the beam. Subsequently, the GND density remains rather constant at around $1 \pm 0.3 \cdot 10^{14}$ m^{-2}, however with a slight increase in the outer fibers.

All lines in the deformation zone (lines 2-6, Fig. 6b-f) reveal an increase in GND density in the outer fibers. One possible explanation is that the higher local strain per cycle $\varepsilon_{cycle}(y)$ causes a dislocation network and cell structure resulting in a pile up of GNDs, not necessarily on one plane. Another explanation could be that the

higher local stress in the outer fibers is activating more dislocation sources. These dislocations are moving to the sample center (neutral fiber) and are interacting with other dislocations because of the multiple slip orientation of grains. Due to this interaction the accumulated dislocations do not show any distinct Burgers vector and line element, and therefore are harder to detect by orientation mapping. In contrast, close to the operating source the dislocation type is believed to be more distinct leading to a higher apparent GND density.

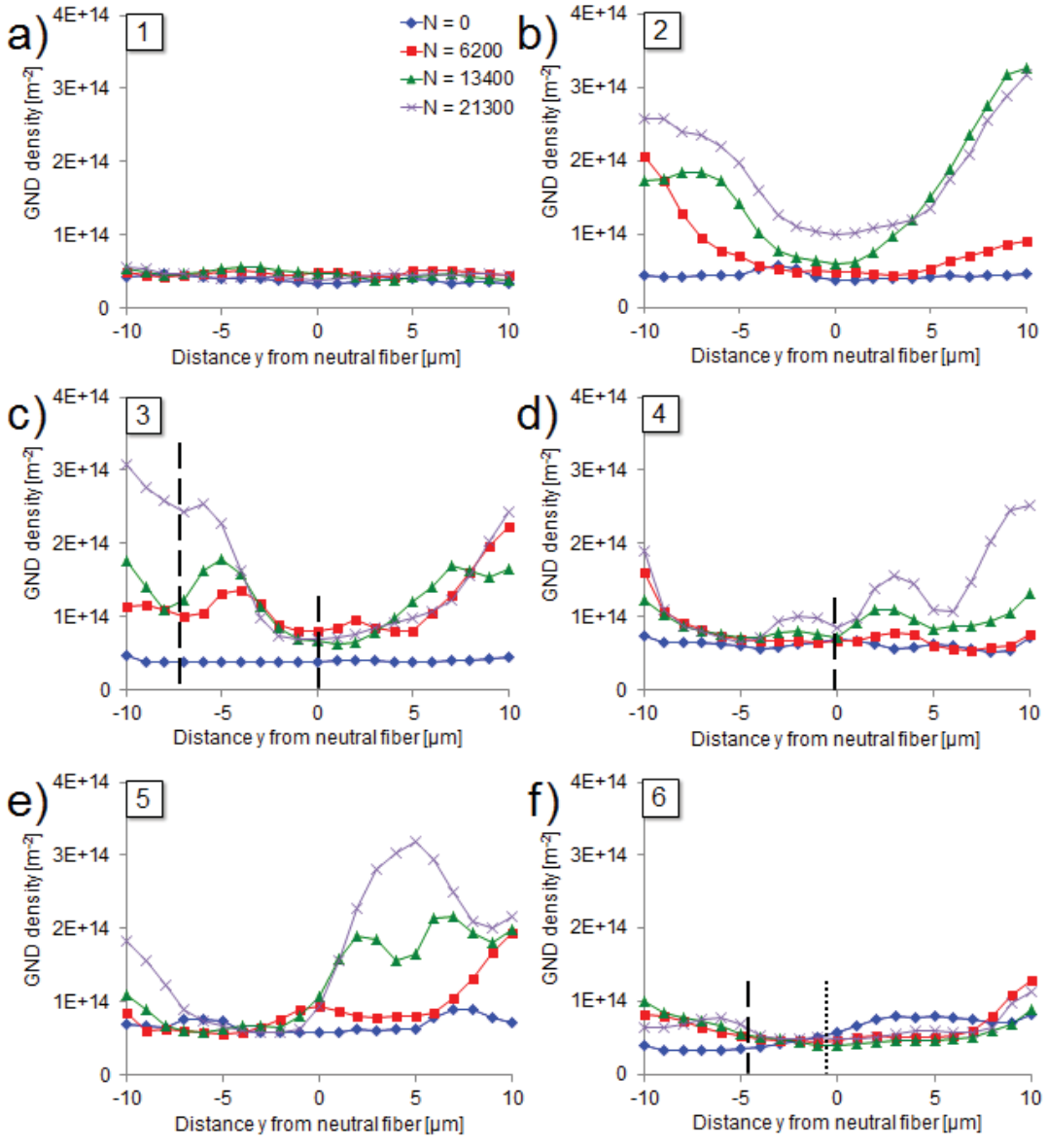

Fig. 6. Evolution of the GND density perpendicular to the sample axis (*y* direction in Fig. 4) in (a) line 1, (b) line 2, (c) line 3, (d) line 4, (e) line 5, and (f) line 6, for line positions see Fig. 4. *N* = 0 (blue curve) gives the initial GND density prior to testing, while at *N* = 6,200 (red), *N* = 13,400 (green) and *N* = 21,300 (violet) the GND density during the experiment is shown. ∑3 twin boundaries are indicated with dashed lines (c, d and f), a large angle grain boundary in (f) is indicated by a dotted line.

Post mortem observations with a high spatial EBSD resolution reveal typical fatigue damage in the samples after cyclic bending (Fig. 7). Close to the samples fixation (Fig. 7a, b) extrusions and intrusions are resolved in the secondary electron image, while the high-resolution EBSD image reveals local orientation changes on the µm level length scale indicating the formation of dislocation cell structures and shear band like structures (Fig. 7c). Such localized orientation changes caused by organized dislocation structures cannot be resolved in the *in situ* like EBSD measurements due to the larger step size, the averaging over areas of 3 • 3 μm^2 and the binning of 8 • 8, all required to significantly reduce recording time from hours to a few minutes. The findings are in agreement with TEM studies on fatigued Cu thin films, where wall and cell structures were also found in the samples if both the grain size and film thickness were above ≈ 1 µm [24, 25]. Furthermore electron channeling contrast images (ECCI) of fatigued Cu thin films with a thickness of 40 µm and a grain size of 46.2 µm also showed a cell structure with a comparable cell size [26]. The cell size of approximately 1 µm is in good accordance with the observed cell size in large grains of ufg Cu [18]. Furthermore it has been found, that the cell size decreases with increasing stress level [18]. During cyclic loading of ufg Cu with 350 nm grain size also micro shear band formation in coarsened grains was observed [17]. Moreover in fatigued single-crystalline Cu a cell structure has been found [16].

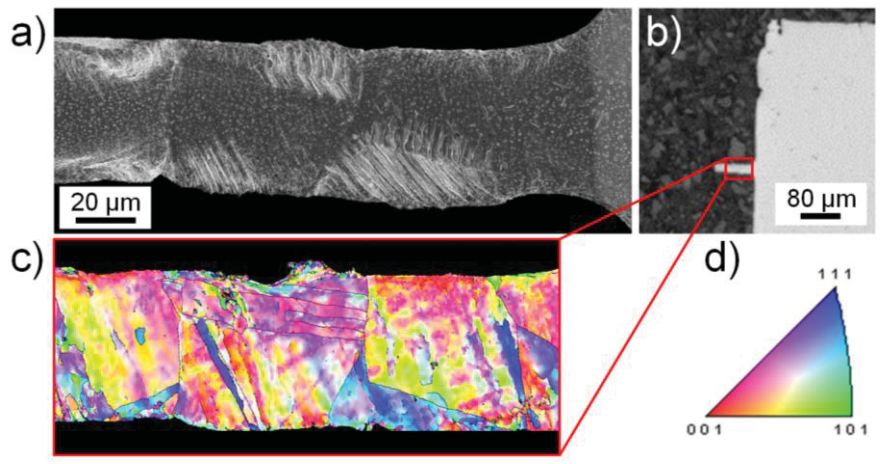

Fig. 7. Post mortem images of a 15.9 µm grained sample after cyclic bending. The (a) SEM image is dominated by extrusion and intrusion formation, (b) is showing the conductive embedded and mechanically polished sample and (c) EBSD image of the area marked in (b) showing the extensive formation of cell structures, shear bands and local arrangement of dislocations. (d) color code of the inverse pole figure corresponding to the grain orientations.

It is well known, that strength is increasing with decreasing grain size [54, 55], furthermore recent publications [48 - 50] have shown a strong influence of the sample dimension to grain size ratio D : d. If less than 25 grains are remaining in a cross-section area, the influence of the free surface becomes increasingly noticeable

and the strength decreases [48 - 50]. This has been also shown for micron-sized Cu tensile samples [15] and for ratcheting experiments [15]. This effect is also visible in fatigue experiments: As soon as a well oriented large grain extends over the entire cross-section, dislocations can freely move and the deformation is confined within this grain. The tremendous strain localization leads to massive damage accumulation and crack initiation in this single grain. Thereby, the stress acting on the outer fiber of the failing grain is estimated to be 70 % lower than the maximum present stress close to the fixation. It is clear that single large grains cause catastrophic failure of the entire Cu line.

Although there are significant differences in deformation mechanism between cyclic tension-tension and tension-compression experiments, it is possible to describe phenomenological both stress-lifetime relationships with a Basquin equation:

$$\sigma_a = \sigma_f' \bullet (2N)^{-b}, \tag{5}$$

where σ_a [MPa] is the stress amplitude, σ_f' [MPa] the fatigue stress coefficient and b the fatigue stress exponent, parameters are given in Tab. 1. This demonstrates, that the Basquin equation can be used to describe cyclic experiments with different values of R, however the applicability of the Basquin equation is not shedding any light on the failure mechanism. This is also demonstrated by the fact, that for the same material the obtained Basquin parameters depend on the mode of experiment. Tab. 1 summarizes the σ_f' and b values for the cyclic bending fatigue study presented here and an earlier cyclic tension-tension experiment on the same material [15]. The values for b are in good accordance with literature values for 18 µm thick Cu films [41]. Dependent on the heat treatment of the Cu samples after deposition values between 0.012 and 0.12 had been obtained [41].

Tab. 1. Parameters for the Basquin equation and cumulative plastic strain ε_{cum}. Note, that the values for σ_f' and b are changing with the mode of experiment and the tremendous difference in accumulated plastic strain to failure, ε_{cum}. Moreover, d is the grain size, ε_f is the elongation to fracture in the tensile test and c is the Coffin-Manson exponent, which was determined to c = -0.3 ± 0.1 in the present study. Error bars present the 95 % confidence intervals.

d [µm]		$R \approx 0$ (stress controlled)	$R \approx -1$ (strain controlled)
2.7	σ_f' [MPa]	295 ± 10 [15]	437 ± 40
	b	0.03 ± 0.02 [15]	0.09 ± 0.06
	ε_{cum}	ε_f = 0.46 [15]	$\varepsilon_{cum} \approx \varepsilon_f \cdot N^{1+c}$

4 Summary and conclusions

In this study micromechanical strain controlled bending experiments on micron-sized Cu lines with up to 146,000 cycles have been performed. The deformation behavior with respect to local mechanical properties and GND density evolution analyzed by EBSD has been investigated. During the first few cycles, where hardening is observable, the Bauschinger effect is present in the stress-strain hysteresis. It is demonstrated, that the local deformation is not only dominated by the external stress level as in bulk-like samples, but rather controlled by the local microstructure, i.e. crystallographic orientation, grain dimension and neighboring grains, which in turn determines the local flow stresses.

Compared to thin Cu films which show no fatigue surface damage and cell structure if the grain size or film thickness is below ≈ 1 µm [24, 25], our samples show the extensive formation of extrusions/intrusions, cell structures and shear bands due to the larger grain size and film thickness.

Finally, the deformation behavior and cycles to failure as functions of stress have been compared with stress controlled cyclic tension-tension experiments [15], showing significant differences in the damage evolution and lifetime. Independent from the stress ratio $R = \sigma_{min} / \sigma_{max}$ a lifetime prediction with a Basquin equation is possible; however the Basquin parameters are changing with the stress ratio R.

Acknowledgement

Part of this work was jointly funded by the Austrian Research Promotion Agency (FFG, Project No. 831163) and the Carinthian Economic Promotion Fund (KWF, contract KWF-1521|22741|34186). The authors want to thank S. Zaefferer for fruitful discussions, furthermore our gratitude is expressed to J. Fugger. Thanks for technical assistance is expressed to A. Leitner, M. Augustin, H. Felber, R. Grilz, H. Groß, F. Hubner, M. Krug, R. Leuschner, C. Lindner, K. Matoy, S. Modritsch, T. Ostermann, G. Reiter, H. Schönherr and K. Schrettlinger.

References

1 WD Nix, Metallurgical Transactions A 20, 11, (1989), 2217-2245.

2 JC Bravman, WD Nix, DM Barnett, DA Smith, Mater. Res. Soc. Symp. Proc. 130, Pittsburgh, PA, (1996), 129.

3 W Heinz, R Pippan, G Dehm, Mat. Sci. Eng. A 527, (2010), 7757-7763.

4 R Moenig, RR Keller, CA Volkert, Rev. Sci. Instrum. 75, (2004), 4997.

5 SP Baker, A Kretschmann, E Arzt, Acta Mater. 49, (2001), 2145-2160.

6 W Heinz, G Dehm, Surf. & Coat. Tech. 206, (2011), 1850-1854.

7 R Shaviv, GJ Harm, S Kumari, RR Keller, DT Read, Microel. Eng. 92, (2012), 111-114.

8 RR Keller, RH Geiss, N Barbosa, AJ Slifka, DT Read, Metall. Mater. Trans. A 38, 13, (2007), 2263-2272.

9 M Smolka, C Motz, T Detzel, W Robl, T Griesser, A Wimmer, G Dehm, Rev. Sci. Instrum. 83, (2012), 064702.

10 NC MacDonald, SG Adams, AA Ayon, KF Böhringer, LY Chen, JH Das, D Haronian, W Hofmann, XT Huang, A Jazairy, RE Mihailovich, SA Miller, I Ogo, R Prasad, BW Reed, MTA Saif, KA Shaw, RY Webb, Y Xu, Microel. Eng. 30, (1996), 563-564.

11 D Kiener, W Grosinger, G Dehm, R Pippan, Acta Mater. 56, 3, (2008), 580-592.

12 Y Hwangbo, JH Song, Int. J. of F. 38, (2012), 1-6.

13 B Yang, C Motz, W Grosinger, G Dehm, Mat. Sci. Eng. A 515, (2009), 71-78.

14 B Yang, C Motz, W Grosinger, G Dehm, Proc. Eng. 2, (2010), 925-930.

15 A Wimmer, A Leitner, T Detzel, W Robl, W Heinz, R Pippan, G Dehm, Acta Mater. 67, (2014), 297-307.

16 H Mughrabi, Mat. Sci. Eng. 33, (1978), 207-223.

17 HW Höppel, M Kautz, C Xu, M Murashkin, TG Langdon, RZ Valiev, H Mughrabi, Int. J. of Fat. 28, (2006), 1001-1010.

18 H Mughrabi, HW Höppel, Int. J. of Fat. 32, (2010), 1413-1427.

19 A Vinogradov, Y Kaneko, K Kitagawa, S Hashimoto, RZ Valiev, Mater. Sci. Forum 269–272 (1998), 987-992.

20 M Haouaoui, I Karaman, HJ Maier, Acta Mater. 54, (2006), 5477-5488.

21 L Collini, Proc. Eng 2, (2010), 2065-2074.

22 D Kiener, C Motz, W Grosinger, D Weygand, R Pippan, Scripta Mater. 63, (2010), 500-503.

23 M Judelewicz, HU Kiinzi, N Merk, B Ilschner, Mat. Sci. Eng. A 186, (1994), 135-142.

24 GP Zhang, CA Volkert, R Schwaiger, E Arzt, O Kraft, J. Mater. Res. 20, 1, (2005), 201-207.

25 GP Zhang, CA Volkert, R Schwaiger, P Wellner, E Arzt, O Kraft, Acta Mater. 54, (2006), 3127-3139.

26 CY Dai, B Zhang, J Xu, GP Zhang, Mat. Sci. Eng. A 575, (2013), 217-222.

27 B Yang, C Motz, W Grosinger, W Kammrath, G Dehm, Int. J. Mater. Res. 99, (2008), 716-724.

28 B Yang, C Motz, W Grosinger, G Dehm, Mat. Sci. Eng. A, 515, (2009), 71-78.

29 C Kirchlechner, J Keckes, JS Micha, G Dehm, Adv. Eng. Mat. 13, 8, (2011), 837-844.

30 W Grosinger, Master thesis, University of Leoben, (2011), 29-31.

31 LP Kubin, A Mortensen, Scripta Mater. 48, (2003), 119-125.

32 HH Binder, Lexikon der chemischen Elemente, S. Hirzel, Stuttgart, (1999).

33 JS Santner, ME Fine, Scripta Met. 2, (1977), 159-162.

34 J Bauschinger, Mittheilungen aus dem mechanisch-technischen Laboratorium der k. technischen Hochschule in Munchen, 13, Ch. 5, (1881), 31.

35 Y Xiang, JJ Vlassak, Acta Mater. 54, (2006), 5449-5460.

36 Y Xiang, JJ Vlassak, Scripta Mater. 53, (2005), 177-182.

37 E Demir, D Raabe, Acta Mater. 58, (2010), 6055-6063.

38 MW Kapp, C Kirchlechner, R Pippan, G Dehm, (2014), submitted.

39 LF Coffin, Jr., Met. Eng. Q. 3, (1963), 22.

40 WD Nix, JC Gibeling, Flow and Fracture at Elevated Temperature, Amer. Soc. for Metals, Metals Park, (1985).

41 HD Merchant, MG Minor, J. of Elec. Mat. 28, 9, (1999), 998-1007.

42 ASTM ET-86a guideline.

43 ASTM E345 guideline.

44 XW Li, WP Jia, ZG Wang, SX Li, J. of Mat. Sci. Lett. 19, (2000), 641-643.

45 WF Hosford, Mechanical Behavior of Materials, Cambridge University Press, (2005), 125-128.

46 T Takeuchi, Trans. JIM 16, (1975), 629-640.

47 AH Cottrell, D Hull, Proc. R. Soc. Lond. A 242, (1957), 211-213.

48 B Yang, C Motz, M Rester, G Dehm, Phil. Mag. 92, 25-27, (2012), 3243-3256.

49 XW Gu, CN Loynachan, Z Wu, YW Zhang, DJ Srolovitz, JR Greer, Nano Lett. 12, (2012), 6385-6392.

50 DC Jang, JR Greer, Scr. Mater. 64, (2011), 77.

51 PJ Imrich, C Kirchlechner, C Motz, G Dehm, Acta Mater. 73, (2014), 240-250.

52 LL Li, XH An, PJ Imrich, P Zhang, ZJ Zhang, G Dehm, ZF Zhang, Scripta Mater. 69, (2013), 199-202.

53 C Kirchlechner , W Grosinger , MW Kapp , PJ Imrich , JS Micha , O Ulrich , J Keckes , G Dehm, C Motz, Phil. Mag. 92:25-27, (2012), 3231-3242.

54 EO Hall, Proc. Roy. Soc. B 64, (1951), 747-753.

55 NJ Petch, J. Iron Steel 174, (1953), 25-28.

5 Appendix

In Appendix A the influences of alloying and annealing are discussed. Appendix B demonstrates the influence of sample dimensions, while Appendix C focusses on the optimization of the sample production process. Appendix D presents an enhanced sample holder, and finally Appendix E gives an empiric formula for the estimation of the local flow stress.

A Effect of alloying elements

A.1 Introduction

To control the grain size during electrodeposition, additives in the electrolyte system are needed. This can result in an embrittlement of grain boundaries in Cu thin films at elevated temperatures as shown in appended Paper A. The strength of the grain boundary can be influenced by different metallic elements [1, 2]. Consequently the influence of alloying and ion bombardment combined with a heat treatment was analyzed to optimize the elongation to fracture at elevated temperatures.

A.2 Experimental details, sample preparation and characterization

The samples were alloyed by electrodeposition of Au and Pd from a liquid solution in a laboratory scale process (5 V, 10 s, Pt anode, cathode-anode distance 20 mm). The Au-deposition was performed with 0.5 % $HAuCl_4$ solution (pH = 4), for Pd-deposition a 1 % $PdNO_3$ (pH = 5) was used. Taking into account the diffusion coefficients of Au (D_{Au} (1100 K) = $1.17 \cdot 10^{-14}$ m²/s [3]) and Pd (D_{Pd} (1100 K) = $2.62 \cdot 10^{-15}$ m²/s [4]) in Cu, an annealing time of 5 h at 1073 K will led to 10 % higher Au content on the surface of the 20 • 20 µm² tensile sample than in the sample center. For Pd the surface concentration will be about two times higher than in the sample center because of the lower D_{Pd}. The surface concentration measured by energy-dispersive X-ray spectroscopy (EDX) was 10 at% (25 wt%) in the case of Au and 2 at% (3 wt%) in the case of Pd, which shows a much faster Au deposition from liquid solution on Cu. This is in good accordance with an APT measurement on the Au alloyed sample showing a uniform distribution of Au in the

Cu matrix (25 at%, Fig. A1), indicating that Au is mainly used for solid solution hardening which excludes the formation of CuAu or Cu_3Au precipitations (Fig. A1).

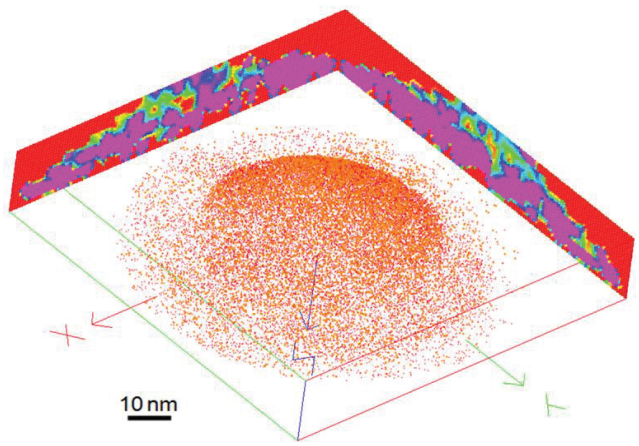

Fig. A1. APT measurement of the Au alloyed and annealed sample showing uniform Au distribution (only Au atoms (red) are shown, Cu atoms are not displayed).

The Ag and Sn alloyed samples have been prepared by electrolytic deposition of the metals from liquid solution on the surface of Cu micron samples in an industrial scale process. Through a heat treatment at 1073 K for 5 h the deposited metals diffused into the Cu matrix and were distributed evenly (Fig.A2a - c). The samples with 30 % Sn (CuSn30) were tested only in the as deposited state as the annealed samples showed liquid phases during heat treatment (Fig. A2).

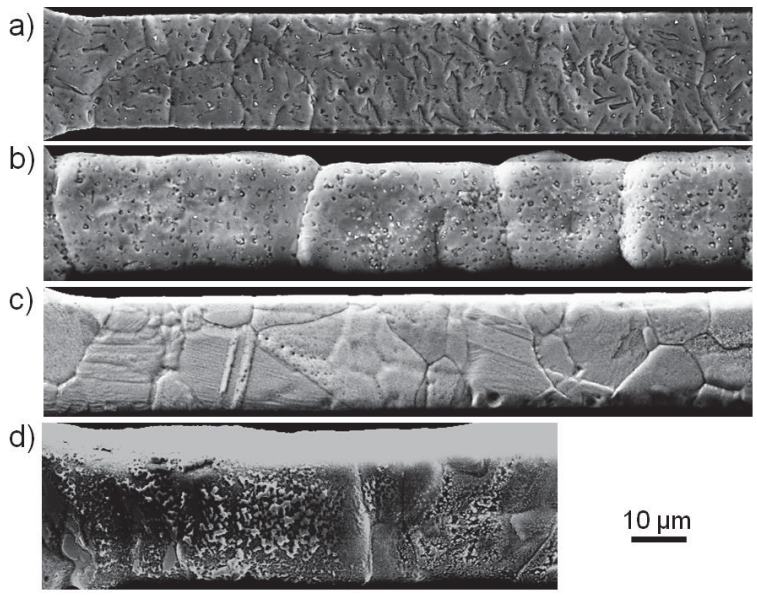

Fig. A2. Samples alloyed with Ag and Sn produced by electrodeposition in an industrial scale process and subsequent annealing process. Sample with (a) 3 % Ag, (b) 30 % Ag, (c) 3 % Sn and (d) 30 % Sn. Note, that all samples showed grain growth during annealing. Samples with 30 % Ag (b) and 3 % Sn (c) reveal a bamboo-like microstructure, the sample with 30 % Sn (d) showed partial meting during annealing and the sample decreased in length and could not be tested due to the increase in cross-sectional area.

The B alloyed samples were produced by B^+ ion bombardment with energies up to 4 MeV of the Cu micron-samples from both sides. The samples prepared for implantation are shown in Fig. A3. Two sample holders, which are described more in detail in the Appendix C, were adhered to a small piece of a silicon wafer for B implantation. Between the two sample holders additional samples were included on the wafer piece to allow extensive mechanical testing and chemical characterization.

After B implantation a thin, electron transparent layer appeared on the surface (Fig. A4a). A TOF-SIMS depth profile of B concentration has shown an implantation depth of ≈ 4 µm (measurement plane: 100 • 100 µm², analysis with Bi^{3+}, depth sputtering with Cs^+, Fig. A4b). The thin surface layer was not resolved in the SIMS measurement. Mechanical testing was performed with a strain-rate of 0.001 s^{-1}.

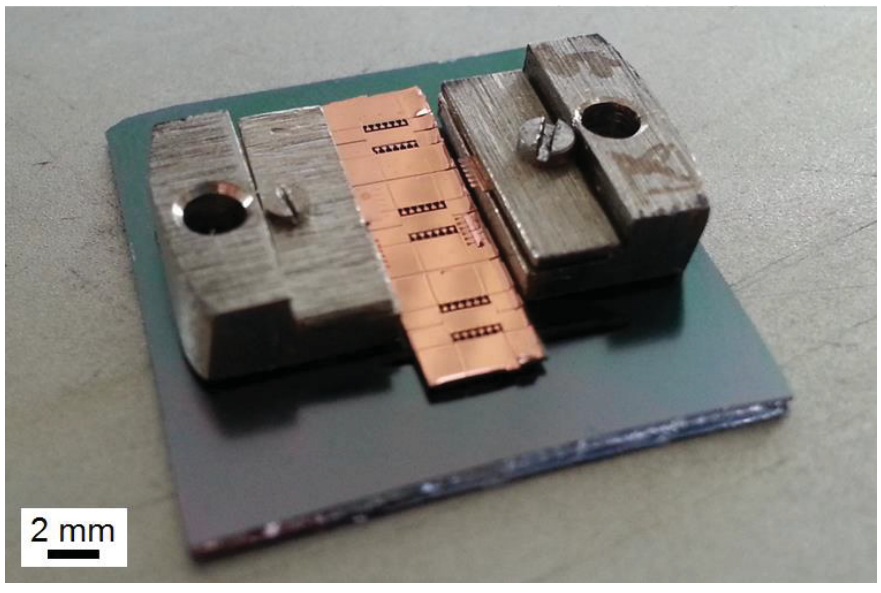

Fig. A3. Cu micron-samples prior to the B-implantation. Two of the macro samples (with each 6 micro-samples) are already positioned in the clamps for the experiment, below them 6 macro-samples were adhered to a Si ground plate. Note that a good thermal connection between samples and the Si plate is needed, as during implantation in high-vacuum a heat output of 10 W will be generated.

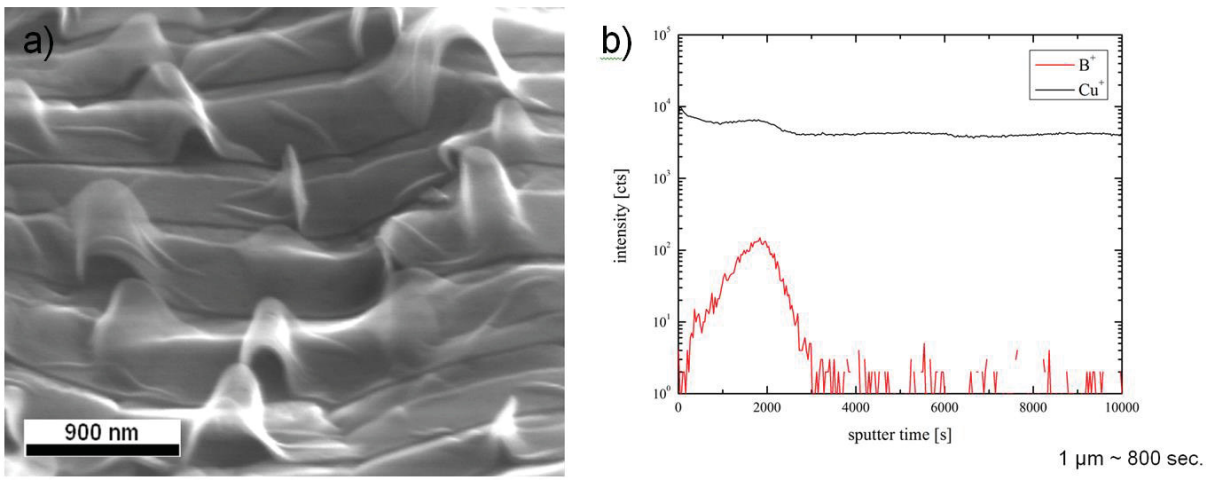

Fig. A4. Analysis of the CuB0.5 samples. (a) A thin film buckling from the surface after B-implantation and (b) SIMS measurement of the B depth profile.

It has been attempted to incorporate carbon nanotubes (CNTs) in electrodeposited Cu films, as CNT reinforced thin films could have significant advantages in strength with negligible effects on electrical and thermal conductivity. However the dispersed CNTs were not incorporated in the thin films and remained on the surface (Fig. A5), consequently these samples were not tested.

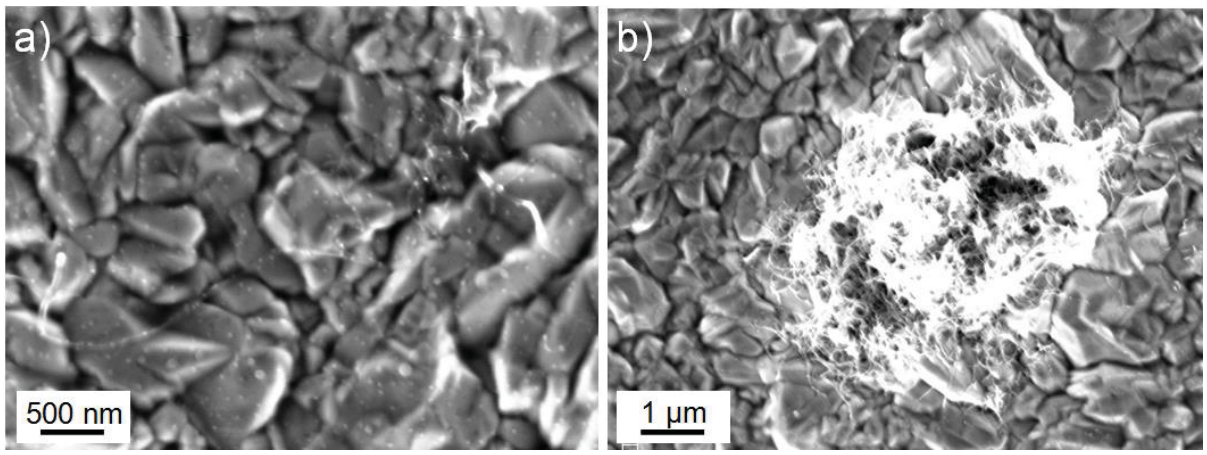

Fig. A5. CNT on the surface of a Cu thin film. (a) A single CNT and (b) a ball of CNTs.

A.3 Results and Discussion

Through the annealing process of the electroplated Cu samples the initial grain size of 2.7 µm increased to 15 ± 5 µm. Through this, there was a significant drop in strength for the samples with 3 and 30 % Ag (CuAg3 and CuAg30) and the samples with 3 % Pd (CuPd3) at 293 K (Fig. A6a). However, the effect of solid solution hardening compensated the drop in strength through the larger grain size for the samples alloyed with 25 % Au (CuAu25) and 3 % Sn (CuSn3). The B implantation increased the yield strength to 283 MPa and the UTS to 355 MPa (Tab. A1). At 473 K the 2.7 µm Cu samples and B-implanted samples showed a massive drop in ductility and a drop in elongation to fracture at 14 %, caused by embrittlement of the grain boundaries (Fig. A6). However, the B-implanted samples still showed a much higher yield strength and UTS compared to undoped samples. The alloyed samples had a much higher ductility after annealing, indicating that through the heat treatment the S was removed from the grain boundary independent if Au, Ag, Sn or Pd was added prior to the heat treatment. Furthermore the samples alloyed with Au, Sn and Pd showed a significant higher strength resulting from solid solution hardening. The Ag additions brought no advantages to the strength, however the CuAg30 samples showed the highest elongation to fracture at 473 K. Higher Sn additions (in the case of the as-deposited CuSn30) brought disadvantages compared to the CuSn3 samples both for the strength and elongation to fracture, most probably caused by the formation of a soft Sn phase.

The samples which were tested prior to annealing (consequently with a thin film of the deposited metal on the surface) showed a higher strength and lower elongation to fracture compared to the annealed samples with nearly even distribution of the deposited metal in the Cu matrix (Tab. A1). One possible explanation is that the metal surface layer is a barrier for dislocations on the free surface. Consequently dislocations cannot escape and accumulate in the material, increasing the strength of the samples (Tab. A1).

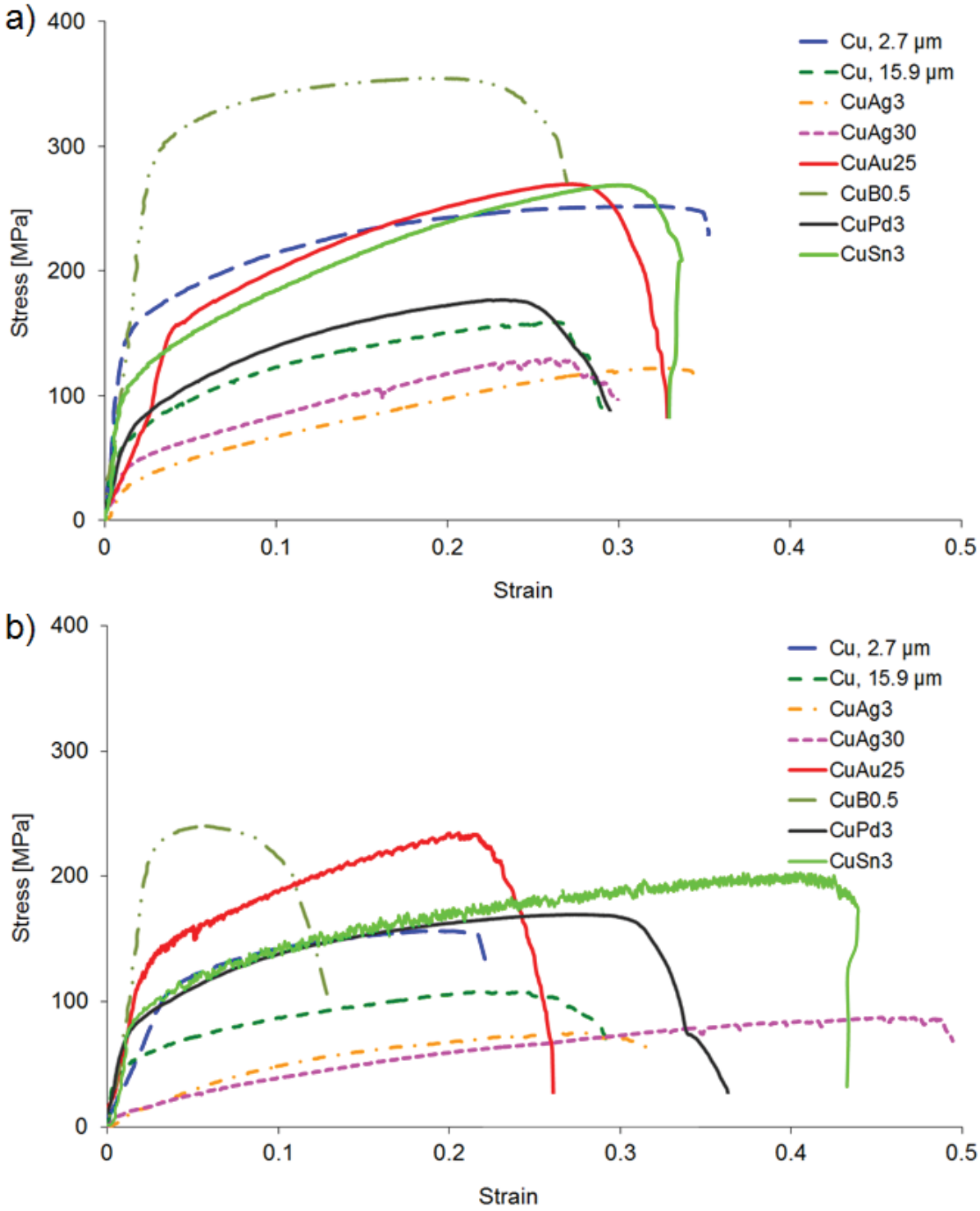

Fig. A6. Stress-strain curves of the virgin Cu samples (Cu, 3 µm), electroplated and annealed samples and implanted samples (CuB0.5). (a) Stress-strain curves at 293 K and (b) stress-strain curves at 473 K.

Tab. A1.Mechanical properties of the primary material, as-deposited and annealed (1073 K, 5h) samples as a function of temperature *T*.

Sample	Condition	*T* [K]	σ_{ys} [MPa]	UTS [MPa]	ε_f
Cu, 2.7 µm	primary	293	142 ± 5	254 ± 6	0.39 ± 0.01
Cu, 15.9 µm	anneal.	293	60 ± 5	155 ± 6	0.37 ± 0.01
CuAg30	as-dep	293	186 ± 6	241 ± 9	0.29 ± 0.01
CuAg30	anneal.	293	54 ± 11	119 ± 28	0.38 ± 0.01
CuAg3	as-dep	293	134 ± 4	189 ± 8	0.24 ± 0.01
CuAg3	anneal.	293	32 ± 2	129 ± 14	0.40 ± 0.01
CuSn30	as-dep	293	143 ± 6	172 ± 4	0.31 ± 0.01
CuSn3	as-dep	293	183 ± 14	240 ± 18	0.22 ± 0.01
CuSn3	anneal.	293	107 ± 4	235 ± 39	0.31 ± 0.01
CuAu25	anneal.	293	147 ± 17	267 ± 9	0.39 ± 0.04
CuPd3	anneal.	293	68 ± 7	185 ± 12	0.37 ± 0.01
CuB0.5	as-dep	293	283 ± 2	355 ± 9	0.31 ± 0.03
Cu, 2.7 µm	primary	473	107 ± 5	153 ± 8	0.20 ± 0.06
Cu, 15.9 µm	anneal.	473	53 ± 2	104 ± 7	0.36 ± 0.04
CuAg30	as-dep	473	125 ± 9	157 ± 11	0.14 ± 0.01
CuAg30	anneal.	473	27 ± 8	82 ± 11	0.41 ± 0.01
CuAg3	as-dep	473	100 ± 8	125 ± 5	0.15 ± 0.01
CuAg3	anneal.	473	55 ± 8	76 ± 13	0.38 ± 0.01
CuSn30	as-dep	473	85 ± 10	107 ± 3	0.16 ± 0.01
CuSn3	as-dep	473	142 ± 10	195 ± 19	0.12 ± 0.01
CuSn3	anneal.	473	73 ± 10	219 ± 19	0.38 ± 0.01
CuAu25	anneal.	473	132 ± 13	239 ± 18	0.32 ± 0.01
CuPd3	anneal.	473	66 ± 1	161 ± 12	0.38 ± 0.05
CuB0.5	as-dep	473	219 ± 2	242 ± 4	0.13 ± 0.03

A.4 Summary and conclusions

Through a combination of alloying and heat treatment both the strength and ductility of the material can be influenced and the material behavior tailored. An extended heat-treatment removes impurities from the grain boundary; the accompanying decrease in strength through grain growth can be compensated through solid solution hardening.

B Effect of sample dimension

B.1 Introduction

The influence of the sample dimension has been studied, as recent works pointed out the importance of the sample dimension to grain size ratio D : d [5 - 7]. These studies have shown a massive drop in strength if D : d decreases below 5 (i.e. 25 grains per cross-section).

B.2 Experimental details

For the production of the samples two different electrolyte systems have been used, one results in a grain size of 2.7 µm, the other one results in a grain size of 13.5 µm for a 20 µm thin film. However, for all electrolyte systems with increasing film thickness the grain size is increasing. For both materials cross-sections of 20 • 20 µm² (D : d = 2.2 for 13.5 µm grain size (Fig. B1a) and D : d = 54 for 2.7 µm grain size) and 80 • 25 µm² (D : d = 11 for 13.5 µm grain (Fig. B1b) size and D : d = 274 for 2.7 µm grain size) were used. The tensile tests were performed with a strain rate of 0.001 s^{-1}.

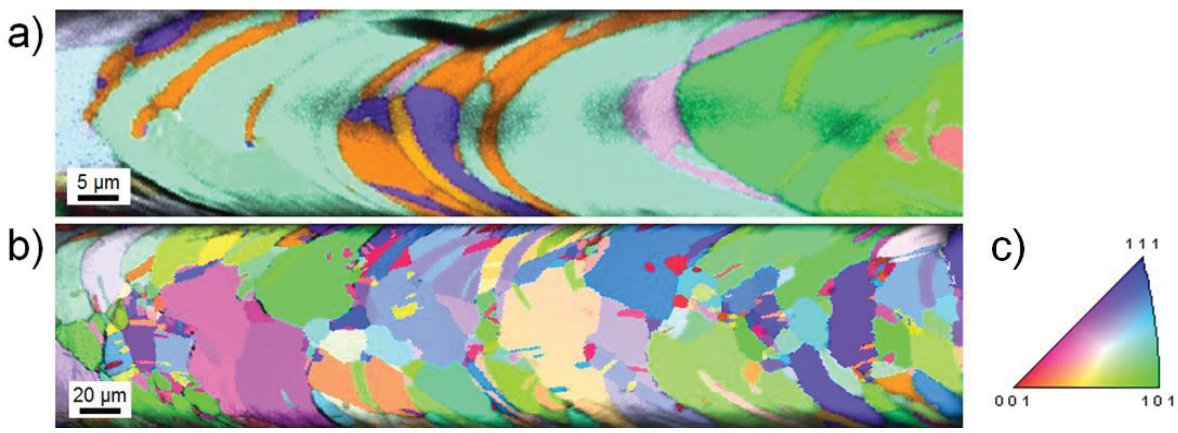

Fig. B1. SEM/EBSD images of samples with 13.5 µm grain size and cross-sections of (a) 20 • 20 µm² and (b) 80 • 25 µm². (c) Color code of the inverse pole figure. Note the difference in scale bars and that grains of the samples can be distorted in the lateral direction because of the surface curvature.

B.3 Results and discussion

The small-grained samples show no significant differences in strength and ductility at all analyzed temperatures. This is caused by the high D : d ratio even for the small samples (Fig. B2). However, the embrittlement which has been discussed for the micro-grained samples with a cross-sectional area of 20 • 20 µm² has also been found for the 80 • 25 µm² samples.

The coarse-grained material with a cross-sectional area of 2,000 µm² and D : d = 11 show a higher UTS compared to the samples with a cross-sectional area of 400 µm² and D : d = 2.2 (Fig. B2). Furthermore the larger samples also showed a larger elongation to fracture, caused by the early localization of deformation and necking in the samples with a low D : d ratio. In the 13.5 µm grained samples with a cross-sectional area of 400 µm² some grains extend across the whole cross-section (bamboo-like microstructure), consequently the deformation is localized in the weakest grain and the strength and elongation to fracture depend on this grain. In the samples with 2,000 µm² cross-sectional area no grain extends across the whole cross-section, resulting in a significant increase in strength and elongation to fracture. The influence is as strong, that the mechanical properties of the large samples (2,000 µm² cross-sectional area) at 673 K exceed the properties of the small samples (400 µm² cross-sectional area) at 473 K.

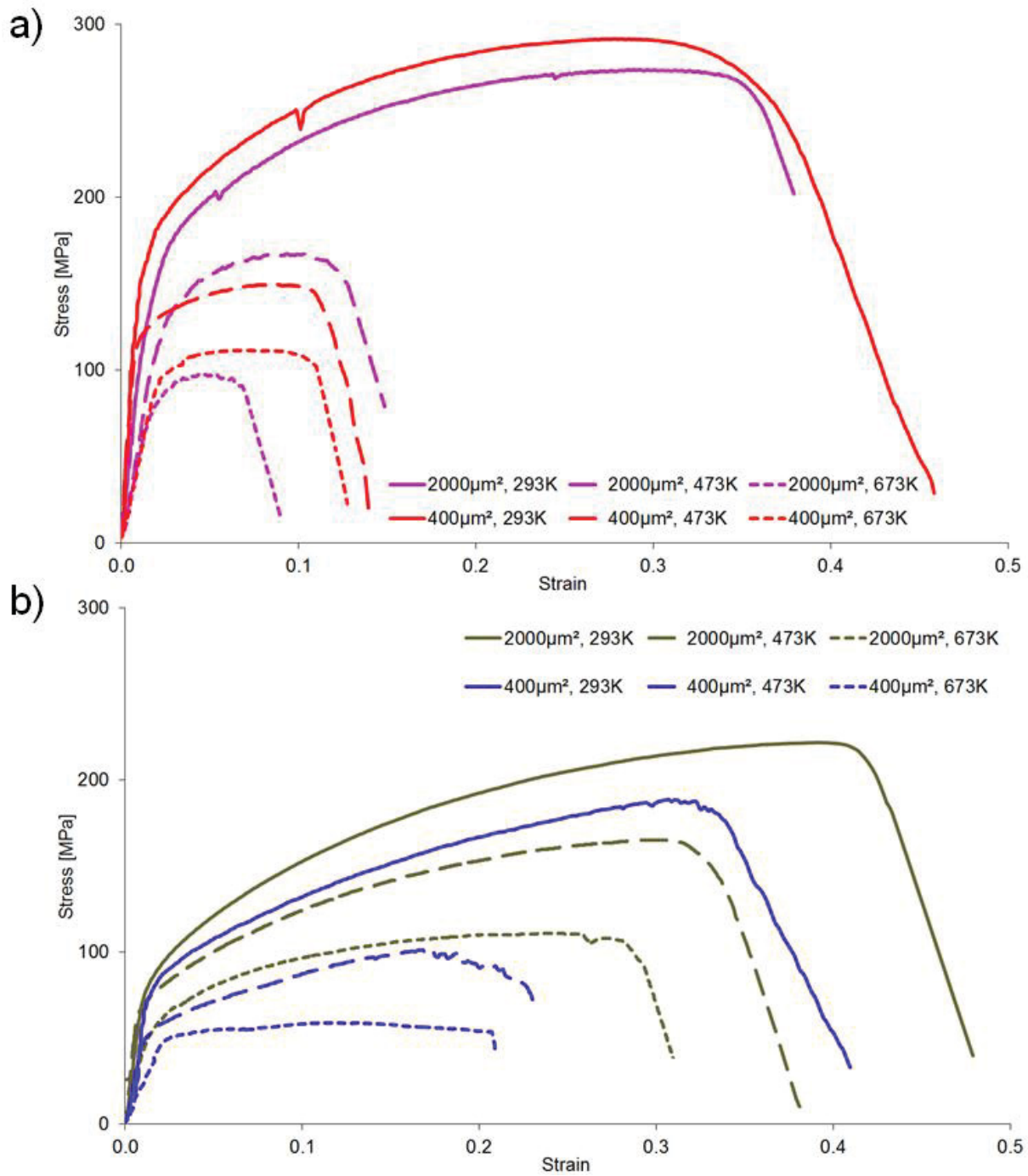

Fig. B2. Stress-strain curves dependent on the sample dimension to grain size ratio $D : d$ and the temperature. Stress-strain curves for the (a) micro-grained material (d = 2.7 µm) and (b) coarse-grained material (d = 13.5 µm).

B.4 Summary and conclusions

It has been demonstrated, that the embrittlement of the 2.7 µm grained material is independent from the sample dimension, furthermore the strength of the small-grained material is independent of the sample dimension. For the coarse-grained material there is a strong influence of the sample dimension caused by the critical D : d ratio.

C Optimization of sample production and handling

A new lithographic wafer mask has been developed to produce several thousand micromechanical samples on one 200 mm Si wafer. The lithographic mask was modified to be able to produce bending and tensile samples together on one wafer (Fig. C1a). To get a freestanding metallic thin film, the Si substrate has to be removed by an etching process as described by Smolka et al. [8]. Prior to this step the metallic thin film has to be covered with polyvinyl butyral (PVB) by spin coating as a protective layer. The laboratory scale spin coating process was modified to be able to coat an entire wafer with one spin coating step (Fig. C1b).Through this up-scaling it was possible to expand the etching process described in [8] to the entire wafer, allowing the production of several thousand samples within a few days.

For the handling of the samples an Invar sample holder system (Fig. C1c), was developed. This allows easy handling of the samples between EBSD scanning, tensile testing and post mortem analysis resulting in an output of 100 %.

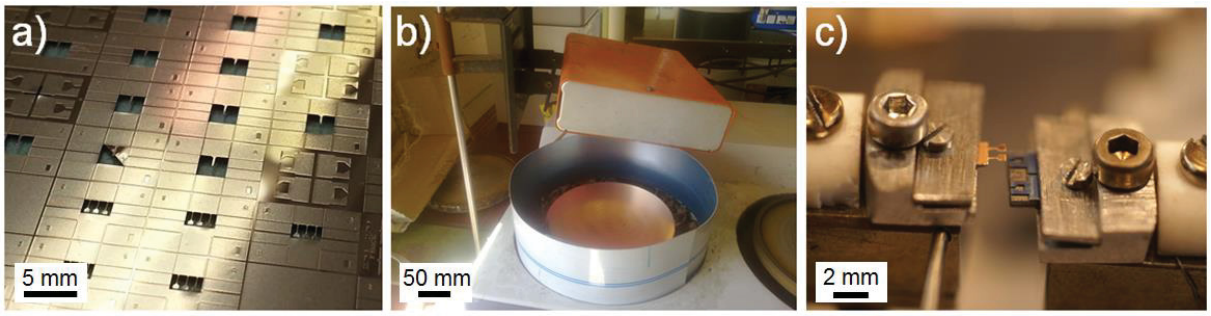

Fig. C1. Optimized production process for preparation of bending samples and tensile samples on one Si wafer. (a) Freestanding thin film samples, (b) optimized laboratory-scale spin-coating process and (c) new sample holder system.

D Novel sample holder for combining *in situ* mechanical testing, SEM, EBSD, APT and TEM on one sample

D.1 Introduction

In the past decades several new techniques have been introduced to material characterization. These methods allow deformation analyses (*in situ* SEM and *in situ* EBSD), microstructural characterization at the nano-scale (TEM) and chemical analysis with atomic resolution (TEM/APT). However, one main drawback is that for different techniques usually different samples have to be used. For example, if a mechanical test and subsequent chemical analysis by TEM/APT is performed, the time consuming lift-out technique has to be used. Furthermore through strong electromechanical forces during APT analysis the welding between APT tip and the support is often the weakest link and causes a fracture (flash) of the sample.

The developed sample holder, which is a further development of the sample holder of Herbig et al. [9] for thin film samples, allows for one to perform a micromechanical test, either with *in situ* SEM or *in situ* EBSD. In the post mortem samples the region of interest can be observed by TEM and/or APT. This allows for the application of several methods of analysis on one sample region, making the comparison between different techniques possible. For example, the analysis of the microstructure, chemical composition and dislocation density can be performed with several different methods on one single sample.

D.2 Sample preparation

Samples are produced by photolithographic process of a 200 mm Si wafer, finally Cu is electrochemically deposited on this Si wafer. The microstructure (e.g. grain size, chemical composition) is controlled by the composition of the electrolyte system [8]. To get a freestanding Cu sample, the Si below the samples is etched as described in Smolka et al. [8]. To obtain the macro sample, which contains between one and six micro bending or tensile samples (the number of samples depends on their size), the wafer is pre-notched by a diamond tip and cut by a scalpel. The Si pad below the samples is grinded to a thickness of 10-20 µm after the samples were attached to the

TEM grid having a 120° opening (Fig. D1a). The thinning of the Si was needed to ensure that the TEM grid would fit to the sample holder in the TEM. This also ensures that the Si layer does not influence the primary electron beam in the TEM. Fig. D1b illustrates a bending beam during *in situ* fatigue testing inside the SEM.

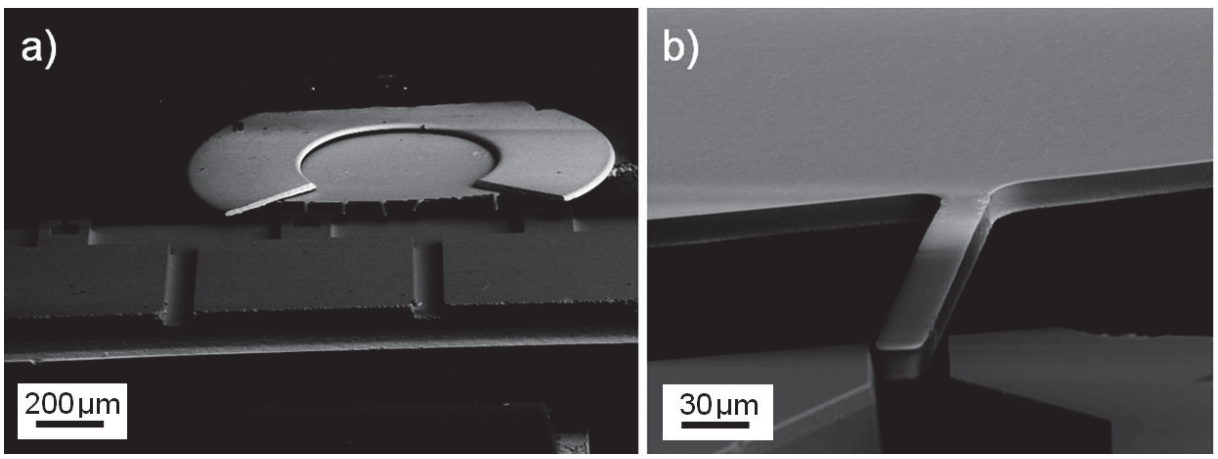

Fig. D1.(a) Macro-sample with 6 micro-samples mounted on a TEM grid with an opening angle of 120°. Note, that micro-samples 1-5 (right) are readily deformed in a cyclic bending experiment (sample 2 fractured) and micro-sample 6 (outermost left) is in position to perform the cyclic bending experiment. As a counterpart for the bending experiment a silicon gripper as described in [5] was used, (b) Micro-sample during cyclic-bending experiment. Note, that the sample shows significant damage with intrusions/extrusions close to the sample foot.

D.3 Post mortem analysis

After mechanical testing (either by tensile testing of dog bone shaped samples by static or cyclic tensile testing or static or cyclic bending of a needle shaped sample) the region of interest (e.g. a fractured grain boundary) is prepared by FIB, either by preparing a thin lamella for TEM (Fig. D2) or a needle shaped sample for APT or TEM (Fig. D2). Note, that for the APT analysis the tip needs a minimum length of > 50 µm. However, for most fractured tensile and bending samples APT of the deformation zone is possible, as long as it is close to the sample center. Results of *in situ* like EBSD, APT and STEM observations are shown in Fig. D3, demonstrating the functional efficiency of the sample holder system.

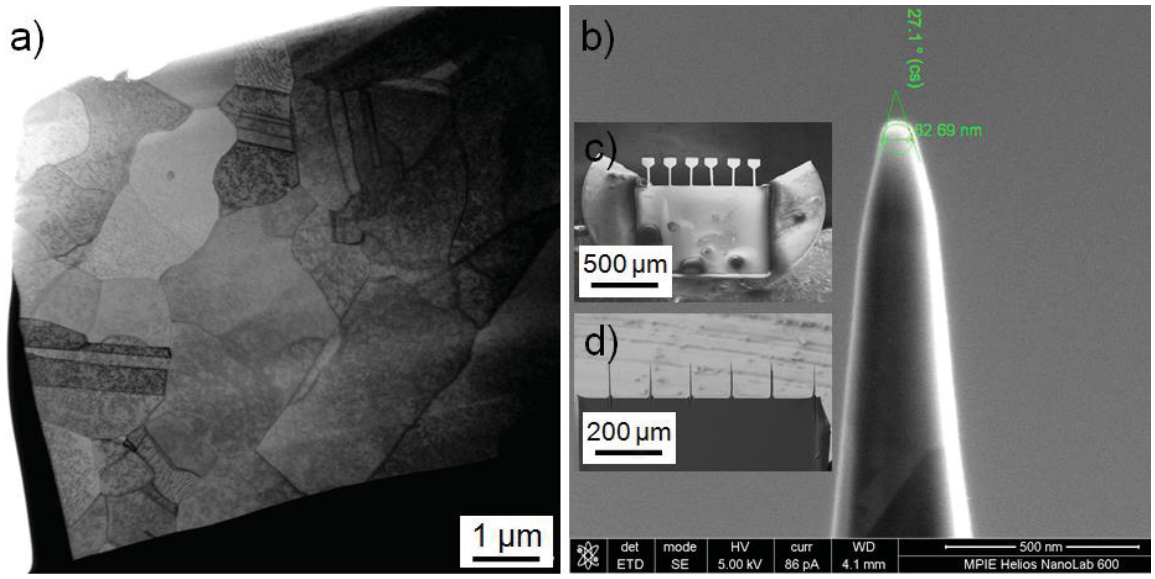

Fig. D2.(a) TEM image of the of the deformation zone of a fractured sample (see Fig. D1, second sample from right), (b) Atom probe tip prepared from a dog-bone shaped sample, (c) samples before and (d) after FIB milling.

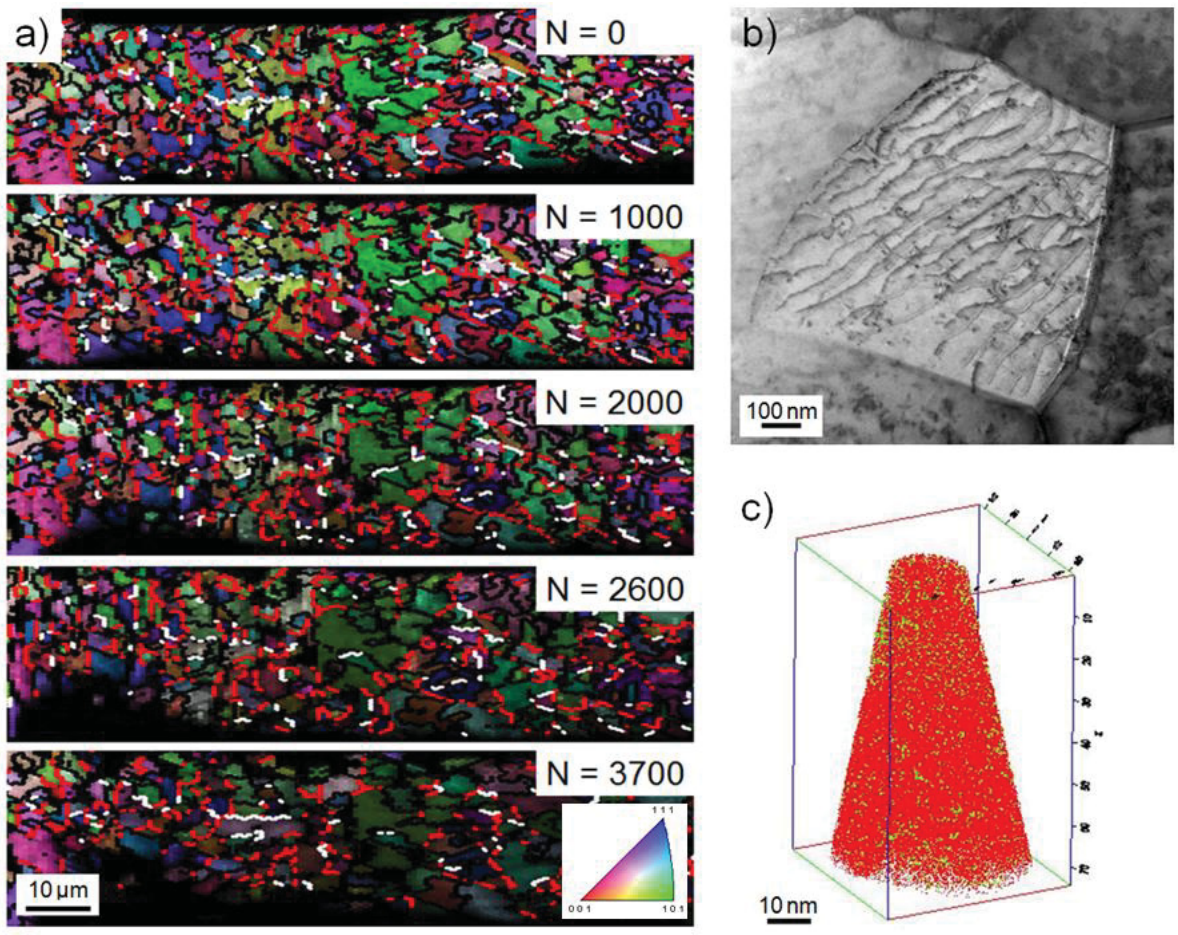

Fig. D3.Results of analysis of electrodeposited Cu thin films with the new sample holder technique. (a) *in situ* EBSD analysis of a cyclic bending experiment, (b) STEM image of a grain in the deformation zone of a cyclic bending experiment [10] and (c) atom probe tomography of a Cu sample.

D.4 Summary and conclusions

This sample holder system is a further development of the system developed by Herbig et al. [9]. Both systems allow FIB preparation, TEM and APT analysis on the same sample using only one sample holder system, ensuring constant geometrical conditions (without tilting during sample transfer). However, the holder system presented in this publication allows micromechanical testing (*in situ* SEM / *in situ* EBSD) without any sample transfer afterwards and without the need for lift-out technique. Consequently, it is possible to determine the dislocation density by analysis of high resolution Kikuchi pattern, Kernel average misorientation (KAM), electron channeling contrast imaging (ECCI) [11] and TEM. Furthermore comparison of chemical analysis methods (e.g. Auger electron spectroscopy (AES), TEM and APT) is possible.

E Empiric formula for the estimation of the flow stress

Based on the work of Taylor [12], Kocks [13], Hansen [14], Meyers [15] and Yang [5] an empiric formula was developed to estimate the flow stress σ_{pred} of a single grain:

$$\sigma_{\text{pred}} = M \bullet [(\tau_{\text{i}} + 0.5\tau_d) \bullet \xi_{geo} + 0.5\tau_p], \tag{E1}$$

where M is the local Taylor factor [12], τ_i [MPa] is the intrinsic shear stress [13], τ_d [MPa] the grain size dependent shear stress [14], τ_ρ [MPa] the work hardening (dislocation density) dependent shear stress [14] and ξ_{geo} a geometric factor [5]. Note that this model assumes that hardening mechanisms do not affect each other.

Parameters as Taylor factor, grain size and the GND density as an approximation for the dislocation density can be simply obtained from an EBSD image. Consequently for an *in situ* EBSD experiment the weakest grain/cross-section can be estimated from the initial EBSD image making it possible to reduce the scanning area to the area which is most prominent to plastic deformation. Furthermore in real life Cu lines the possible fracture sides can be estimated.

References

1 CT Liu, CL White, JA Horton, Acta metall. 33, 2, (1982), 213-229.

2 JH Liao, HY Bor, CG Chao, TF Liu, Mat. Trans. 52, 10, (2011), 1989-1997.

3 AB Martin, RD Johnson, F Asaro, J. Appl. Phys. 25, 364, (1954), 364-369.

4 NL Peterson, Phys. Rev. 132, 6, (1963), 2471-2476.

5 B Yang, C Motz, M Rester, G Dehm, Phil. Mag. 92, 25-27, (2012), 3243-3256.

6 XW Gu, CN Loynachan, Z Wu, YW Zhang, DJ Srolovitz, JR Greer, Nano Lett. 12, (2012), 6385-6392.

7 DC Jang, JR Greer, Scr. Mater. 64, (2011), 77.

8 M Smolka, C Motz, T Detzel, W Robl, T Griesser, A Wimmer, G Dehm, Rev. Sci. Instrum. 83, 6, (2012), 064702.

9 M Herbig, D Raabe, YJ Li, P Choi, S Zaefferer, S Goto, Phys. Rev. Lett. 112, (2014), 126103, 1-5.

10 P Imrich, unpublished.

11 I Gutierrez-Urrutia, S Zaefferer, D Raabe, Mat. Sci. Eng. A 527, (2010), 3552-3560.

12 GI Taylor, Proc. Roy. Soc. A145, (1934), 362-387.

13 UF Kocks, H Mecking, Progr. in Mat. Sci. 48, (2003), 171-273.

14 N Hansen, Mat. Sci. Eng. A 409, (2005), 39-45.

15 MA Meyers, A Mishra, DJ Benson, Prog. in Mat. Sci. 51, (2006), 427-556.